AN ELECTRONIC

SPIRIT LEVEL TILT SENSOR

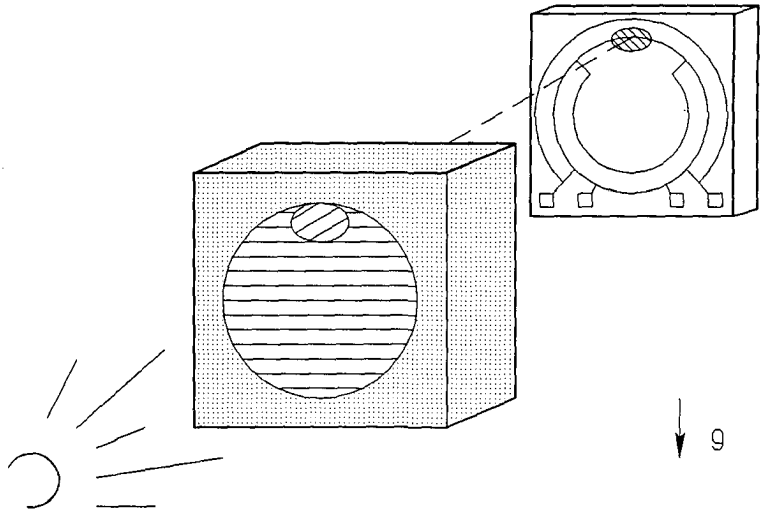

Yizi Xing

AN ELECTRONIC

SPIRIT LEVEL TILT SENSOR

AN ELECTRONIC SPIRIT LEVEL TILT SENSOR

PROEFSCHRIFT

ter verkrijging van de graad van doctor
aan de Technische Universiteit Delft,
op gezag van de Rector Magnificus,
Prof.drs. P.A. Schenck
in het openbaar te verdedigen
ten overstaan van een commissie door
het College van Dekanen daartoe aangewezen
op dinsdag 28 februari 1989 te 14.00 uur

door

Yizi Xing

Elektrotechnisch ingenieur
geboren te Peking, China

Dit proefschrift is goedgekeurd door de promotor
Prof.dr.ir. S. Middelhoek

aan Yaya
aan onze ouders
aan de familie Vastenhouw

CONTENTS

CHAPTER 1 INTRODUCTION

In this thesis an account is given of research work carried out on a tilt sensor. A tilt sensor is an electronic device which provides information on the attitude of an object relative to the orientation of the gravitational field of the earth. It is the gravitational field which defines the vertical and horizontal at any given place on this planet. When an object is tilted from its rest position, an angle can be defined between a reference line and the vertical or horizontal. That angle is called the tilt angle. It is crucial information for use during construction of buildings, roads and bridges, and in control systems for vehicles.

From the time man first began to build houses, he must have had ways of determining the tilt angle. Perhaps, at first, his observation of tilt was based on perception, and only much later did he advance enough to create tools. One of the tools is still in current use and familiar to all, the spirit level. The basic element of the spirit level is a glass vial which is partially filled with some kind of liquid. Due to the gravitational force, the air bubble captured in the glass–liquid system always has the tendency to stay at the top when the vial rotates. Electronic versions of this device have been developed over the past thirty years and are now commercially available. Common features of these devices are the high sensitivity, usually capable of sensing tilt angles of arc seconds or even less, and the small measurement range, the

largest being only several degrees. The electronic tilt sensor described in this thesis is based on the principle of the spirit level, but is aimed at a measurement range of 360 degrees and a linearity within one degree. This device, which provides an electrical output signal for an input tilt angle, can be small in size and suitable for mass production. Compared with tilt sensors which use a pendulum, the spirit level principle has the virtue of being free from the mechanical friction associated with the pendulum. The functional aspects of the vial and the working liquid, the sensing device of the position of the air bubble, and the electronic signal–processing circuit are the main subjects of this thesis.

1.1 SIGNAL CONVERSION AND TILT SENSING

Without exception an electronic information–processing system consists of three units: an input transducer, a signal processor and an output transducer [1.1]. In an input transducer, often called a sensor, a nonelectrical measurand such as pressure, displacement or light intensity is converted into an electrical signal. In the signal processor the electrical signal is amplified, filtered or converted from analog into digital. In the output transducer the electrical signal is converted into a signal which can be perceived by human senses (display) or which can cause action (actuator). This signal conversion from one type into another takes place in the input and output transducers. The signals can be divided into six signal domains: radiant, mechanical, thermal, electrical, magnetic, and chemical, as shown in Fig.1.1.

In Fig.1.1, the signal domains are drawn in such a way that the emphasis is on the mechanical and electrical domains, because it is between these domains that signal conversion takes place in a tilt sensor. As shown in Fig.1.2, in a tilt sensor of any type three basic units can be distinguished: a gravitation–orientation sensing unit, a position–sensing unit and an associated electronic signal–processing unit. A gravitation–orientation sensing unit usually contains a mass element. The position of the mass element, defined in a coordinate system based on the frame of the unit, is determined by the tilt angle. This processing of signal within the mechanical domain is represented by an extra branch associated with this domain, as depicted in Fig.1.1. In order to obtain an electrical signal, a position–sensing unit is required to convert the position of the mass element, which is a mechanical signal, into an electrical signal. The last block in the chain is an electronic signal–processing unit, which can be the entire signal–processing system or just a part of it.

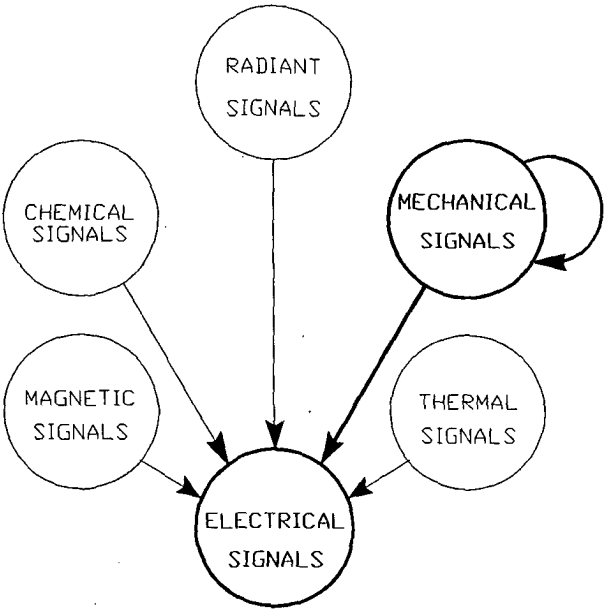

Fig.1.1 *Diagram representing the five possible signal conversions in sensors. The extra branch associated with the mechanical signal domain shows that for a tilt sensor mechanical signal processing takes place within that domain.*

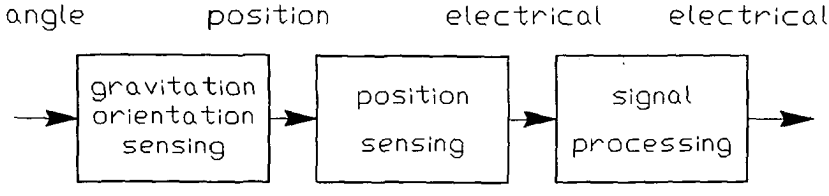

Fig.1.2 *Functional block diagram of a tilt sensor.*

1.2 GENERAL ASPECTS OF TILT SENSORS

1.2.1 Sensitivity of the gravitation–orientation sensing unit

Tilt measurement is in fact angle measurement. The sensitivity of the sensor is dependent on the sensitivity of the gravitation–orientation sensing unit, the position–sensing unit and the signal–processing unit. In the gravitation–orientation sensing unit the tilt angle is the input signal and the position of the mass element is the output signal. If θ represents a small change in the tilt angle and d the corresponding change in position, the sensitivity of the gravitation–orientation sensing unit S_g can be defined as:

$$S_g = \frac{d}{\theta}$$

For the gravitation–orientation sensing unit various working principles have been employed over the past years. These principles can roughly be divided into the following types:

- the vertical pendulum type,
- the horizontal pendulum type,
- the spirit level type,
- the liquid level type.

In Fig.1.3(a) a gravitation–orientation sensing unit based on a vertical pendulum is depicted. It is constructed by suspending a solid mass on a pivot from a cord or a rod of a negligible weight. The mass can swing freely in one or two directions, depending on the kind of pivot bearing the cord. The horizontal pendulum is shown in Fig.1.3(b): a solid mass is fixed to a rigid rod which is suspended horizontally by two fine cords from a bracket. The joint points of the two cords with the rod are situated in different places. A line passing through the ends of the cords fixed to the bracket forms a virtual axis, around which the pendulum can rotate. In a spirit level type the position of the air bubble is used as the reference. The moving track of the air bubble is predefined by the curvature of a solid wall which contains the liquid and the air bubble. The situation is presented in Fig.1.3(c). In contrast with the spirit level type,

the liquid level type uses a container which is open at the top. The displacements of the liquid level along the two side walls are observed as measures of tilt, as shown in Fig.1.3(d). The input–output relation of these four types of gravitation–orientation sensing unit are given below:

$d = l\,\theta$ vertical pendulum

$d = l\ arctan\ \frac{tan\theta}{sin\phi} \approx \frac{l}{\phi}\,\theta$ horizontal pendulum

$d = r\,\theta$ spirit level

$d = \frac{b}{2}\,tan\theta\ \approx \frac{b}{2}\,\theta$ liquid level

In these equations l represents the distance between the rotating point and the mass center, ϕ the angle between the vertical and the virtual axis, r the distance between the geometric center of the air bubble to the center of the curvature of the vial, b the length of the base line of the liquid container. The angles are all expressed in radians. Several points must be noted concerning the above equations:

(a) The vertical pendulum type and the spirit level type have an inherent linear relationship between the input tilt angle and the output position, while linear approximations can only be used for the horizontal pendulum and the liquid level when the tilt angle is small.

(b) The vertical pendulum and the spirit level are reversible devices, which means that, if we turn the device upside down and interchange the density of the mass element with its surrounding matter, a new gravitation–orientation sensing unit is obtained with the same principle. Examples are an air balloon fixed to a cord or a steel bullet trapped in a spherical container. The former is fictive, but the latter has been realized in practice.

(c) The sensitivities of the gravitation–orientation sensing units are only dependent on geometric factors. Increasing the sensitivity usually means increasing the size of the sensor. Physical properties of the materials, such as weight, density, viscosity and surface tension, have no direct influence on the sensitivity of the gravitation–orientation sensing unit.

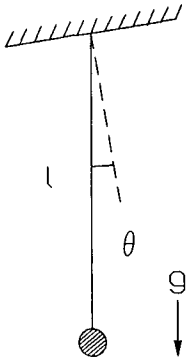

(*a*) $S_g = l$

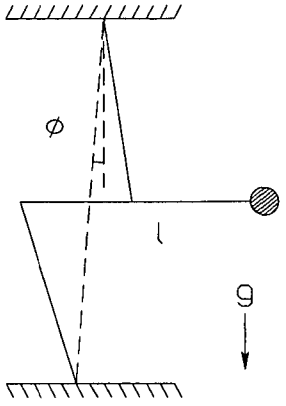

(*b*) $S_g = \frac{l}{\phi}$

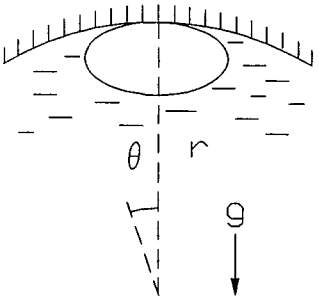

(*c*) $S_g = r$

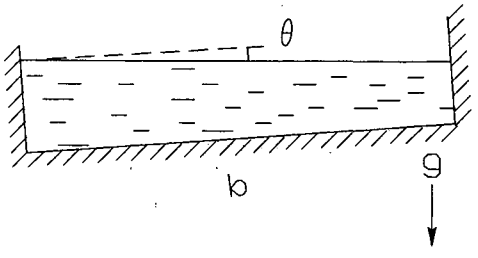

(*d*) $S_g = \frac{b}{2}$

Fig. 1.3 *Diagrams showing the four principles most often employed in a gravitation–orientation sensing unit: (a) the vertical pendulum type, (b) the horizontal pendulum type, (c) the spirit level type, and (d) the liquid level type.*

1.2.2 Tilt and acceleration

The mass element in the gravitation–orientation sensing unit changes its position under the influence of the gravitational field when the device is tilted. But the same result is also obtained when the device is accelerated in the horizontal direction. It is generally accepted that the acceleration effect is inseparable from the tilt effect in tilt sensors. This is the reason why an accelerometer with some modifications can be used for tilt sensing, and vise versa. For example, when a pendulum mass is suspended from a frame and the frame is tilted, an angle is formed between the direction of the gravitational field and the internal reference line. But the same angle can also be obtained when the frame is horizontally accelerated. The angle can be expressed as: $\theta = arctan(a/g)$, where a is the inertial acceleration in the horizontal direction and g is the gravitational acceleration. In a more general sense, it can be said that the gravitational field created by a mass and the inertial field created by the acceleration of the reference frame are indistinguishable. The theoretical background can be found in the statement known as the *principle of equivalence*, which requires that physical laws must be written in a form independent of the state of motion of the frame of reference [1.2]. It shows an equivalence between a gravitational field and an accelerated frame of reference.

However, the possibility of constructing sensors (not only tilt sensors) capable of delivering separate output signals of acceleration, rotation and gravitation without interference from each other is not yet extinct, at least theoretically. In a feasibility study, Forward [1.3] has pointed out that an inertial field created by an acceleration and a gravitational field created by a mass do not have the same nature. The inertial field is a uniform vector field in space and has no gradients, whereas the gravitational field is highly nonuniform and has an unlimited number of higher order gradients. Based on this elementary phenomenon, concepts have been proposed for gravity sensors which are able to measure separately the effects of acceleration, rotation and gravitation. One of the proposed devices consists of two pairs of accelerometers placed orthogonally at some distance from each other. By properly adding and subtracting their outputs, information about the acceleration, rotation and gravitation is obtained independently.

With few modifications the same principles can be applied to the measurement of tilt. In order to illustrate the idea, we simplify the problem by only taking the translational movement of the sensor into our consideration so that the number of accelerometer pairs can be reduced to one. As shown in Fig.1.4, the two

accelerometers are placed at the ends of a rod with their sensitive axes in parallel with the rod. The rod is tilted a small angle θ from the horizontal. In the meantime the whole system is also accelerated by a force $\underline{F}$. The readings at the devices' outputs expressed in the unit of acceleration are:

$$a_1 = -\frac{F_x sin\theta - F_y cos\theta}{m} - \frac{\gamma M cos^2\alpha}{(R + l cos\theta/2)^2} sin(\alpha + \theta)$$

$$a_2 = \frac{F_x sin\theta - F_y cos\theta}{m} - \frac{\gamma M cos^2\alpha}{(R - l cos\theta/2)^2} sin(\alpha - \theta)$$

where γ is the proportionality constant, M the mass of the earth, m the mass of the mass element in the accelerometer, l the distance between the two accelerometers. Adding a_1 and a_2 we obtain:

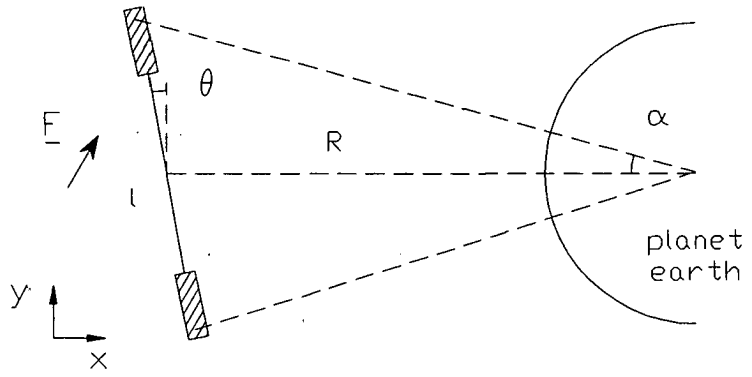

Fig.1.4 A tilt sensor consisting of two accelerometers. The influence of the acceleration is eliminated when the outputs from the accelerometers are added.

$$a_{\text{tilt}} \approx -\frac{gl}{R}cos\theta$$

where g is the gravitational acceleration. In the above equation the acceleration dependent fraction vanishes so that the output of this sensor is now only dependent on the tilt angle.

The reason why there are no actual realizations of this concept is a practical one: in the sensor output the components with higher order gradients related to the gravitational field are too weak compared with the components of lower gradients and the inertial field. As we can see from the above equation, the sensitivity of this sensor depends on the length of the rod, the radius of the earth and the gravitational acceleration. As l is determined by the size of the device, which is usually several tens of millimeters, and R is approximately the same as the radius of the earth which is 6.37×10^6 m, the sensor sensitivity calculated with the above equation is thus extremely low.

Theoretically, the devices described above do not violate the principle of equivalence. In fact, the principle requires a uniform gravitational field, which in practice would only be realistic if the observer's laboratory occupies a space with infinitely small dimensions. Such a condition is valid for the commonly used accelerometers and tilt sensors, because, as the principle of operation, the mass elements in the gravitation–orientation sensing units are always treated as point masses. Whereas in sensors described by Forward the nonuniformity of the gravitational field is intentionally utilized.

In practice, since horizontal acceleration and tilt can not be distinguished in the output, tilt sensors are usually not used in dynamic environments. They are sensitive for mechanical shocks and vibrations. Therefore, although not necessary for the operational principle, damping effects are incorporated in nearly every practical device. A poorly damped tilt sensor can oscillate for a long period of time after the environmental disturbance has disappeared. It sometimes also causes electrical drift in the signal–processing system.

1.2.3 Application and terminology

Tilt sensors have very broad applications in fields such as civil engineering, geophysical observation, alignment of machinery and attitude–control instruments. In the control systems of road–paving and road–scraping machines information is required on the inclination of the ground with the horizontal. In order to determine the angular position of the boom of a crane or the carriage of a tip lorry, tilt sensors can be employed. As a tilt sensor uses the gravitational field as the reference, an indication of the tilt angle of the object under measurement (the boom and the carriage) can be obtained regardless of the attitude of the vehicles (the crane and the tip lorry). This is the main difference between the tilt sensor and other angle measuring devices, such as an optical shaft encoder. During construction of buildings, piles and bridges where alignment of structures with a reference line is needed, sensitive tilt sensors can have an important function. A tilt sensor, in combination with a distance or depth measuring device, can provide information on the slope of a hill or of a bore hole in the ground. For ships, airplanes, submarines and torpedoes or missiles, the pitch and roll of the vehicles are crucial information for the attitude–control systems. Tilt sensors with their relatively simple structures and low cost can sometimes replace more complex and expensive gyroscopic instruments. The main disadvantage relative to gyros is, of course, the sensitivity to interfering translational acceleration inputs. However, on the other hand, a gyro normally needs to be overhauled after a thousand–hour operation time, whereas a simple tilt sensor can go on for years without any maintenance. In the field of geophysical instrumentation, tilt sensors have been very useful to monitor ground activities such as earth tides, volcanoes, earthquakes, earth flows and slope deformations. In such circumstances, the demands on the sensor sensitivity and stability are extremely high.

The broad application of the tilt sensor is also reflected in the names used for it. The names which frequently appear in the literature are: liquid level, bubble level, spirit level, electrolevel, leveling switch, electrolytic potentiometer, inclinometer, slope indicator, tiltmeter, tilt sensor, pendulum, horizontal pendulum. Apparently, devices with names associated with "level" use liquids in the gravitation–orientation sensing unit; pendulum is usually meant to be the vertical type pendulum. The term inclinometer is often used in civil engineering, where tilt angles with respect to the horizontal rather than the vertical are measured. Tiltmeter and tilt sensor may represent devices of any kind.

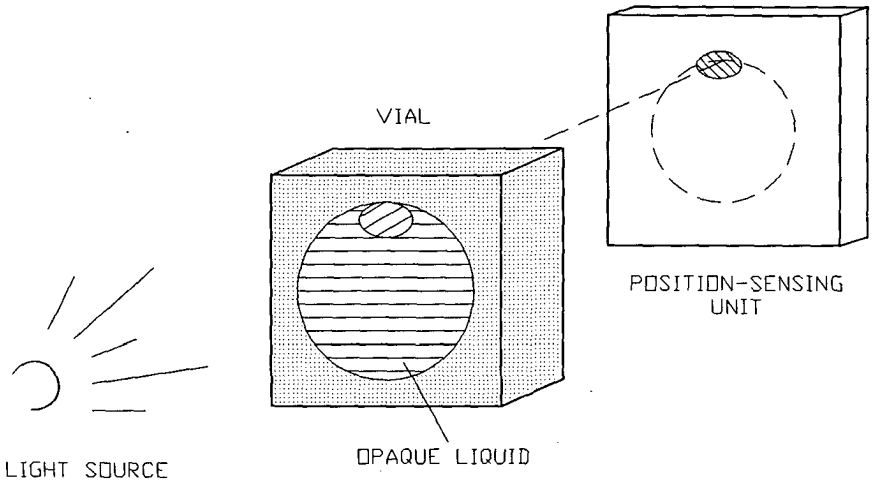

Fig.1.5 *Schematic illustration of the electronic spirit level tilt sensor.*

1.3 PRINCIPLE OF THE SENSOR

The operational principle of the electronic spirit level tilt sensor is schematically illustrated in Fig.1.5. It consists mainly of a vial, a light source and a position–sensing unit. The associated electronic signal–processing unit is omitted in the figure. The vial has a cylindrical hole in the center, which is partially filled with an opaque liquid. The vial is settled in a vertical position and operates within the plane perpendicular to the axis of the hole. It can be seen that, due to the gravitational force, the air bubble inside the vial always tends to remain at the top of the spherical cavity when the device is rotated. The angle between the geometric center of the air bubble and an internal reference line of the vial provides an indication of the angular position of the tilt sensor with respect to the gravitational field.

In order to detect the angular position of the air bubble, an optical method is employed. The vial is placed between a light source and a light spot position–sensing unit. Since the working liquid inside the vial is nontransparent, only the part of the light which passes through the air bubble can be received by the position–sensing unit. The position–sensing unit then provides an electrical signal which indicates the position of the light spot, and so the tilt position of the tilt sensor.

1.4 ORGANIZATION OF THE THESIS

In Chapter 2 an overview of the literature on tilt sensors is presented and different ways of fabricating the sensor are discussed. It will be shown that three aspects characterize the construction of a tilt sensor: the gravitation–orientation sensing unit, the method used for position sensing, and the way of achieving a proper damping effect. In Chapter 3 the gravitation–orientation sensing unit which is used in our tilt sensor is discussed. The choice of the working liquid and the liquid dye, the property of the light source, and the dynamic response of the tilt sensor are the main topics of this chapter. The position–sensing unit will be dealt with in Chapter 4. Position–sensitive detectors (PSD's) utilizing the lateral photoeffect are considered suitable for use in the tilt sensor. Performances of the two–dimensional bilateral photodiode–type PSD and the angular position–sensitive detectors (APD) are presented and analyzed. In Chapter 5 an electronic signal–processing circuit is presented, which can be integrated with an APD on one chip with a bipolar IC process. Experiments on this circuit are described. In the final stage, a prototype electronic spirit level tilt sensor with a large measurement range is constructed. Experimental results of this device are presented in Chapter 6. The experimental setups, which are used in the measurements presented in Chapter 3, Chapter 4 and Chapter 5, are also described in Chapter 6.

References

[1.1] S. Middelhoek, "Integrated sensors", Proc. 3rd Jap. Sensor Sym., Tsukuba Science City, pp.1–10, 1983.

[1.2] M. Alonso and E. J. Finn, "Fundamental university physics", Vol.1, "Mechanics and thermodynamics", 2nd edition, Addison–Wesley Publishing Company, Amsterdam, 1980.

[1.3] R. L. Forward, "Gravity sensors and the principle of equivalence", IEEE Trans. on Aerospace and Electron. Systems, Vol.AES–17, pp.511–519, 1981.

CHAPTER 2 OVERVIEW

2.1 INTRODUCTION

In this chapter an overview is given of the state of the art of tilt sensors. In the overview, tilt sensors are classified in categories according to the type of the gravitation–orientation sensing unit used in the sensor. These are the pendulum based units, *i.e.* the vertical and the horizontal pendulums, and the liquid based units, *i.e.* the spirit and the liquid levels. Besides the gravitation–orientation sensing unit, a position–sensing unit must be employed in a tilt sensor in order to determine the pendulum position or the liquid level. The commonly employed methods for position sensing are the capacitive, resistive, optical and inductive methods. The use of the position–sensing method is closely related to the gravitation–orientation sensing unit and the specific requirements on the performance of the sensor. Another aspect which must be taken into consideration is the dynamic behavior. In most of the tilt sensors damping effects are obtained by using viscous liquids and mechanical springs, or by electromagnetic means. From the view of sensor construction, the choice of the gravitation–orientation sensing unit, the use of the method for position sensing, and the way of achieving a proper dynamic response are distinguishing features. Since measurements of tilt angle can also be carried out by employing devices like

accelerometers and gyros, brief descriptions of their principles of operation will be given as well.

2.2 PENDULUM BASED TILT SENSORS

2.2.1 Vertical pendulum

The earliest electronic version of a simple plumb bob delivering an electrical output signal was reported to be the Talyvel [2.1] which was developed in 1964. When a metallic pendulum was placed between two ac–excited electrodes, a small change of the pendulum position caused a change in the capacitance of the system, which could be detected by synchronous detection or by other electronic means. The structure is illustrated in Fig.2.1. The same principle has also been adopted by many other designers [2.2, 2.3] in their tilt sensors. In the field of geophysical instrumentation, Graf in 1964 and Schneider in 1966 [2.4] independently developed a vertical pendulum to measure deviations from the vertical in two perpendicular directions. The vertical pendulum tilt sensor was a biaxial device with a length of two meters. The deflection of the pendulum from the vertical was measured by means of two perpendicular capacitive bridge readout systems. Bonatz [2.5] examined the technical properties of the device and found that air temperature changes could considerably affect the measurement results. The vertical pendulum was preliminarily damped by immersing the system in a fluid with a high viscosity. A more sophisticated vertical pendulum tilt sensor with the ability of offset compensation was designed by Zschau [2.6]. His device consisted of cylinder coils which generated a magnetic field exerting a torque on the pendulum. Compensation of drift was achieved by sending a direct current through the coils. The damping effect could be modulated by varying the capacitance value of a capacitor in the feedback circuit. The vertical pendulum tilt sensor was an extremely wide band device with its output signal superimposed by various noises. This led to the development of an active Butterworth–Bessel low–pass filter by Flach and Grobe–Brauckmann [2.7]. The active filter showed a flat amplitude response below the natural frequency and a high attenuation beyond. The vertical pendulum tilt sensor with a capacitive sensing method usually has a high sensitivity; it is able to resolve a tilt of less than one arcsec. It has a small measurement range; the largest is only several degrees. A general overview of the vertical pendulum tilt sensor was presented by Flach [2.8] in 1976.

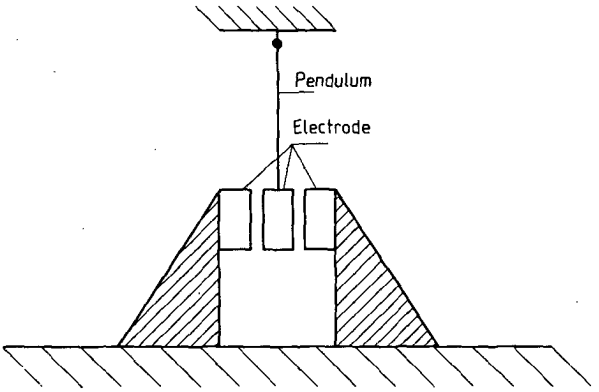

Fig.2.1 A vertical pendulum tilt sensor with a capacitive sensing method [2.1].

In civil engineering and in control systems of vehicles, the measurement of large tilt angles is required. Pendulum based devices are usually employed for these applications. In these devices the electrical pick–up of the pendulum position is usually resistive. Ordinary potentiometer–like resistive elements are used with the pendulum functioning as the wiper. A fluid with a certain specific mass density and viscosity is incorporated in the sensor in order to compensate for the pendulum weight, and to provide the possibility of changing the damping constant. In some cases mechanical springs are also employed. The dynamic response of the device depends on the mass and moment of inertia of the pendulum, the viscosity of the fluid and the elastic constant of the spring [2.9]. The commercially developed Penny & Giles type has a full–scale measurement range of 300 degrees and a nonlinearity of ± 0.5 % [2.10]. Figure 2.2 shows a diagram of the pendulum tilt sensor.

The shortcomings of the pendulum type tilt sensor with the resistive sensing method are the mechanical friction at the tip of the wiper with the resistive element and the friction at the pivot point. As the first part of the problem, the contact between the wiper and the resistive element introduces sliding noise, limits the position resolution, causes a rotational torque and reduces sensor lifetime. In order to solve this problem, a tilt sensor developed by Slope Indicator Company in the U.S.A was provided with a switch which controlled the tip of the wiper so that it only touched the resistive element when the switch button was pushed [2.11]. In recent years, as a result of rapid development in contactless potentiometers, tilt sensors have been built using this principle [2.12, 2.13]. In the sensor a permanent magnet was mounted on the pendulum and the conventional resistive element was replaced by a

magneto–resistive element, whose resistance changed with the strength of a magnetic field. A drawback of utilizing the magneto–resistive element is its large temperature coefficient. As the second part of the problem, the mechanical suspension of the pendulum mass causes a frictional drag force and is sometimes also a source of drift. In order to avoid this problem, Simon *et al.* [2.14] designed a pendulum made of a diamagnetic mass. The pendulum was suspended in a magnetic field derived from a permanent magnet. The tilt position of the pendulum was sensed by using an optical method. The device had a diameter of 10.2 cm and a length of 15.2 cm. The output characteristic was linear within 10 arcsec and the device had a sensitivity of 9 μA/arcsec. In 1979 Schaevitz Engineering [2.15] developed a tilt sensor which consisted of a paddle, a position detector and a torque motor with a control network. When the sensor was tilted, the paddle was kept in a fixed position by the motor. The current through the motor was directly proportional to the sine of the tilt angle. The sensor has been used for radar and missile vehicle leveling and for the determination of the pitch and roll of a naval gun turret for the fire–control computer. In some other conventional type tilt sensors, strain gauges and vibrating wires have been used as the sensing devices for the pendulum position [2.16].

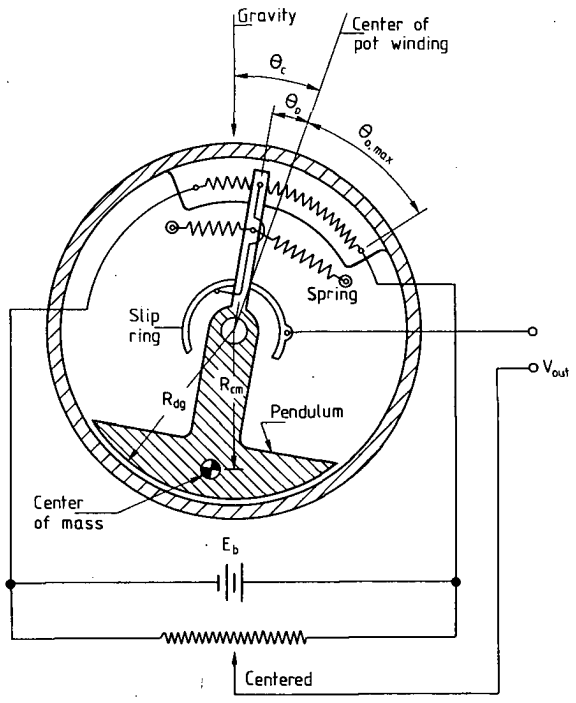

Fig.2.2 A pendulum tilt sensor capable of measuring large tilt angles [2.10].

2.2.2 Horizontal pendulum

The invention of the horizontal pendulum can be traced back to the beginning of the nineteenth century when Hengler discovered a method which greatly increased the sensitivity of the pendulum by using a bifilar suspension [2.17]. He carried out numerous observations using his instrument to demonstrate the effect of luni–solar attraction. The movement of the tip of the pendulum was observed through a microscope. About fifty years later, Zollner constructed a horizontal pendulum based on Hengler's concept and applied it to monitoring slow movements of the earth crust. The horizontal pendulum, as shown in Fig.2.3, consisted of a very rigid bracket fixed by a base plate to three leveling screws V_1, V_2 and V_3. At points A and B two metal wires were clamped and fixed at C and D to a horizontal metal beam. The axis of the rotation of the beam was therefore the line passing through A and B. One could make the axis almost vertical by suitably manipulating the leveling screws. The remaining angle between the line through A and B and the vertical determined the sensitivity of the horizontal pendulum. Since this angle was usually unknown after the pendulum was installed, the sensitivity was calibrated by measuring the free oscillation period of the pendulum. In order to determine the pendulum position, a mirror M was fixed on the beam so that the movement of the beam could be recorded optically by sending a light beam to the mirror. Since then developments have been made in the horizontal pendulum for the purpose of earth crust movement observation. Vanicek [2.18] studied the theoretical aspects of the horizontal pendulum. The problems of suspension material, calibration, mounting and recording were discussed by many investigators [2.19, 2.20, 2.21]. Anderson [2.22] investigated the dynamic response of the horizontal pendulum. It was found that the horizontal pendulum had a well–damped frequency characteristic by nature. In order to improve the linearity of the pendulum, Vogel and Anderson [2.23] constructed a servo–controlled system in which the sensor was placed on an expandable bearing plate whose tilt position could be changed by a pressure produced by a column of mercury. The pendulum position was sensed by an electro–optical sensor which provided a suitable servo signal to adjust the height of the mercury. Mentes [2.24] discussed the possibility of using a capacitive instead of an optical method. It was found that a capacitive sensor with oil as a dielectric was suitable for horizontal pendulums because of its insensibility to environmental parameters.

In 1961 Ostrovsky designed a tilt sensor which was constructed by suspending a pendulum horizontally from a vertical steel wire and two horizontal tungsten wires [2.17]. A light beam was sent to a mirror fixed on the pendulum. The reflected beam

was then measured by photocells. Bagmet [2.25] studied the drift of the sensor and found that the drift was not only caused by deformation of the frame due to temperature changes but also by the electronic amplifier. Skalsky and Soukup [2.26] calculated the sensitivity of the sensor and improved its performance by including the expandable bearing plate. In a comparative study between the vertical pendulum and the Ostrovsky's device, Shirokov and Anokhina [2.27] found that the vertical pendulum had a relatively better stability than Ostrovsky's horizontal pendulum. The accuracies were about the same. In 1970, Tsubokawa [2.28] presented an electromagnetic tilt sensor constructed with an aluminum plate supported by four metallic wires forming a cross–suspension. Inclination of the sensor was detected by a differential transformer. Damping effects were obtained by placing the system into a container which was filled with silicon oil.

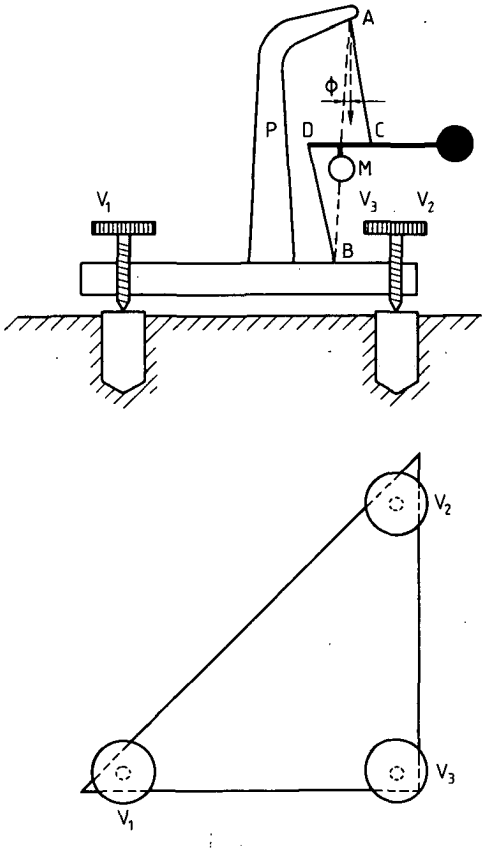

Fig.2.3 The horizontal pendulum [2.17].

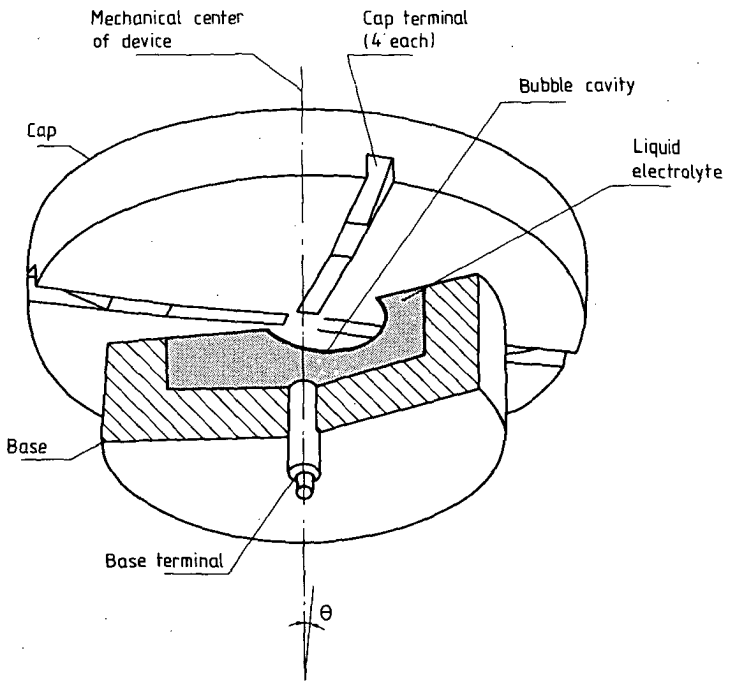

Fig.2.4 The biaxial tiltmeter with a resistive sensing method [2.30].

2.3 LIQUID BASED TILT SENSORS

2.3.1 Spirit level

electrolyte and resistive sensing

The earliest spirit level device capable of providing an electrical output signal is the so–called biaxial tiltmeter which was originally developed for use in inertial navigation systems by Autonetics, Rockwell International in 1958. The experimental results were first presented in 1970. In a review paper, Cooper [2.29] described the working principle and presented experimental data on the temperature dependence, sensitivity and stability of the sensor. As shown in Fig.2.4, the sensor consisted mainly of a glass

cavity with a spherical concave top partially filled with an electrolytic liquid. Four equally–spaced strip electrodes situated on the inner surface of the top and a circular electrode deposited on the bottom were connected in a resistive bridge. The bridge was balanced when the air bubble rested exactly at the center of the top and became unbalanced when the sensor was tilted. The resistive bridge had to be ac–excited to avoid polarization of the electrolyte. The dynamic responses of the sensor to tilt and horizontal acceleration could be expressed with second–order linear equations. Kohlenberger *et al.* [2.30] in 1973 and Kohlenberger [2.31] in 1975 discussed the frequency response of the sensor to tilt, horizontal acceleration, and horizontal displacement. They concluded that a tilt sensor with the basic construction of the spirit level acted as an overdamped fluid pendulum and exhibited a natural frequency of approximately 1 Hz. Cooper and Schmars [2.32] showed that the resolution limit of the sensor was of the order of 2×10^{-3} arcsec for a 1.25 kHz bandwidth. The predominant random noise limitations on the sensor were believed to be the Brownian random motion of the bubble and the thermal noise in the associated electronics [2.32, 2.33]. Because of its high sensitivity, stability and simplicity, many efforts have been made to prove the value of the biaxial tiltmeter in geophysical instruments for monitoring earthquakes and volcanos. Miller *et al.* [2.34] discussed the capability of the sensor used as a horizontal seismometer.

The biaxial tiltmeter was criticized by Westphal *et al.* [2.35] because it was "relatively expensive and not conveniently available". This might be the reason why later on single–axis tiltmeters were developed. As schematically shown in Fig.2.5, three wires (A, A', and B) were sealed into a glass tube to form three electrodes. The tube was partially filled with an electrically conducting liquid entirely covering wire B, but leaving a bubble into which wires A and A' penetrated. The glass tube of the sensor had a length of 30 mm, an outer diameter of 8 mm and a bore of 6 mm in diameter. The tube was bent to a radius of 355 mm. The nature of the wires, electrolyte and gas in the bubble and any special preparations of the glass tube remain classified information of the manufacturers. The sensor reported by Jones and McNaughton [2.36] was composed of electrodes made of platinum and a solvent (amyl isopropyl ketone) containing solutes of sodium iodide and iodine. The sensor was found to have about the same sensitivity and noise characteristics as the biaxial tiltmeter. The shortcomings of this kind of device are a wide spread of sensitivity and a large temperature coefficient when they are produced in large quantities. The temperature dependence of the sensitivity, which has been found to be as large as -1 %/^{0}C, was due to the changes in the conductivity of the electrolyte. While that of the offset, about -1.4 arcsec/^{0}C, was caused by an asymmetry in the glass tube.

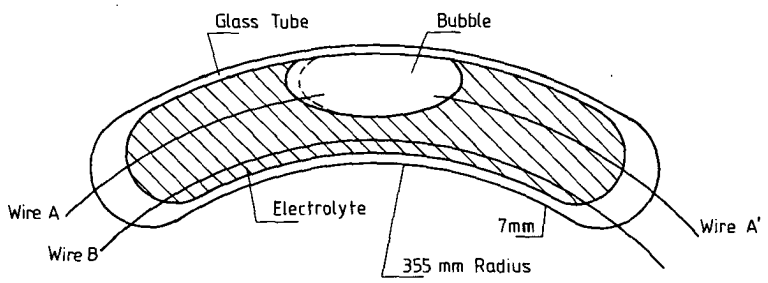

Fig.2.5 The single–axis tiltmeter [2.35].

Jardine *et al.* [2.37] in 1985 constructed a tilt sensor for the use of strain measurements in triaxial tests on weak rock. It consisted of a glass capsule containing electrolyte. Three electrodes were immersed in the liquid and the impedances between the central electrode and the two outer electrodes were measured. A similar device was constructed by Zhang [2.38] to monitor active earth flows in Raukumara Peninsula, New Zealand. The device had six carbon electrodes so that biaxial tilts could be measured. An interesting aspect of Zhang's tilt sensor was that the sixth electrode was used for temperature sensing. In the device the central electrode and the temperature electrode were fully immersed in the electrolyte, so that the conductivity between them did not change with tilt, but did change with temperature. This, therefore, could be used as a compensation signal for the temperature influence.

alcohol with optical sensing

In 1965 NASA [2.39] developed a biaxial tilt sensor which was a combination of a light source on the bottom, a four–quadrant photodetector on the top, and a spirit level in between. The light spot position on the photodetector was modulated by the air bubble. It determined the photocurrents in the four photocells. The accuracy was about 15 arcsec. Ernsberger [2.40] used a metal bullet instead of an air bubble as the mass element. It was placed in a closed container filled with a fluid to obtain a proper damping constant. The accuracy was about 2 degrees. The most recent design of this kind is by Kato *et al.* [2.41, 2.42] developed in 1986. As shown in Fig.2.6, the sensor consists of a GaAs light–emitting diode and a biaxial spirit level mounted on an SnO_2–Si four–quadrant photodetector. The composition of the liquid is ethanol with

$C_2H_5OH:H_2O$ = 3:1. The diameter of the hemispherical glass is 16 mm and that of the bubble in a horizontal position is 8 mm. The differences in the output currents between the opposite photodiodes are proportional to the differences in the area of the light spot image on the corresponding diodes. Up to an angle of 20 degrees the experimental values agree well with the calculated results which are obtained by using a simple model.

Clark [2.43] designed an optical plummet for the surveying of mountainous and jungle–covered regions by helicopter. The device was made of a container with two separated compartments containing two kinds of liquid with carefully chosen indices. When observing the ground through a telescope mounted on the container, the deviation of the device from the vertical was approximately the same as the tilt angle. In combination with a position–sensitive detector (PSD), Reid *et al.* [2.44] in 1985 constructed an optical tilt sensor based on a single–axis spirit level with opaque liquid. The light from a line filament lamp was focused by a cylindrical lens and the image of the bubble was projected on the PSD. A resolution of 0.1 % of the measurement range was achieved.

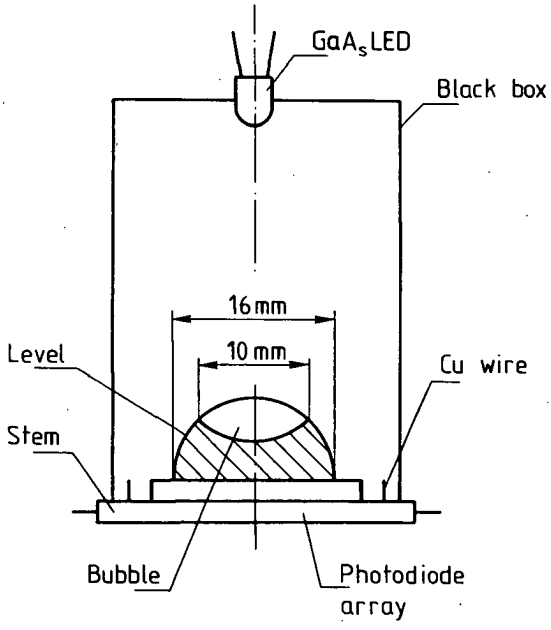

Fig.2.6 The biaxial tilt sensor with an optical sensing method [2.41].

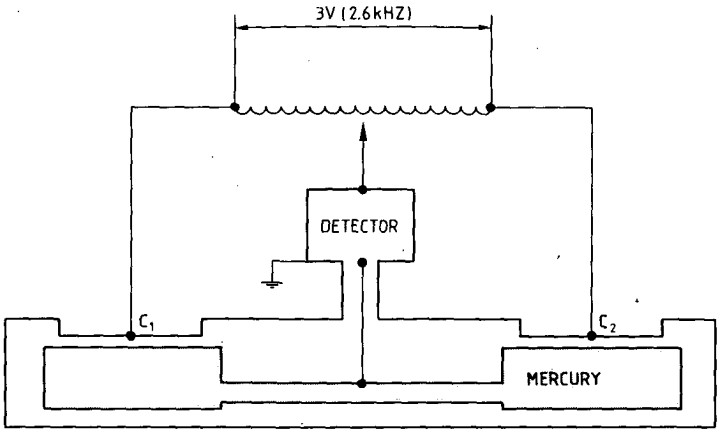

Fig.2.7 Principle of the mercury level tiltmeter [2.48].

2.3.2 Liquid level

Unlike the spirit levels, which measure centimeters or less in size, liquid levels are usually large and heavy. The earliest devices might be the water–levels which were designed for the observation of earth tides [2.45, 2.46, 2.47]. In most cases these instruments did not provide electrical output signals and the water level was observed by human eyes. In 1969, Stacey [2.48] constructed a tilt sensor based on the same principle, but in his device mercury instead of water was used as the working liquid. The sensor consisted of two shallow mercury pools connected by a capillary tube, as shown in Fig.2.7. Electrodes were provided on top of each pool while the mercury surface served as the common electrode. When the device was tilted, the capacitances of the two electrodes to the common electrode became different. A measurement range of 0.6 degrees and a resolution of 2×10^{-4} arcsec were reported to have been achieved. Since the viscosity of the mercury cannot be changed, the required damping of the mercury oscillation between the pools was obtained by properly choosing the dimensions of the tube. Roger *et al.* [2.49] found that the mercury level dropped by approximately 20 μm over a one month period as a result of reduced surface tension due to contamination. This consequently led to changes in the sensor gain constant. McGarr and Green [2.50] used this device in a gold mine to detect tilts due to enlargement of mine excavation.

Besides the capacitive sensing method, an optical sensing method can be used in combination with mercury as well, since a clean mercury surface works like a mirror. Masry [2.51] placed a mercury pool on a carriage in order to measure the rotation around its travel direction. A light beam was sent to the mercury pool and the reflected light was received by an autocollimator. A similar device was constructed by Gort [2.52] in which a light–emitting diode was suspended vertically above a mercury pool while photodetectors, placed on top of the device, detected the reflected light. The device had a measurement range of 0.04 degrees and an accuracy of 2 arcsec.

2.4 OTHER DEVICES USED FOR TILT MEASUREMENT

2.4.1 Accelerometers

Tilt sensors are sensitive to accelerations, and accelerometers also provide an output component which is dependent on the tilt angle. Since the gravitational acceleration is known, the tilt of the sensitive axis of the accelerometer with respect to the horizontal can readily be obtained. The basic structure is a pendulum mass restrained in a housing by mechanical or electromagnetic means [2.53, 2.54, 2.55]. The sensor has to be mounted with its sensitive axis in a horizontal position and the output is a sine function of the tilt angle. Recent developments on integrated silicon accelerometers [2.56, 2.57] and fiber–optic accelerometers [2.58, 2.59] have shown the possibility of constructing tilt sensors using various principles. The integrated accelerometers possess the advantages of small size and being batch fabricatable, while the fiber–optic accelerometers are well protected from electromagnetic interference.

2.4.2 Gyros

Gyroscopic instruments are relative–motion measurement instruments since the orientation of the reference can arbitrarily be determined. The simplest configuration is perhaps the free gyro which is able to measure the angular displacement of a vehicle to which it is attached. A single free gyro can measure rotation around two perpendicular axes. The measurement range cannot exceed 10 degrees when precision is expected because of the interaction between the two angular motions. Rather than

using free gyros to measure angular displacements in two directions, recent high performance systems utilize single–axis or constrained gyros [2.10]. The constrained gyros can be divided into two groups: the rate gyro and the rate–integrating gyro. The rate gyro measures absolute angular velocity and is widely used to generate stabilizing signals in vehicle–control systems. The rate–integrating gyro measures absolute angular displacement and thus is used as a fixed reference in navigation and attitude–control systems. Compared with a tilt sensor, the advantages of gyros are apparently the high accuracy and the absence of interference with acceleration inputs. A shortcoming of gyros is the gradual drift of orientation of the rotating axis which is used as the reference, resulting in the necessity for maintenance after a period of operation.

2.5 SUMMARY

In Table 2.1, construction aspects of several tilt sensors are listed. The sensitivity of the tilt sensor is, in the first place, related to its measurement range. Tilt sensors with a small measurement range usually have a high sensitivity, while those with a large measurement range have a low sensitivity.

Throughout history the most frequently used gravitation–orientation sensing units have been the pendulum based and the liquid based type. An advantage of the pendulum based type is that the position of the pendulum can be detected by relatively simple means. The sensitivity of the unit can be increased by either enlarging the length of the pendulum arm or by using a different construction, such as the horizontal pendulum. The resistive position–sensing method is frequently used in sensors with a large measurement range because of the desired linear relationship between input and output. For tilt sensors with a small measurement range and a high resolution, the noncontact position–sensing methods, such as the capacitive, optical or inductive methods, are more suitable. The horizontal pendulum is by nature a well–damped device, whereas an additional damping effect is required in most of the vertical pendulums. This is achieved by using viscous fluids, mechanical springs and/or magnetic coils with feedback circuits. A shortcoming of the pendulum based tilt sensor is the mechanical friction at the pivot point and at the contact point of the wiper with the resistive element.

The problem of the mechanical friction is very much reduced in tilt sensors based on liquids. The liquids can be electrolyte, alcohol, water or mercury. The sensitivity of the spirit level type tilt sensor can be increased by enlarging the radius of the curvature of the vial, while the sensitivity of the liquid level type can be increased by enlarging the base line of the liquid container. The resistive sensing method is widely used because of its simple construction. A drawback is the temperature dependence of the sensitivity and drift. This problem does not occur in tilt sensors utilizing an optical sensing method. But, on the other hand, as a light source is required, the lifetime of the sensor will possibly be determined by that of the light source. A comparatively higher power consumption can also be expected. The spirit level tilt sensor has, basically, a very good dynamic behavior. In comparison, a tilt sensor based on mercury needs a special construction to achieve the damping effect.

Table 2.1 Construction aspects of several tilt sensors

author	sensing unit	position sensing	damping method	range	remarks	source
Flach	pendulum	capacitive optical	electro–magnetic fluid	small	–	[2.8]
Doebelin	pendulum	resistive	fluid, spring	large	–	[2.9]
Masuda Murakami	pendulum	magneto–resistive	viscous fluid	large	noncontact	[2.12] [2.13]
Simon	pendulum	optical	electro–magnetic	–	noncontact	[2.14]
Melchior	horizontal pendulum	capacitive optical	–	small	very sensitive	[2.17]
Vogel	horizontal pendulum	optical	–	small	zero method	[2.19]
Cooper Westphal	electrolyte	resistive	–	small	single axis or biaxial	[2.29] [2.35]
Jones	electrolyte	resistive	–		zero method	[2.36]
Zhang	electrolyte	resistive	–	small	temperature compensated	[2.38]
NASA Kato Reid	opaque liquid	optical	–	small	single axis or biaxial	[2.39] [2.41] [2.44]
Stacey	mercury	capacitive	pipe	small	–	[2.48]

Reference

[2.1] P. H. Sydenham, "Linear and angular transducers for positional control in the decametre range", Proc. IEE, Vol.115, pp.1056–1066, 1968.

[2.2] R. V. Allen, D. M. Wood and C. E. Mortensen, "Some instruments and techniques for measurements of tidal tilt", Phil. Trans. R. Soc. Lond. A., Vol.274, pp.219–222, 1973.

[2.3] R. V. Jones, "The measurement and control of small displacements", Phys. Bull., Vol.18, pp.325–336, 1967.

[2.4] P. Melchior, "The tides of the planet earth", Pergamon Press, Oxford, 1978.

[2.5] M. Bonatz, "Clinometer measurement with Askania vertical pendulum (borehole tiltmeter) Gbp 1 No. 12 in the test station Erpel", Proc. 7th Int. Sym. on Earth Tides, Sopron, pp.235–241, 1973.

[2.6] J. Zschau, "A calibration–, compensation– and damping device for the Askania borehole tiltmeter", Proc. 7th Int. Sym. on Earth Tides, Sopron, pp.313–326, 1973.

[2.7] D. Flach and W. Grobe–Brauckmann, "An electronic filter and damping system for the Askania borehole tiltmeter", J. Geophys., Vol.41, pp.303–310, 1975.

[2.8] D. Flach, "Present state of the development of the Askania borehole tiltmeter", Proc. 7th Int. Sym. on Earth Tides, Sopron, pp.249–258, 1973.

[2.9] E. O. Doebelin, "Measurement systems: application and design", McGraw–Hill, New York, 1983.

[2.10] Product Data, Penny & Giles Potentiometers Ltd., U.K., 1983.

[2.11] Product Data, Slope Indicator Company, U.S.A., 1976.

[2.12] N. Masuda, "Contactless potentiometers moving into industrial equipment field", JEE, Vol.18, pp.76–79, 1981.

[2.13] K. Murakami, "Applications growing for contactless potentiometer", JEE, Vol.20, pp.73–77, 1983.

[2.14] I. Simon, A. G. Emslie, P. F. Strong and R. K. McConnell, "Sensitive tiltmeter utilizing a diamagnetic suspension", Rev. Sci. Instrum., Vol.39, pp.1666–1671, 1968.

[2.15] "Electronic inclinometer eliminates field leveling requirements", Defense Electronics, Vol.11, no.12, p.37, 1979.

[2.16] S. D. Wilson and P. E. Mikkelson, "Foundation instrumentation – inclinometers", Shannon & Wilson, Inc., Geotechnical Consultants, Seattle, 1977.

[2.17] P. Melchior, "The earth tides", Pergamon Press. Ltd., Oxford, 1966.

[2.18] P. Vanicek, "Theory of motion of horizontal pendulum with Zollner suspension", Proc. 6th Int. Sym. on Earth Tides, Strasbourg, pp.180–182, 1969.

[2.19] A. Vogel, "A horizontal pendulum station with tilt compensation", Proc. 6th Int. Sym. on Earth Tides, Strasbourg, pp.213–215, 1969.

[2.20] G. Alpar, "Investigations to the development of Zollner–suspension horizontal pendulums", Act. Geod. Geophys. & Mont., Vol.10, pp.329–337, 1975.

[2.21] H. Schlemmer, "Some instrumental experiences", Proc. 7th Int. Sym. on Earth Tides, Sopron, pp.267–272, 1973.

[2.22] A. J. Anderson, "Dynamic response of a quartz horizontal pendulum system", Proc. 7th Int. Sym. on Earth Tides, Sopron, pp.197–203, 1973.

[2.23] K. A. Vogel and A. J. Anderson, "An improved servo–controlled tiltmeter system and latest measurements in Sweden", Phil. Trans. R. Soc. London. A., Vol.274, pp.305–309, 1973.

[2.24] G. Mentes, "Horizontal pendulum with capacitive transducer", Act. Geod. Geophys. & Mont., Vol.16, pp.269–280, 1981.

[2.25] A. L. Bagmet, "On the study of instrument drift of tiltmeter", Proc. 7th Int. Sym. on Earth Tides, Sopron, pp.205–221, 1973.

[2.26] L. Skalsky and V. Soukup, "Photo–electric compensating tiltmeter", Proc. 7th Int. Sym. on Earth Tides, Sopron, pp.291–299, 1973.

[2.27] I. A. Shirokov and K. M. Anokhina, "On the comparative observations of tidal tilts by Askania borehole tiltmeter", Proc. 7th Int. Sym. on Earth Tides, Sopron, pp.285–289, 1973.

[2.28] L. Tsubokawa, "A new type electromagnetic tiltmeter", Proc. 6th Int. Sym. on Earth Tides, Strasbourg, pp.217–218, 1969.

[2.29] G. L. Cooper, "Development and use of a two–axis electrolytic bubble level as a precision vertical reference and tilt indicator", Technical Report for Guidance, Control and Flight Mechanics Conference of AIAA, Autonetics, Anaheim, Calif., pp.1–11, 1970.

[2.30] C. W. Kohlenberger, G. L. Cooper and W. T. Schmars, "Dynamic properties of a new biaxial tiltmeter", Autonetics Technical Report for Seismological Society of America Meeting, Colorado, pp.1–5, 1973,.

[2.31] C. W. Kohlenberger, "Tiltmeter dynamics related to PVM–10 and PVM–11 motion tests", Autonetics Internal Technical Report, Anaheim, pp.1–11, 1975.

[2.32] G. L. Cooper and W. T. Schmars, "Selected applications of a biaxial tiltmeter in the ground motion environment", J. Spacecr. & Rockets, Vol.11, pp.530–535, 1974.

[2.33] F. Wyatt and J. Berger, "Comments on 'Use of a bubble tiltmeter as a horizontal seismometer' by Miller *et al.*", Geophys. J. R. Astr. Soc., Vol.59, pp.411–413, 1979.

[2.34] W. F. Miller, R. J. Gerller and S. Stein, "Use of a bubble tiltmeter as a horizontal seismometer", Geophys. J. R. Astr. Soc., Vol.54, pp.661–668, 1978.

[2.35] J. A. Westphal, M. A. Carr, W. F. Miller and D. Dzurisin, "Expendable bubble tiltmeter for geophysical monitoring", Rev. Sci. Instrum., Vol.54, pp.415–418, 1983.

[2.36] B. E. Jones and H. M. McNaughton, "An investigation of open and closed loop tilt monitors employing electrolytic spirit levels", J. Phys. E: Sci. Instrum., Vol.7, pp.582–585, 1974.

[2.37] R. J. Jardine, N. J. Brooks and P. R. Smith, "The use of electrolevel transducers for strain measurements in triaxial test on weak rock", Int. J. Rock Mech. Min. Sci. Geomech. Abstr., Vol.22, pp.331–337, 1985.

[2.38] X. Zhang, "A low–cost electrolytic tiltmeter for measuring slope deformation", Geotech. Testing J., Vol.10, no.2, pp.91–94, 1987.

[2.39] "Bubble forms tilt–responsive lens", Machine Design, Vol.37, p.214, April, 1965.

[2.40] K. Ernsberger, "Kugellotsensor – eine kostengunstige Alternative zu manchen Kreiselanwendungen auf Schiffen", Proc. Tagung Sensoren, Basel, pp.50–62, 1983.

[2.41] H. Kato, M. Kojima and S. Sasaki, "Photoelectric inclination sensor", Rev. Sci. Instrum., Vol.57, pp.1207–1208, 1986.

[2.42] H. Kato, M. Kojima and S. Sasaki, "Photoelectric inclination sensor", Proc. 6th Jap. Sensor Sym., Nagoya, pp.299–303, 1986.

[2.43] B. A. J. Clark, "An optical plummet", J. Sci. Instrum., Vol.44, pp.744–746, 1967.

[2.44] G. T. Reid, H. Messer and H. Stewart, "Optical sensors for position and displacement measurement", Proc. 7th Int. Conference on Automated Inspection and Product Control, Birmingham, pp.323–330, 1985.

[2.45] P. H. Sydenham, "Transducers in measurement and control", Adam Hilger Ltd, Bristol, 1980.

[2.46] D. R. Bower, "A sensitive water–level tiltmeter", Phil. Trans. R. Soc. Lond. A., Vol.274, pp.223–226, 1973.

[2.47] P. H. Sydenham, "Microdisplacement transducers", J. Phys. E: Sci. Instrum., Vol.5, pp.721–735, 1972.

[2.48] F. D. Stacey, J. M. W. Rynn, E. C. Little and C. Croskell, "Displacement and tilt transducers of 140 db range", J. Phys. E: Sci. Instrum., Series 2, Vol.2, pp.945–949, 1969.

[2.49] J. S. Rogers, C. U. Park and F. W. Jones, "Test cell results for a mercury–level tiltmeter", J. Phys. E: Sci. Instrum., Vol.13, pp.161–162, 1980.

[2.50] A. McGarr and R. W. E. Green, "Measurement of tilt in a deep–level gold mine and its relationship to mining and seismicity", Geophys. J. R. Astr. Soc., Vol.43, pp.327–345, 1975.

[2.51] S. E. Masry, "Accurate method for measuring rotational movement of a carriage", Rev. Sci. Instrum., Vol.38, pp.1651–1653, 1967.

[2.52] A. F. Gort, "A fully integrated microprocessor–controlled total station", Hewlett–Packard J., pp.3–17, 1980.

[2.53] E. E. Ambrosius, R. D. Fellows, A. D. Brickman, "Mechanical measurement and instrumentation", The Ronald Press Company, New York, 1966.

[2.54] G. H. van Zeggelaar, "Angle– and tilt measurement in civil engineering", Proc. Sensors & Actuators Sym., Enschede, pp.153–158, 1984.

[2.55] P. L. Chen, R. S. Muller, R. D. Jolly, G. L. Halac, R. M. White, A. P. Andrews, T. C. Lim and M. E. Motamedi, "Integrated silicon microbeam PI–FET accelerometer", IEEE Trans. on Electron Devices, Vol.ED–29, pp.27–33, 1982.

[2.56] L. M. Roylance and J. B. Angell, "A batch–fabricated silicon accelero–meter", IEEE Trans. on Electron Devices, Vol.ED–26, pp.1911–1917, 1979.

[2.57] P. L. Chen and R. S. Muller, "Integrated silicon PI–FET accelerometer with proof mass", Sensors and Actuators, Vol.5, pp.119–126, 1984.

[2.58] A. B. Tveten, A. Dandridge, C. M. Davis, T. G. Giallorenzi, "Fibre optic accelerometer", Electronics Letters, Vol.16, pp.854–856, 1980.

[2.59] S. Tai, K. Kyuma and M. Nunoshita, "Fiber–optic acceleration sensor based on the photoelectric effect", Appl. Opt., Vol.22, pp.1771–1774, 1983.

CHAPTER 3 THE GRAVITATION–ORIENTATION SENSING UNIT

3.1 INTRODUCTION

In this chapter the gravitation–orientation sensing unit, the vial with the working liquid, is first considered. A criterion motivating the choice of a proper working liquid is established. Since an optical method is used for the determination of the air bubble position, physical properties of the liquid, such as mass density, surface tension, and viscosity are of great concern. In section 3.2, a comparative study is made between mercury and alcohol. The light source is also treated in this chapter because of its close tie with the working liquid. The radiation power of the light source, the uniformity of illumination of the vial by the light source, and the spectral density distribution affect the accuracy of the sensor considerably. In case of using a transparent liquid, liquid dye must be used. The functional aspects of the light source and the liquid dye are dealt with in section 3.3. In section 3.4, the dynamic response of the tilt sensor is evaluated. The dynamic property of the tilt sensor is mainly determined by the gravitation–orientation sensing unit. The primary aim of the dynamic analysis concerns the damping effect in the tilt sensor. A simple model is established to describe the dynamic response of and to estimate the damping effect in the tilt sensor.

In the experiments described in this chapter, a light spot position–sensing unit is used. The photocurrent generated in the unit is proportional to the light intensity. After signal processing, the position–sensing unit is able to provide an output signal which is a linear function of the center of gravity of the density of an incident light spot. The performance of the position–sensing unit, the fabrication procedure of the vial, and the construction of the tilt sensor will be described in the following chapters.

3.2 THE WORKING LIQUID AND THE VIAL

Due to the presence of the gravitational field, liquids always tend to keep their surfaces horizontal. However, when a liquid surface approaches a solid surface, it is bent upwards or downwards as the result of surface tensions. In the tilt sensor, the gravitational force is the driving force for the liquid mass, whereas the surface tension is the counter–acting force which tends to hold the liquid in its original position.

3.2.1 The contact angle and the contact angle hysteresis

The case where an air bubble is captured in a solid–liquid system as shown in Fig.3.1(a) is considered. As a result of the mechanical equilibrium between solid, liquid and vapor, the following equation was proposed to hold at the joined interface of the three phases by Young in 1805:

$$\gamma_{SL} - \gamma_{SV} + \gamma_{LV}\cos\theta_c = 0 \tag{3.1}$$

where γ_{SL}, γ_{SV} and γ_{LV} are the surface tensions at the interfaces between the solid, liquid and vapor, respectively. θ_c is the contact angle defined between the surfaces of the solid and the liquid. However, the contact angle θ_c cannot exactly be determined in many cases [3.1]. As shown in Fig.3.1(b), when the solid surface is tilted, the air bubble does not slip away immediately but elongates in the direction of the tilt. Two contact angles can be found, one at the front of the bubble and one at its tail. These contact angles are described as the advancing angle θ_A and the receding angle θ_R. The

advancing angle decreases and the receding angle increases as the tilt angle increases. The bubble is deformed and starts to move only when a critical tilt angle is reached. This phenomenon is called the contact angle hysteresis [3.1, 3.2].

Attempts have been made to establish relationships between the contact angle of Young, the advancing and receding angles, and the tilt angle of the solid surface [3.3]. Furmidge [3.4] derived an expression for the case of a liquid droplet resting on a solid plate using the assumption that the base of the droplet on the plate was a rectangle. The same expression is used here for the description of the air bubble captured in the vial, which gives:

$$(3.2) \qquad mg\sin\alpha = \gamma_{LV} w (\cos\theta_A - \cos\theta_R)$$

where m is the buoyant mass of the air bubble, g the gravitational acceleration, α the tilt angle, and w the width of the bubble. The physical meaning of Eq.(3.2) can easily be seen as the quantity $mg\sin\alpha$ is the component of the buoyant force on the bubble parallel to the solid surface, while $\gamma_{LV} w (\cos\theta_A - \cos\theta_R)$ is the force exerted on the bubble to hold it in position. When the contact angle of Young is zero, the advancing and the receding angle are normally also zero.

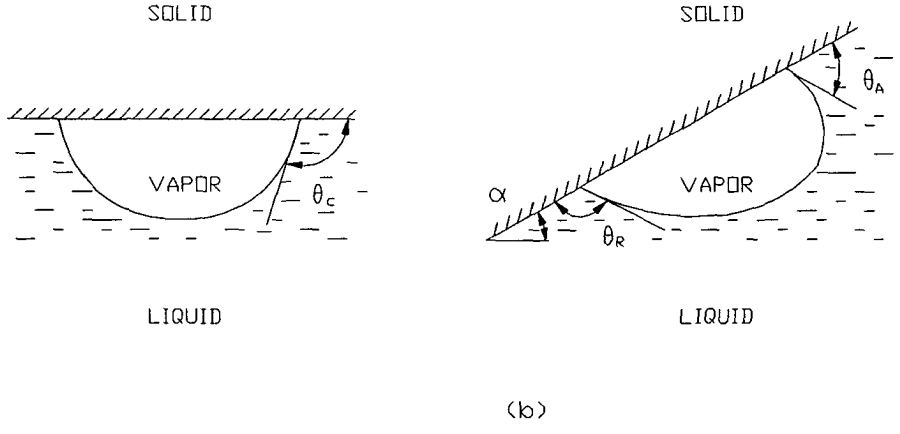

Fig.3.1 *An air bubble captured in a solid–liquid system, where (a) the solid surface is in a horizontal position, and (b) the solid surface is tilted an angle α.*

The contact angle hysteresis of the liquid leads to an undesired deformation of the shape as well as to a hysteretic motion behavior of the air bubble. The selection criterion for the working liquid can be established if we define a parameter C_r by rewriting Eq.(3.2) as:

$$(3.3) \qquad C_r = \frac{\gamma_{LV}{}^{w}}{mg}(cos\theta_A - cos\theta_R)$$

In an ideal case C_r must be zero. Equation (3.3) shows that, in order to ensure a smooth motion behavior of the air bubble, liquids must be used which have a small ratio between the surface tension and the mass density, as well as an equal advancing and receding angle.

3.2.2 The working liquid and the vial

The contact angle and the contact angle hysteresis depend greatly on the properties of the solid and the liquid, and on the conditions of their surfaces. For instance, for a water droplet on a clean and carefully polished glass plate, a zero contact angle can be observed. But the contact angle can be as large as 160 degrees and a contact angle hysteresis of several degrees can be observed when the glass plate is replaced by a plate made of wax. Mercury is usually regarded as a liquid which can easily have a large contact angle with glass because of the presence of its oxygen–contaminated surface when exposed to air, but it has also been reported that highly purified mercury does wet glass [3.5]. In contrast, the contact angle between the surfaces of alcohol and glass is zero under normal conditions.

The origin of the contact angle hysteresis, on the part of the solid, is thought to be the roughness of the solid surface. It was found, based on simple mathematical models, that several metastable states with local free energy minima for certain contact angles could exist, depending on the size and shape of the roughness [3.6]. The energy barriers between the states and the capacity of the liquid to overcome them provide a plausible explanation of the contact angle hysteresis. In practice, it appears that the cleaner and the smoother the solid surface is, the smaller the contact angle and the contact angle hysteresis will be.

Table 3.1 *The density (ρ), viscosity (μ), surface tension (γ_{LV}) and contact angles with glass of various liquids at room temperature.*

liquid	ρ g/cm^3	μ g/cm/s	γ_{LV} Dynes/cm	θ_c deg	θ_A deg	θ_R deg	reference
mercury	13.6	0.016	435.5	128–148	118	139	[3.7],[3.8] [3.9],[3.10]
water	1.00	0.010	74.2	≈ 0	–	–	[3.7],[3.6] [3.10]
ethanol	0.791	0.012	23.0	0	–	–	[3.7],[3.5]
methanol	0.810	0.060	22.7	0	–	–	[3.7]

The density, viscosity, surface tension and contact angles with glass for mercury, water and alcohol, respectively, are listed in Table.3.1. The advancing and receding angles given in the table are the minimum advancing angle and the maximum receding angle, respectively. The large deviation in the experimental data of the contact angle of mercury is attributed to surface contamination, which is difficult to control. Mercury has the largest mass density but also the largest surface tension and a large contact angle hysteresis, so that the parameter C_r in Eq.(3.3) is very large. Water has a very small contact angle with glass, but the ratio between the surface tension and the mass density of water is larger than that of alcohol.

3.2.3 Experimental results

In order to investigate the motion behavior of the air bubble, experiments are carried out with mercury and alcohol as the working liquids, and with vials made of glass, perspex (PMMA) and polyvinylchrolide (PVC). PMMA is easy to handle but less resistive to alcohol. Glass is well resistive to alcohol but black glass has a low absorption coefficient for infrared. PVC has a wide absorption spectrum and is well resistive to alcohol at temperatures up to 60 ^{0}C. In the experiment with mercury, a glass vial is used. The vial is cleaned with fuming nitric acid, rinsed with distilled water and then heated up to 100 ^{0}C to dry it. In the experiments with alcohol, vials made of glass, PMMA and/or PVC are used. The vial is rinsed several times in alcohol, then dried by blowing condensed air onto its surfaces. Mercury is purified by oxygen bubbling for 22 hours. 97 % ethanol is used.

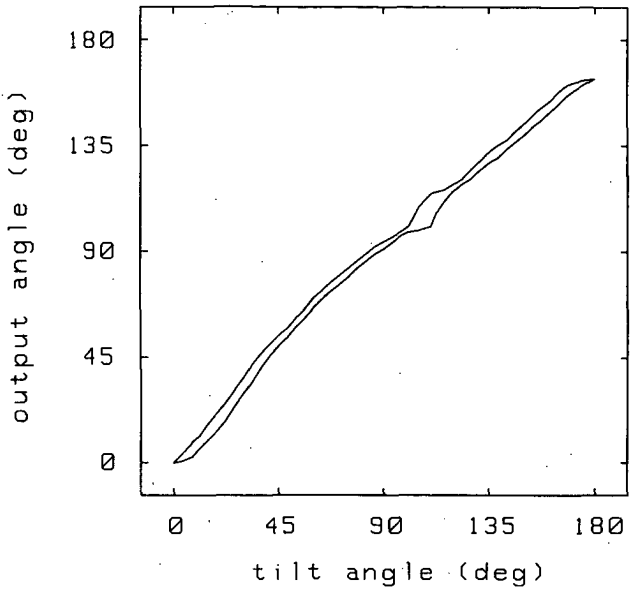

(*a*)

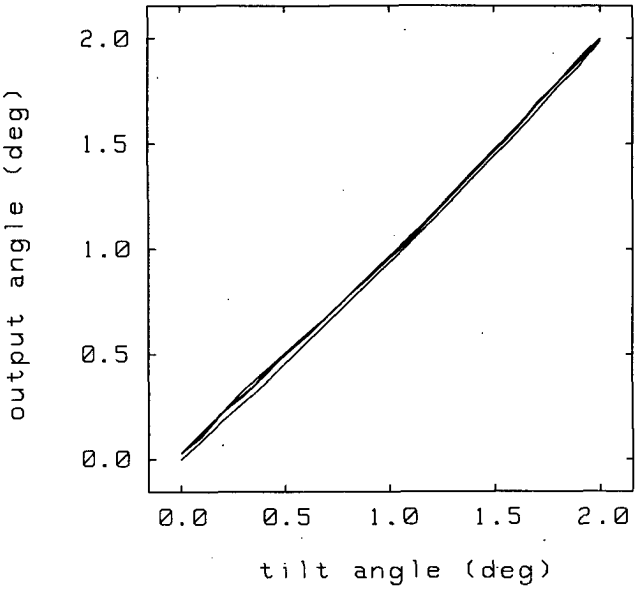

(*b*)

Fig.3.2 *Experimental results with (a) mercury and (b) alcohol as the working liquids in a glass vial. The angular position of the air bubble is measured as a function of the tilt angle.*

In the experiments, a light beam derived from an He–Ne laser is diffused by a lens and is projected on the vial. A light image of the air bubble is formed on the position–sensing unit. The angular position of the center of gravity of the light spot is measured as the output angle. The measurements are carried out by rotating the vial forwards and backwards several times. The measurement results are shown in Fig.3.2. From Fig.3.2(a) it can be seen that, when mercury is used as the working liquid, a large hysteresis in the output signal occurs. This is the result of the hysteretic motion behavior of the mercury. In experiments with alcohol, as shown in Fig.3.2(b), the phenomenon of hysteresis is very small. Experiments carried out with alcohol in vials made of PMMA and PVC also show similar results.

3.3 THE LIGHT SOURCE AND THE LIQUID DYE

In order to obtain a light image of the air bubble on the position–sensing unit, the vial with the working liquid is illuminated by a light source. Since the position–sensing unit detects the center of gravity of the density of a light spot, a uniform illumination of the vial is required. When the illumination is nonuniform, the center of gravity of the light density will deviate from the geometric center of the light spot, which causes measurement errors. Since alcohol is a transparent liquid, liquid dye must be used. The dye must be well soluble in alcohol and able to absorb the incident light over the spectrum of interest. The solution must be stable under normal operational conditions.

3.3.1 The light source

Experiments have been carried out with infrared light–emitting diodes (GaAlAs IRLED's) and miniature incandescent lamps made of tungsten–wire filaments with a low operational voltage. The IRLED (type OD100) has a maximum optical output power of 160 mW with a voltage of 4.5 V and a current of 300 mA. The distribution of the spectral density has its maximum at the wavelength of 880 nm. The incandescent lamp has an operational voltage of 6 V and a current of 200 mA. The radiation of the tungsten filament around the visible light region is very similar to that of a greybody [3.11]. The lifetime of the lamp is 20,000 hours, while that of the IRLED is longer than 100,000 hours.

The effect of a nonuniform illumination of the vial on the accuracy of the sensor is estimated as follows. A nonuniform illumination of the vial results in a variation of light density within the light spot. In the practical design of the sensor, the center of the light source is aligned with that of the vial. A cylindrical coordinate system thus can be defined at the center of the vial. Since the air bubble is moved around the center of the vial, only the light density variation along the circular track of the air bubble is of interest. Suppose that the density of the photocurrent generated in the position–sensing unit can be expressed by a constant component J_0 superimposed by a position–dependent component J_d: $J = J_0 + J_d(\phi)$, then the position of the center of gravity of the light spot ϕ_g measured by the position–sensing unit is given by:

$$(3.4) \qquad \phi_g = \frac{\int_{\phi_1}^{\phi_2} \phi J \, d\phi}{\int_{\phi_1}^{\phi_2} J \, d\phi} = \frac{\alpha\phi_e J_0 + \int_{\phi_1}^{\phi_2} \phi J_d \, d\phi}{\alpha J_0 + \int_{\phi_1}^{\phi_2} J_d \, d\phi}$$

where ϕ_1 and ϕ_2 are the coordinates of the two edges of the light spot with $\phi_1 < \phi_2$, α is the width of the light spot with $\alpha = \phi_2 - \phi_1$, ϕ_e is the geometric center of the light spot with $\phi_e = (\phi_2 + \phi_1)/2$. All the coordinates are normalized to the measurement range and have a maximum value of unity. The integrals in Eq.(3.4) can be expanded in terms of α by using the square rule. Neglecting the terms including α of the order three and higher, the error $\Delta\phi = | \phi_g - \phi_e |$ caused by the nonuniform illumination is obtained:

$$(3.5) \qquad \Delta\phi \approx \left| \frac{\alpha^2}{12 J_0} \frac{d}{d\phi} J_d(\xi) \right| \approx \left| \frac{\alpha \Delta J_{max}}{12 J_0} \right|$$

with $\phi_1 < \xi < \phi_2$. In Eq.(3.5) assumptions are made that $\alpha << 1$ and $J_0 >> \Delta J_{max}$, with ΔJ_{max} the maximum variation of the light density within the light spot.

3.3.2 The liquid dye

The absorption spectrum of dye is determined by the optical density A, which is given by the Lambert–Beer's law [3.12]:

$$A = \epsilon\, c_d d_v \tag{3.6}$$

where ϵ is the absorption coefficient, c_d the dye concentration and d_v the thickness of the vial containing the opaque liquid. Since the thickness of the vial is a geometric constraint which cannot be varied greatly, the selection criteria of a dye must be based on its absorption coefficient and its solubility in alcohol. The relation between the optical density A and the light transmission ratio T through the dye solution is:

$$T = 10^{-A} \tag{3.7}$$

If I_{phd} is the photocurrent generated in the position–sensing unit by the light through the dyed liquid, and I_{phl} is the photocurrent generated in this unit by the light through the air bubble, then a ratio can be defined as:

$$\frac{I_{phd}}{I_{phl}} = \frac{A_d \sum_i J_i T_i \eta_i \lambda_i}{A_l \sum_i J_i \eta_i \lambda_i} \tag{3.8}$$

where J_i, T_i and η_i are the spectral density of the light source, the transmission ratio of the dyed liquid, and the spectral sensitivity of the position–sensing unit at a small interval around the wavelength λ_i, respectively. A_d is the active area of the position–sensing unit screened by the dyed liquid, and A_l is that illuminated by the light through the air bubble. It is desired to have the ratio as small as possible.

Four dyes soluble in alcohol are listed in Table 3.2. Their solubility in alcohol and fastness are given. The optical densities are shown in Fig.3.3.

Table 3.2 Properties of the dyes

dye	Color Index no.	solubility in ethanol (g/l)	fastness light	fastness heat	source
Malachite Green Base	Solvent Green 1 42000B	4	poor	60 °C	ICI
Waxoline Green AS	Solvent Green 3 61565	slightly soluble	good	155°C	ICI
Methasol Nigrosine	Solvent Black 5 50415	15 – 70	good	150°C	ICI
Nigrosine S. S.	Solvent Black 5 50415	15 – 70	good	150°C	NVCI

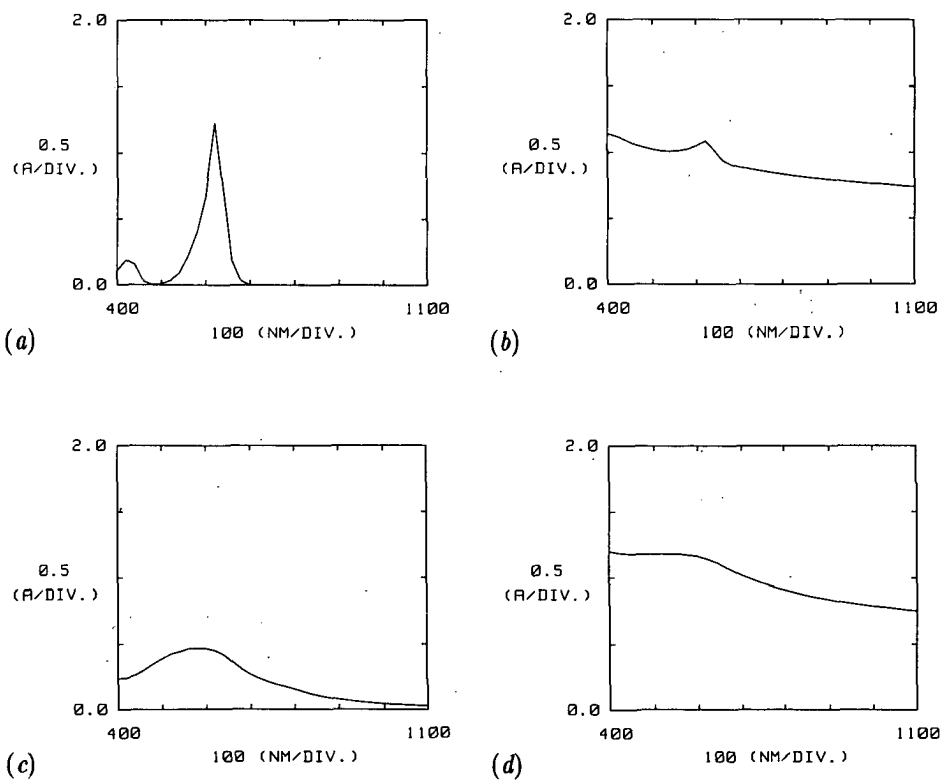

Fig.3.3 Optical densities of various dyes: (a) Malachite Green, $c_d = 10$ mg/l, (b) Waxoline Green AS, $c_d = 56$ mg/l, (c) Nigrosine Spirit Soluble, $c_d = 11$ mg/l, and (d) Methasol Nigrosine, $c_d = 11$ mg/l.

Malachite Green is used in carbon copying papers, typewriter ribbons and inks for ball–point pens. Waxoline Green AS is used for coloring petrol, polishes and soap. There is a maximum in the optical density of Malachite Green at the wavelength of 622 nm, whereas Waxoline Green AS has a fairly smooth absorption curve over a wide spectrum extending to the infrared region. A shortcoming of Waxoline Green AS is its relatively low solubility in alcohol. Nigrosine Spirit Soluble and Methasol Nigrosine are both from the same group given in the Color Index. Nigrosine is made by heating together nitrobenzene, aniline and aniline hydrochloride with iron or copper at temperatures from 180 to 200 ^{0}C. Compounds containing oxazine and diaxine ring systems are thought to be present [3.13]. The chief use of Nigrosine Spirit Soluble is as black in shoe polish. Both dyes are described by the manufacturers as very soluble in alcohol. From Fig.3.3 we can see that Methasol Nigrosine absorbs infrared radiation better than Nigrosine Spirit Soluble as the optical density of the latter decreases more steeply after reaching a maximum at the wavelength of 568 nm. Also in an absolute sense the optical density obtained with Methasol Nigrosine with the same concentration of dye is nearly twice as high as that of Nigrosine Spirit Soluble. Therefore, Methasol Nigrosine is considered to be the best dye of the four for the application to the tilt sensor.

3.3.3 Experimental results

The uniformity of the illumination of the vial by the light source is experimentally examined by moving a pin–photodiode around the center of the light source at a radial distance of 4 mm. The distance between the light source and the center of the circular track of the photodiode is 20 mm. During the measurement, the vial without liquid is placed between the light source and the photodiode. A typical measurement result with the IRLED as the light source is shown in Fig.3.4. If the width of the light spot on the position–sensing unit is 10 % of the total measurement range, the maximum error caused by the nonuniform illumination calculated with Eq.(3.5) is smaller than 0.01 %. The sinusoidal variation in the photocurrent is actually caused by a concentric error between the center of the cylindrical hole of the vial and the center of the circular track of the photodiode, so that the light density variation in the radial direction is reflected in the angular direction.

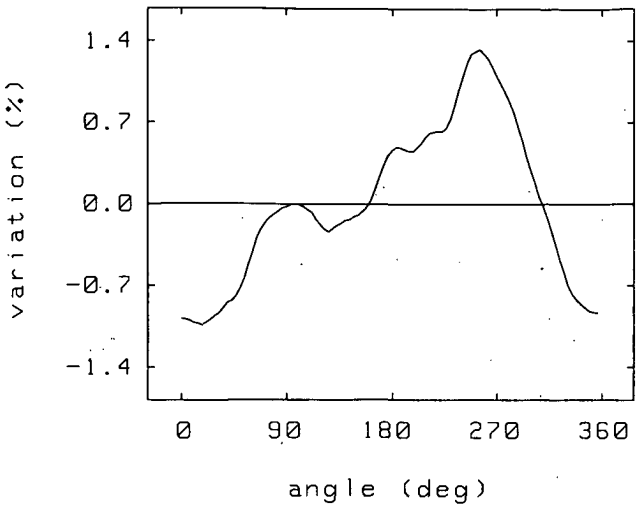

Fig.3.4 *Measured photocurrent variation along a circular track around the center of the light source (an IRLED). Radius of the circular track: 4 mm, distance between the light source and the center of the track: 20 mm.*

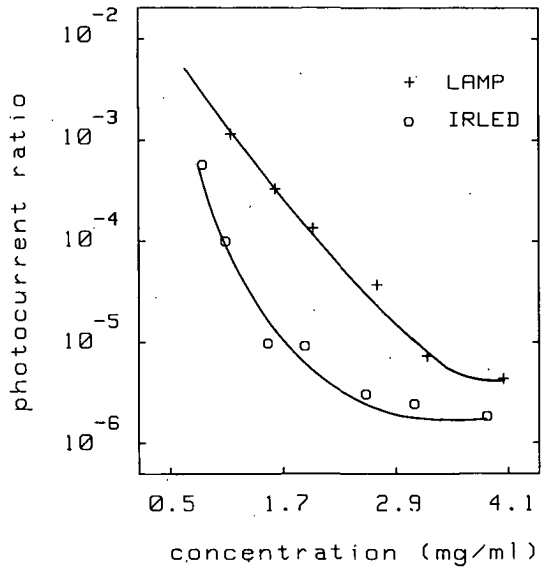

Fig.3.5 *Ratios between the photocurrents measured by the position–sensing unit with and without the dyed liquid as a function of the dye concentration c_d. The light sources are an IRLED and an incandescent lamp. Methasol Nigrosine is used as the dye. The thickness of the vial is 5 mm.*

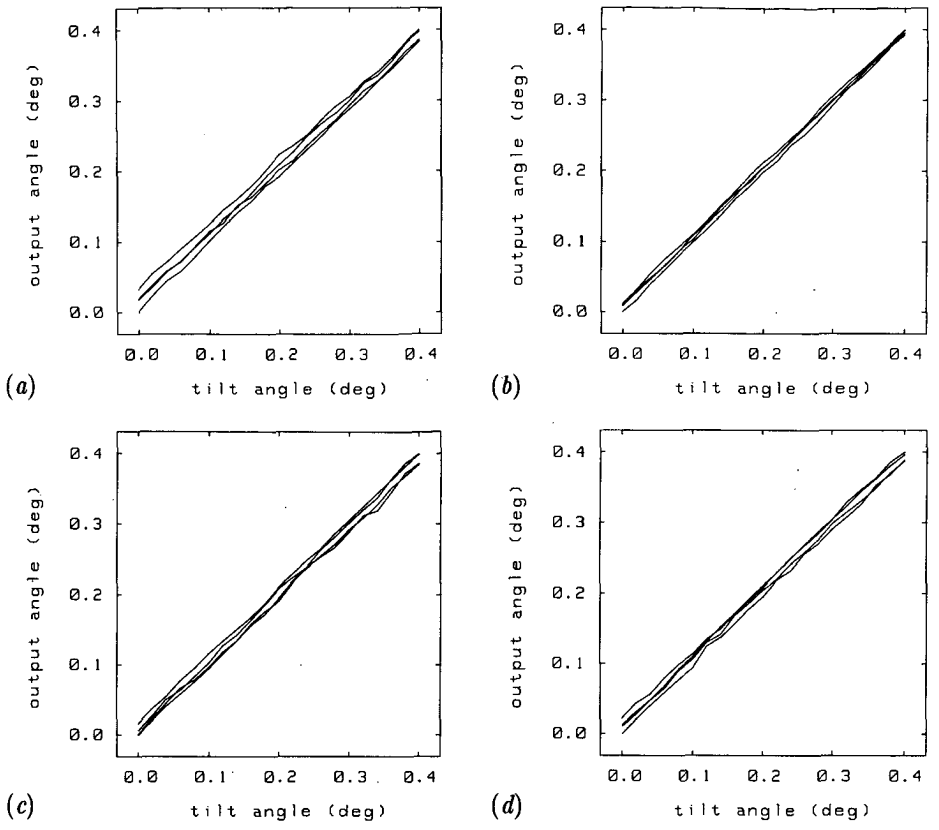

Fig.3.6 *Input–output characteristics measured with different dye (Methasol Nigrosine) concentrations: (a) $c_d = 1.1$ mg/ml, (b) $c_d = 1.4$ mg/ml, (c) $c_d = 2.1$ mg/ml, and (d) $c_d = 3.3$ mg/ml. The incandescent lamp is used as the light source.*

The ratios between the total photocurrents generated in the position–sensing unit with and without the dyed liquid as functions of the concentration of dye for both the IRLED and the incandescent lamp are shown in Fig.3.5. In the measurement the vial filled with the dyed alcohol is placed between the position–sensing unit and the light source. From Fig.3.5 we can see that the curves are flattened at high concentrations of the dye. This deviation from the Lambert–Beer's law is the result of the leakage current in the position–sensing unit. From Fig.3.5 we also can see that the photocurrent ratio for the IRLED at the dye concentration $c_d = 2$ mg/ml is much smaller than that for the incandescent lamp. This is apparently due to the fact that the lamp has a much wider spectrum than the IRLED.

By adding the dye to alcohol, the physical properties of alcohol may have been changed. In order to examine the influence of the dye on the motion behavior of the air bubble, measurements are carried out for four different dye concentrations. During the measurement the vial is rotated with a small angle of 0.4 degrees forwards and backwards twice. The angular position of the geometric center of the air bubble is measured. From Fig.3.6 we can see that the dye concentration has a minor influence on the motion behavior of the air bubble.

In order to investigate the stability of the dyed liquid, the solution of Methasol Nigrosine in alcohol (2 mg/ml) is centrifugalized in a centrifuge for 10 minutes with a speed of 20,000 circles per minute. No distinguishable depositions of the dye can be observed. Before the centrifuge the solution is filtered with a filter.

3.4 THE DYNAMIC RESPONSE

For systems which can be described by linear differential equations, transfer functions which relate the input signals to the output signals in the frequency domain can be established. The dynamic response then can be evaluated with the conventional techniques such as the frequency and the transient response analysis. A tilt sensor based on the spirit level principle is basically a nonlinear system, mainly due to the fact that the mass in motion is a liquid so that the shape of the air bubble is not a constant factor in most dynamic circumstances. However, the problem can be simplified when proper assumptions are made.

The most important assumption made in this analysis is that the liquid mass in motion can be considered as a rigid body, and that the air bubble conserves its shape even in a dynamic state. Thus the characteristic quantities associated with a rigid body, such as the moment of inertia and the center of mass, can be defined for the liquid mass. These quantities can then be used to establish differential equations describing the motion behavior of the air bubble. This assumption is contrary to the definition of liquid, as all the component particles in a liquid should enjoy the advantage of moving freely with respect to each other, whereas in a rigid body the distances between these particles always remain constant. However, from the theory of fluid mechanics we know that, in case of a flow of a real fluid in touch with a solid

surface, a thin transition region, which is called the boundary layer, in the fluid at the interface between the fluid and the solid surface can be distinguished [3.14]. The velocity of the fluid within this region changes rapidly from zero at the interface to approximately the velocity of the main flow. The thickness of this transition region can be very small, especially when the fluid has a low viscosity. This fact implies that for the particles in the main flow of the fluid the same velocity holds for each particle, and that the distances between them must be constant. Therefore, when certain conditions are satisfied, a moment of inertia and a center of mass can still be defined for the liquid mass in the main region. One of the conditions is that the mechanical input signals applied to the tilt sensor should be small.

3.4.1 The transfer function, the frequency and the transient response

the differential equations and the transfer functions

In a dynamic state the air bubble within the vial moves under the application of various physical forces. The first is the gravitational force of the earth which is the major acceleration force tending to keep the bubble in a position at the top of the spherical cavity of the vial. Secondly, there is a frictional force at the interface between the solid wall and the liquid when the liquid mass is in motion. It is the result of the viscous behavior of the liquid. This frictional force acts as a counter–acting force to the relative movement of the liquid with respect to the vial. Further, there is an inertial force when the vial is accelerated. The horizontal component of the inertial force causes the liquid inside the vial to pile up on the side away from the direction of acceleration and consequently pushes the bubble to move in the direction of acceleration.

For a tilt input the following differential equation can be obtained by balancing the gravitational force, the inertial force and the frictional force at the interface between the liquid and the vial:

$$(3.9)\quad J_m \frac{d^2}{dt^2}\theta_{out} + D\frac{d}{dt}\theta_{out} + mgR_{cm}\,\theta_{out} = J_m \frac{d^2}{dt^2}\theta_{in} + mgR_{cm}\,\theta_{in}$$

in which θ_{in} and θ_{out} are the input and output angles, respectively, D a constant parameter, m the liquid mass, R_{cm} the distance between the geometric center of the vial and the center of mass of the liquid, and J_m the moment of inertia of the liquid mass. It is further assumed that the boundary layer is very thin so that the liquid mass within it is negligible, and that the amplitude of the input signal is small.

The transfer function for a small tilt input signal is obtained by applying the Laplace transformation with the initial conditions that the input and output signals and their first–order derivatives are zero at the time $t = 0$. The transfer function for a tilt input is:

$$(3.10) \qquad F_t(s) = \frac{\theta_{out}}{\theta_{in}} = \frac{s^2/\omega_n^2 + 1}{s^2/\omega_n^2 + 2\zeta s/\omega_n + 1}$$

where s is the Laplace variable, ω_n the natural angular velocity, and ζ the damping ratio. The natural angular velocity ω_n and the damping ratio ζ are defined as:

$$(3.11) \qquad \omega_n = \sqrt{\frac{mgR_{cm}}{J_m}} \qquad \text{and} \qquad \zeta = \frac{D}{2\sqrt{mgJ_mR_{cm}}}$$

The differential equation of the system for a horizontal displacement input signal is derived by using the same assumptions:

$$(3.12) \qquad J_m \frac{d^2}{dt^2}\theta_{out} + D\frac{d}{dt}\theta_{out} + mgR_{cm}\,\theta_{out} = maR_{cm}$$

with $a = d^2x/dt^2$ and x the horizontal displacement. Applying the same approximations we obtain the transfer function for a horizontal displacement input:

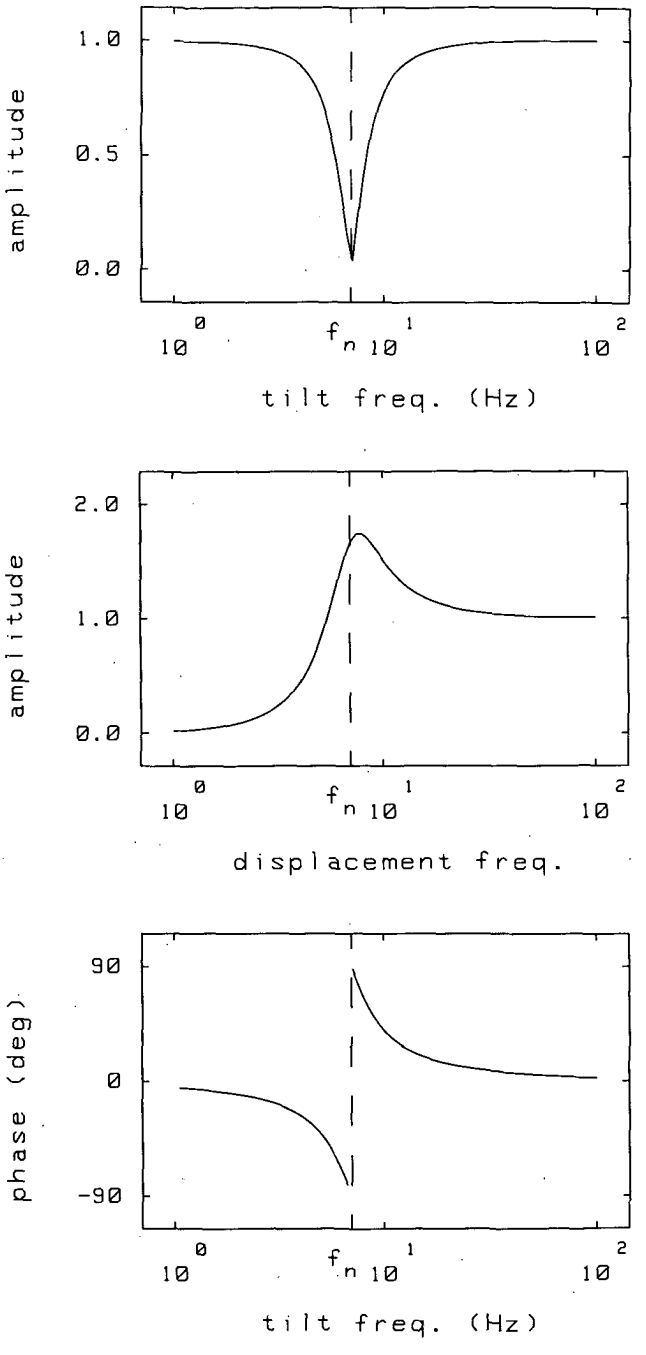

(*a*)

(*b*)

(*c*)

Fig.3.7 *Frequency responses of the tilt sensor: (a) the amplitude with a tilt input, (b) the amplitude with a horizontal displacement input, and (c) the phase shift.* $f_n = \omega_n/2\pi = 7Hz$, $\zeta = 0.2$.

$$(3.13) \qquad F_x(s) = \frac{\theta_{out}}{x} = \frac{1}{g} \frac{s^2}{s^2/\omega_n^2 + 2\zeta s/\omega_n + 1}$$

the frequency response

Figure 3.7 shows the calculated frequency responses of the tilt sensor. From Fig.3.7(a) we can see that, as the oscillation frequency approaches the natural frequency $f_n = \omega_n/2\pi$, the amplitude of the transfer function approaches zero. This is apparently due to the fact that around the natural frequency, the air bubble tends to move with the vial. This behavior of the bubble is caused by the viscous effect in the liquid which has the tendency to couple the rotational motion of the vial with the liquid mass. At tilt oscillation frequencies above f_n, the inertia of the liquid dominates and holds the bubble stationary with respect to the vial. At tilt oscillation frequencies below f_n, only the weight of the liquid acted upon by the gravitational force tends to keep the bubble at the top of the spherical cavity. The calculated frequency response to a horizontal displacement input is shown in Fig.3.7(b). Since an increasing oscillation frequency of the horizontal displacement with a constant amplitude means an increasing horizontal acceleration, the amplitude of the transfer function increases at frequencies below the natural frequency. At frequencies above the natural frequency, the liquid inertia dominates again, so that the response tends to be flat for higher frequencies. Figure 3.7(c) shows the phase shift of the output signal, from which we can see that the tilt sensor is a nonminimum phase system. As the tilt frequency passes the natural frequency, a phase shift of 180 degrees occurs.

the transient response to a step input

The transient responses of the tilt sensor to a step input of tilt and a step input of horizontal displacement, respectively, are derived from Eq.(3.10) and Eq.(3.13) as:

$$(3.14) \qquad c_{tilt}(t) = 1 - \frac{2\zeta}{\sqrt{1-\zeta^2}} exp(-\zeta\omega_n t) sin(\sqrt{1-\zeta^2}\,\omega_n t)$$

and

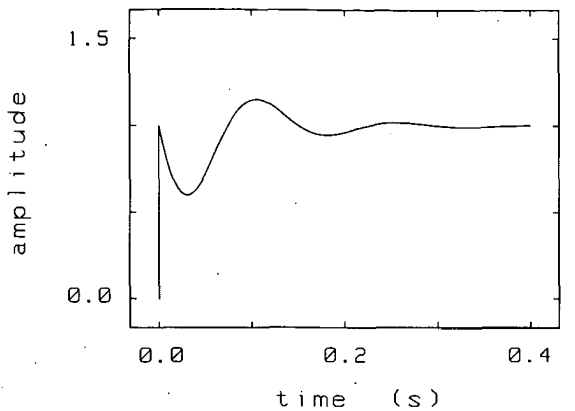

(*a*)

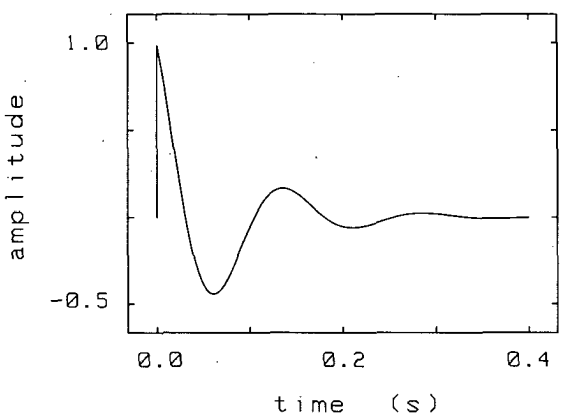

(*b*)

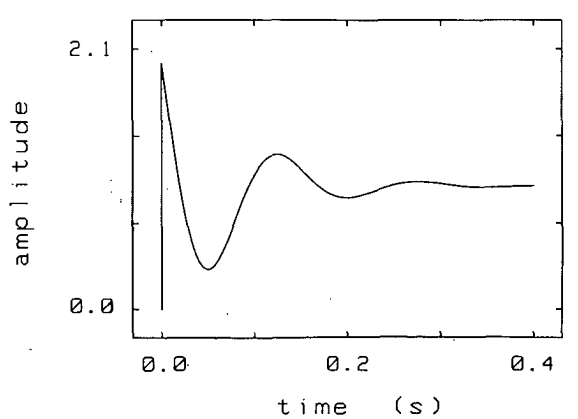

(*c*)

Fig.3.8 *Transient responses to step inputs of (a) tilt, (b) horizontal displacement, and (c) a superimposition of these two signals.* $f_n = \omega_n/2\pi = 7Hz$, $\zeta = 0.2$.

$$(3.15) \qquad c_{disp}(t) = -\frac{{\omega_n}^2}{g\sqrt{1-\zeta^2}}\, exp(-\zeta\omega_n t) sin(\sqrt{1-\zeta^2}\,\omega_n t - \theta_{ph})$$

where $\theta_{ph} = arctan(\sqrt{1-\zeta^2}/\zeta)$. The step response to a superimposed input signal of both tilt and horizontal displacement is obtained by adding Eq.(3.14) and Eq.(3.15), which gives:

$$(3.16) \qquad c(t) = 1 - \frac{1}{\sqrt{1-\zeta^2}}\, exp(-\zeta\omega_n t)$$
$$\times \left(2\zeta\, sin(\sqrt{1-\zeta^2}\,\omega_n t) + S_f \frac{{\omega_n}^2}{g}\, sin(\sqrt{1-\zeta^2}\,\omega_n t - \theta_{ph}) \right)$$

where S_f is a constant scaling factor. The calculated step responses from Eq.(3.14), Eq.(3.15) and Eq.(3.16) to a tilt, a horizontal displacement and a superimposition of these two signals are shown in Fig.3.8.

3.4.2 Estimation of the natural frequency and the damping ratio

shape of the air bubble

The dynamic behavior of the air bubble depends on its shape, which is determined by the size of the cylindrical hole and the amount of the liquid in the vial, and by the mass density, the surface tension and the contact angle of the liquid. Since the form of the vial and the physical properties of the liquid are given factors, the shape of the air bubble can only be changed by varying the amount of liquid in the vial. The calculation is carried out with the assumption that the dimension of the cylindrical hole in the vial in the axial direction is infinitely large, so that a two–dimensional model established in the plane perpendicular to the axis of the cylindrical hole can be used. The effects of the side walls of the vial on the bubble motion are not taken into account.

Consider a portion of the liquid–air interface bounded by two planes parallel to the x–y plane at a unit distance apart. By equalizing the components of forces acting on

the interface on the x–axis, the following equation can be obtained in the absence of inertial acceleration [3.15]:

$$\gamma_{LV}\cos\theta + \frac{1}{2}\rho g y^2 = C \tag{3.17}$$

where ρ is the density of the liquid, θ the tangential angle of the liquid–air interface at the position (x, y) with respect to the x–axis, and C is a constant. The liquid–air interface can be described by the coordinates (x, y) with:

$$x = \int_0^{\theta} \frac{kbcos\theta'}{2(1 - k^2cos^2\theta'/2)^{1/2}}\, d\theta' \tag{3.18}$$

$$y = \frac{2b}{k}\sqrt{1 - k^2cos^2\theta/2} \tag{3.19}$$

in which θ' is an integral parameter, g the gravitational acceleration, $b^2 = \gamma_{LV}/\rho g$ and $k^2 = 4b^2/(C + 2b^2)$. Referring to Fig.3.9 the parameter k, the coordinates (x_1, y_1) and the coordinate of the center of the hole y_0 can be determined if one of the following values is known: the volume of the liquid, the angle θ_1, the coordinates y_0, x_1 or y_1. For the calculation the easiest way is to assume that θ_1 is known. The rest of the parameters can then be obtained by solving the equations:

$$x_1 = Rsin\theta_1 \qquad x_1 = \int_0^{\theta_1} \frac{kbcos\theta}{2(1 - k^2cos^2\theta/2)^{1/2}}\, d\theta \tag{3.20}$$

$$x_1^2 + (y_1 - y_0)^2 = R^2 \qquad y_1 = \frac{2b}{k}\sqrt{1 - k^2cos^2\theta_1/2}$$

in which the coordinates x_1, y_1, y_0 and the parameter k are the unknowns.

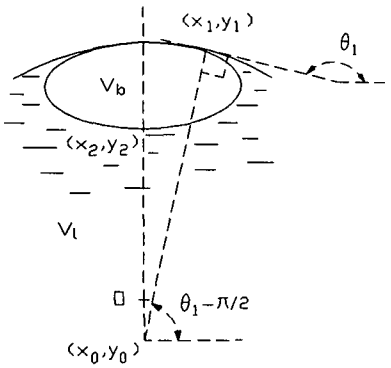

Fig.3.9
Sketch showing the parameters used in the calculation of the bubble shape.

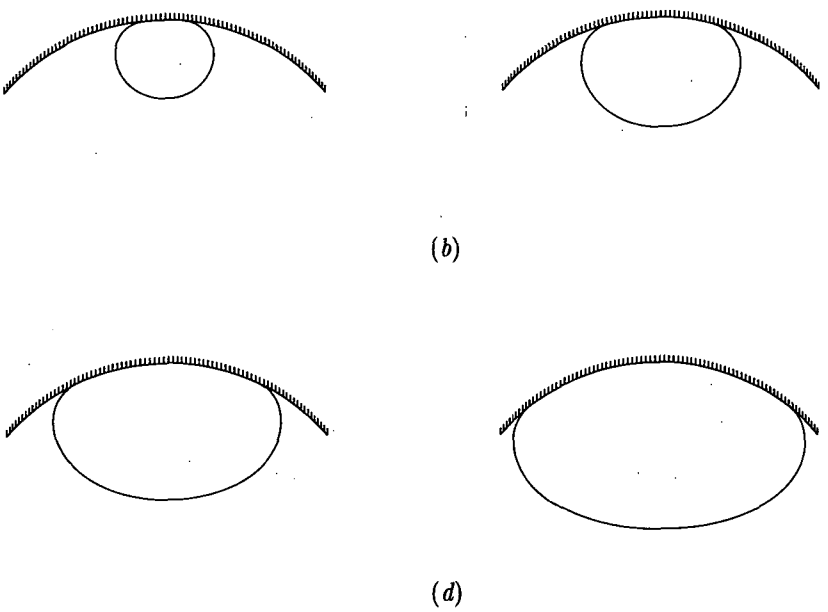

Fig.3.10 *Shapes of the air bubble with different sizes*: (*a*) $V_b/V_v = 4$ %, (*b*) $V_b/V_v = 10$ %, (*c*) $V_b/V_v = 17$ %, (*d*) $V_b/V_v = 27$ %. *The radius of curvature of the vial is* 5 *mm.*

The volume of the liquid can be readily calculated with $V_l = V_v - V_b$, where V_v is the volume of the vial, V_l that of the liquid, and V_b that of the air bubble with:

$$(3.21) \qquad V_b = 2(\pi - \theta_1)dR^2 + \frac{1}{2}\, dR^2 sin2\theta_1 + \int_0^{\theta_1} \frac{dkbcos\theta}{(1 - k^2cos^2\theta/2)^{1/2}}\, x(\theta)\, d\theta$$

where d is the thickness and R the radius of curvature of the vial.

The calculated shapes of the air bubble are depicted in Fig.3.10. The size of the bubble is used as a parameter, which is expressed as the relative volume of the bubble to the vial. From Fig.3.10 we can see that, for an air bubble with a small size, its shape approaches a circle. As the size increases the shape becomes more like an ellipse. These calculated results agree well with experimental observations.

the parameter D

The parameter D included in Eq.(3.11) is derived from the torque exerted on the liquid body. D depends on the mass density and the viscosity of the liquid, the shape of the air bubble, and, by approximation, it is independent on the frequency of an input signal. When the vial changes its tilt position, the working liquid inside the vial will flow with respect to the vial. The frictional force per unit area or the shear stress τ defined parallel to the flow direction and the solid surface is given by Newton's law of friction:

$$(3.22) \qquad \tau = \mu \frac{du}{dy}$$

in which μ is the viscosity and u the velocity of the fluid parallel to the solid surface. y is measured outwards from the solid surface. It is further assumed that the angular velocity is not too high, so that it is only necessary to take the gravitational force and the frictional force into account. By balancing the shear force and the gravitational force in a small volume at the solid surface, the boundary layer thickness is derived as [3.16]:

$$\delta \approx \sqrt{\frac{\mu r \omega}{\rho g}} \tag{3.23}$$

where $0 < r < R$, ω is the angular velocity of the liquid relative to the vial and δ the thickness of the boundary layer. Using the values given in Table 3.1, we obtain the boundary layer thickness: $\delta = 0.3$ mm for alcohol with $\omega = 120$ cps and $r = 5$ mm. The shear stress is obtained:

$$\tau \approx \mu \frac{r\omega}{\delta} \approx C_s \sqrt{g\mu\rho r}\, \omega \tag{3.24}$$

where an approximation is made by replacing the square root of ω by $C_s\omega$ with C_s a constant. The torque T can be calculated by multiplying Eq.(3.24) with r and integrating the obtained equation over the entire inner surface S_c of the vial which is in contact with the liquid. Using the relation: $T = D\omega$, with $\omega = d\theta_{out}/dt$, the parameter D is obtained:

$$D = C_s \sqrt{g\mu\rho} \iint_{S_c} r^{3/2}\, dS \tag{3.25}$$

estimation of ω_n *and* ζ

When the shape of the air bubble is known, the center of mass and the moment of inertia of the working liquid for a given size of the air bubble are obtained:

$$R_{cm} = \frac{1}{V_1} \iiint_{V_1} (y - y_0)\, dV \tag{3.26}$$

and

$$J_m = \iiint_{V_1} \rho \left[x^2 + (y - y_0)^2\right] dV \tag{3.27}$$

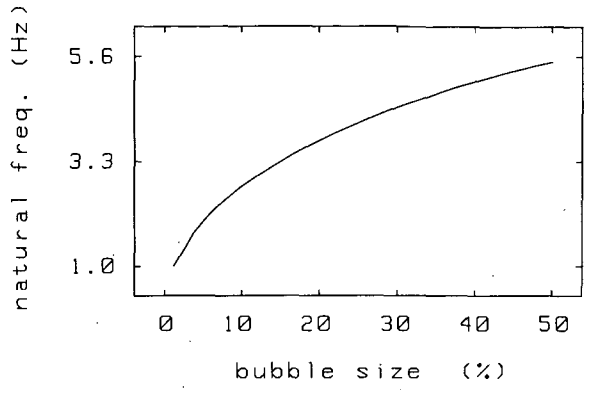

(*a*)

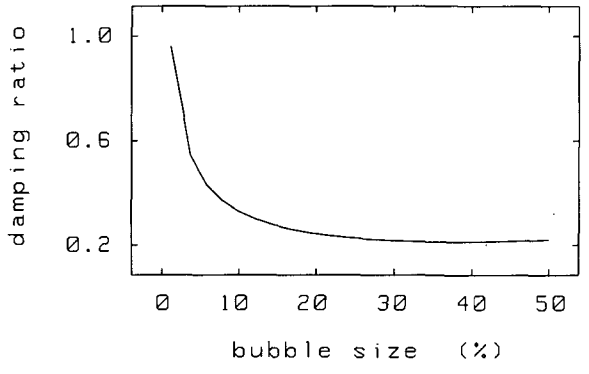

(*b*)

Fig.3.11 *Calculated results of (a) the change of the natural frequency f_n and (b) the relative change of the damping ratio ζ as functions of the bubble size.*

Equations (3.26) and (3.27) are solved numerically. Figure 3.11 shows the calculated values of f_n and ζ as functions of the bubble size. As Fig.3.11(a) shows that the natural frequency f_n increases with the bubble size. The relative change of the damping ratio ζ is calculated. Figure 3.11(b) shows that ζ decreases with the bubble size.

It is interesting to see the influence of the viscosity and the mass density of the working liquid on the dynamic behavior of the tilt sensor, if we make a comparison between alcohol, water and mercury. From Eq.(3.11) we can see that the natural

frequency is not dependent on the mass density and the viscosity, but the damping ratio is. The damping ratio can be evaluated by rewriting Eq.(3.11) as: $\zeta \approx \mu/\rho\, f(V_{\text{liquid}}, \theta_c, b)$, in which $f(V_{\text{liquid}}, \theta_c, b)$ is a function dependent on the shape of the air bubble. It is determined when the volume of the liquid V_{liquid}, the contact angle θ_c and the parameter b are given. When the contact angles of the liquids are assumed to be zero, the calculated values of $f(V_{\text{liquid}}, \theta_c, b)$ for mercury, water and alcohol are approximately the same. From this relation we can see that the damping ratio increases with the viscosity and decreases with the mass density. This is because the viscous force tends to drag the liquid mass with the vial in response to any movement of the vial, whereas a working liquid with a large mass has a large inertial momentum and tends to move freely inside the vial ignoring the movement of the vial. The numerically calculated damping ratios for mercury and water relative to alcohol are: $\zeta_{\text{mercury}} = 0.059\ \zeta_{\text{alcohol}}$, and $\zeta_{\text{water}} = 0.71\ \zeta_{\text{alcohol}}$, respectively. Therefore, for tilt sensors with alcohol as the working liquid, a larger damping effect can be achieved than with mercury or water.

3.4.3 Experimental results

Experiments are carried out with respect to the following aspects:

- the validity of the rigid body assumption,
- the frequency response of the tilt sensor,
- the transient response to a step input.

Finally, the influence of the size of the air bubble on the natural frequency and the the damping ratio is also experimentally investigated.

The validity of the rigid body assumption and the approximations, which are made during the derivation of the linear differential equations, can be examined by applying a sinusoidal input signal with a variable frequency and a constant amplitude to the tilt sensor. In the measurement the amplitude of the sinusoidal tilt input is 1.15 degrees. A typical output response of the sensor is presented in Fig.3.12(a), which shows a well–defined sinusoidal wave form. The input oscillation frequency $f_{\text{in}} = 28$ Hz. The spectrum of the output signal is also inspected by means of a spectrum analyzer for different input frequencies. The experimental results are shown in Fig.3.13. A slight increase in the amplitudes of the second and third harmonics of the input frequency can be observed for the input frequency $f_{\text{in}} = 55$ Hz. This is probably a result of the increasing vibration of the experimental setup at higher frequencies.

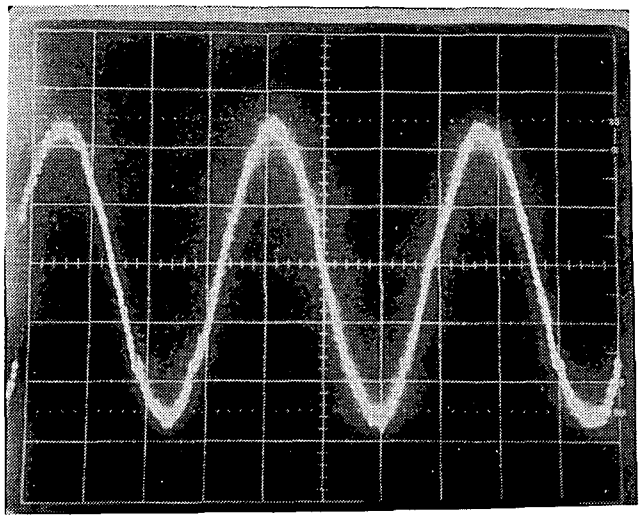

(*a*)

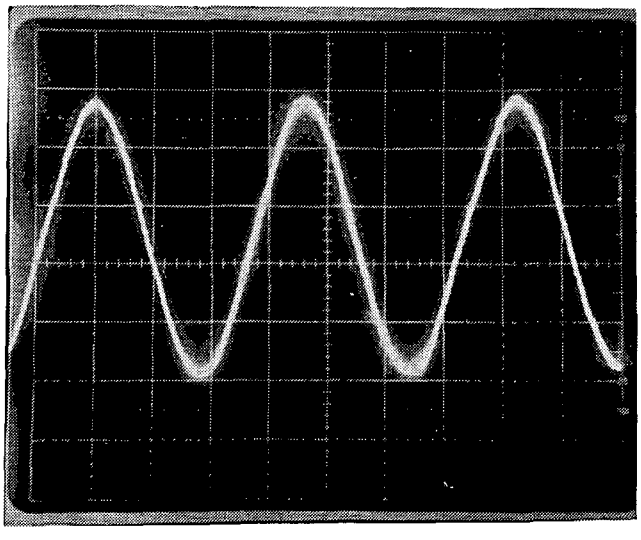

(*b*)

Fig.3.12 *Responses of the tilt sensor to (a) a sinusoidal tilt input signal, x–axis: 10 ms/div., f_{in} = 28 Hz, and (b) a sinusoidal horizontal displacement input signal, x–axis: 20 ms/div, f_{in} = 14 Hz.*

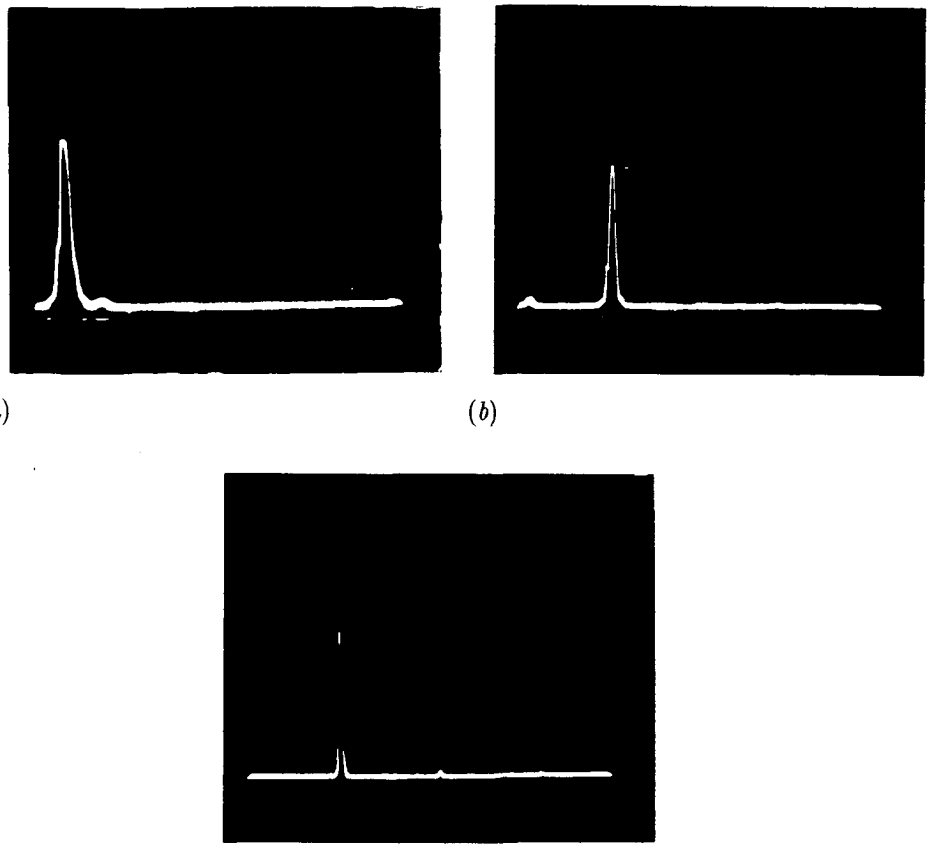

(*a*) (*b*)

(*c*)

Fig.3.13 *Spectra of the sensor responses for different input frequencies* f_{in}. (*a*) *x–axis full–scale*: 50 *Hz*, $f_{in} = 4.5$ *Hz*, (*b*) *x–axis full–scale*: 100 *Hz*, $f_{in} = 25$ *Hz*, (*c*) *x–axis full–scale*: 200 *Hz*, $f_{in} = 55$ *Hz*.

The amplitude of the sinusoidal horizontal displacement input is 0.5 mm. The sensor response for $f_{in} = 14$ Hz is presented in Fig.3.12(b), which shows again a well–defined sinusoidal wave form. The rigid body assumption is only valid for low horizontal displacement input frequencies. As the frequency is further increased, the air bubble is soon broken and the liquid rushes into the space which is occupied by the air. This causes abrupt changes in the output signal. Since the horizontal acceleration increases quadratically with the oscillation frequency, the wave form of the output signal becomes totally irregular for oscillation frequencies higher than 19 Hz.

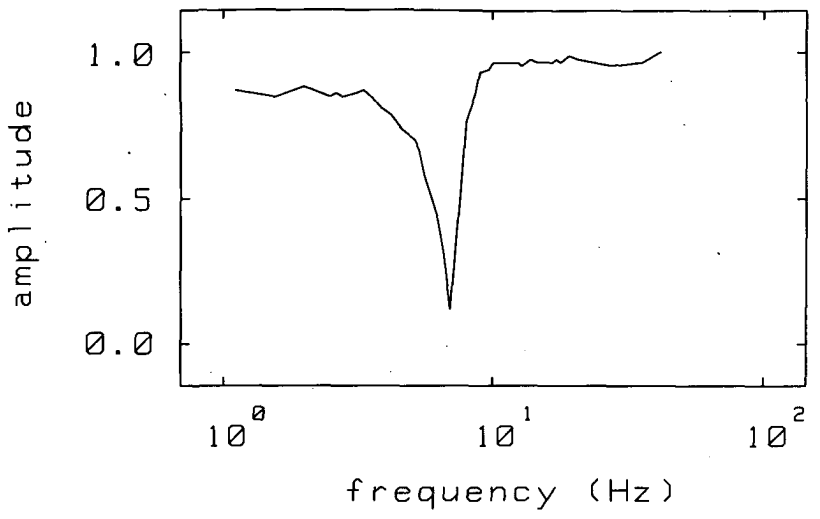

(*a*)

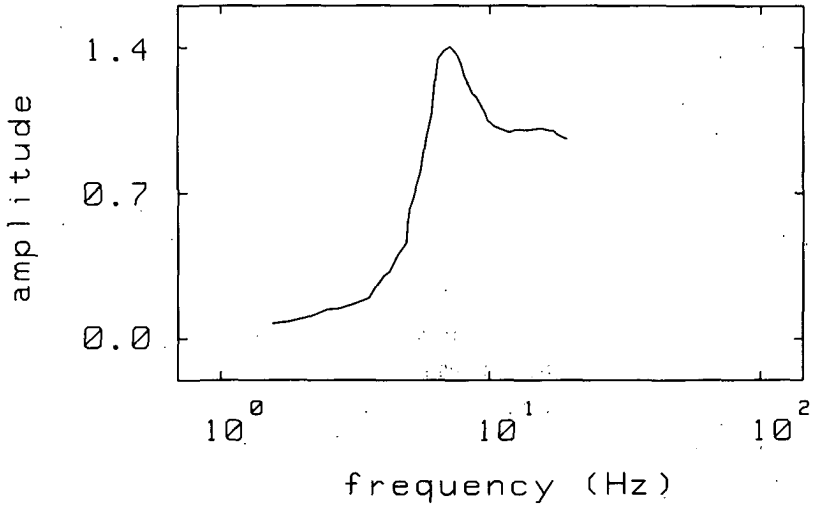

(*b*)

Fig.3.14 *Measured frequency responses of the tilt sensor to (a) a tilt input and (b) a horizontal displacement input. The measured minimum in (a) occurs at the frequency* $f_{\text{in}} = 6.8$ *Hz.*

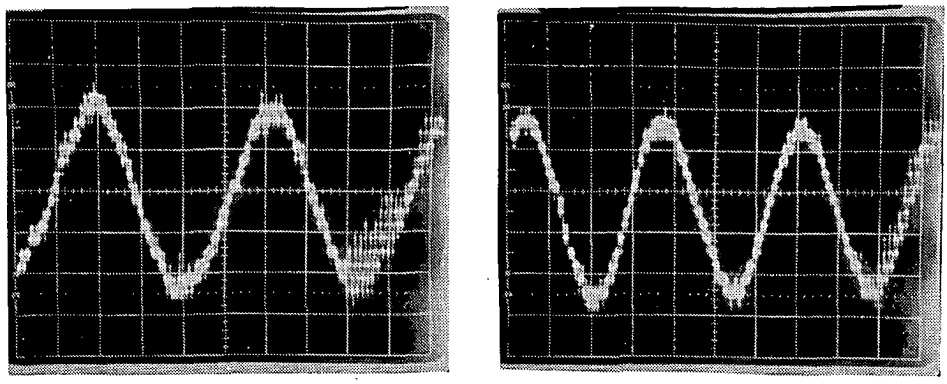

(*a*) (*b*)

Fig.3.15 *Phase shift in the sensor response around the natural frequency.* (*a*) $f_{in} = 6.0$ *Hz, and* (*b*) $f_{in} = 7.1$ *Hz. x–axis:* 40 *ms/div.*

The frequency responses of the tilt sensor to a tilt and a horizontal displacement input are shown in Fig.3.14. The measured amplitude of the output signal in Fig.3.14(a) has a minimum at the frequency $f_{in} = 6.8$ Hz, which shows a reasonable agreement with the calculated result. That the tilt sensor is a nonminimum phase system can be seen from Fig.3.15, in which the output signal is measured at two frequencies around the natural frequency. The measured phase shift within that frequency range is about 150 degrees.

The measured transient responses to step inputs of tilt and horizontal displacement are shown in Fig.3.16. Comparing Fig.3.16 with Fig.3.8, several things can be noted. First, there is the overshoot in the step response to a tilt input, which is much larger than the calculated one. This may be caused by a concentric error between the center of the tilt sensor and the center around which the device rotates. During the measurement when a step input of tilt is applied, the tilt sensor may undergo simultaneously a movement in the horizontal direction. The result is that the step response to a tilt is superimposed by a step response to a horizontal displacement. Therefore, the overshoot in this case is larger. Secondly, the step responses to both the tilt and the horizontal displacement input exhibit an abrupt change in the signal level at the beginning of the response. The response curves in both cases do not go as smoothly as predicted by Eq.(3.14) and Eq.(3.15). From Fig.3.16 we can see that the first minima in the measured responses are not the same as those shown in Fig.3.8. This can be explained again by the occurrence of a broken air bubble. Since in this

case, although the horizontal displacement may be very small, due to the position change within a short time interval the associated horizontal acceleration can be very large. From Fig.3.16 it is also interesting to see that the air bubble has a good ability to recover its shape within a very short time interval after the abrupt disturbance disappears. The time interval in which the air bubble remains broken is much shorter than the time period with which the bubble oscillates around the new position. Therefore, we may conclude that, although the air bubble can easily be broken when accelerated, the motion behavior of the air bubble can still be described by the second–order linear differential equations after the acceleration vanishes. Also the damping effect in the tilt sensor can still be predicted by using the rigid body assumption with a good degree of accuracy.

The influence of the bubble size on the natural frequency and the damping ratio is also experimentally investigated. The natural frequency of the tilt sensor can be determined by measuring the frequency response. As shown in Fig.3.17, the minimum in the response occurs at the frequency f_n. The frequency f_n slightly increases with the bubble size. The natural frequency is approximately 7 Hz. The damping ratio can be obtained by measuring the transient response. The measurement results for various bubble sizes are shown in Fig.3.18. The damping ratio can be calculated as follows: the moments t_n on which maxima and minima occur in the step response are calculated by taking the first differentiation of Eq.(3.16) and making the equation equal to zero. We then obtain:

$$t_n = \frac{1}{\omega_n\sqrt{1-\zeta^2}}(\theta' + n\pi) \tag{3.28}$$

with $n = 0, 1, 2 \ldots$, and θ' a function of ζ and θ_{ph}. Inserting Eq.(3.28) into Eq.(3.16) we obtain the maxima and minima in the step response:

$$c(t_n) = 1 - \frac{1}{\sqrt{1-\zeta^2}} exp\left(-\frac{\zeta(\theta' + n\pi)}{\sqrt{1-\zeta^2}}\right) \times \left(2\zeta\, sin(\theta' + n\pi) + S_c \frac{\omega_n^2}{g} sin(\theta' - \theta_{ph} + n\pi)\right) \tag{3.29}$$

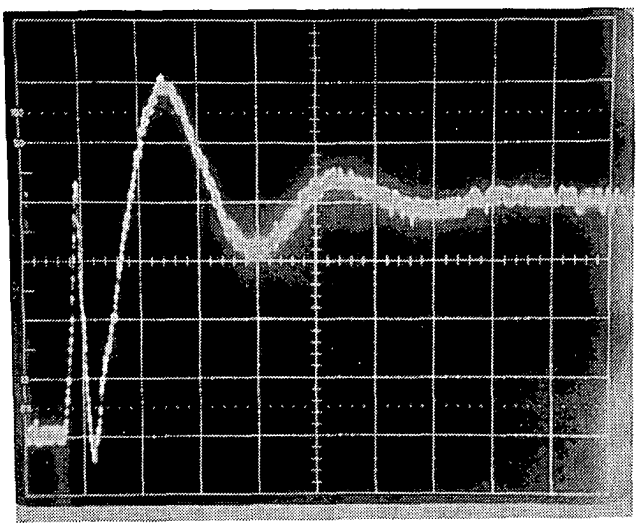

(*a*)

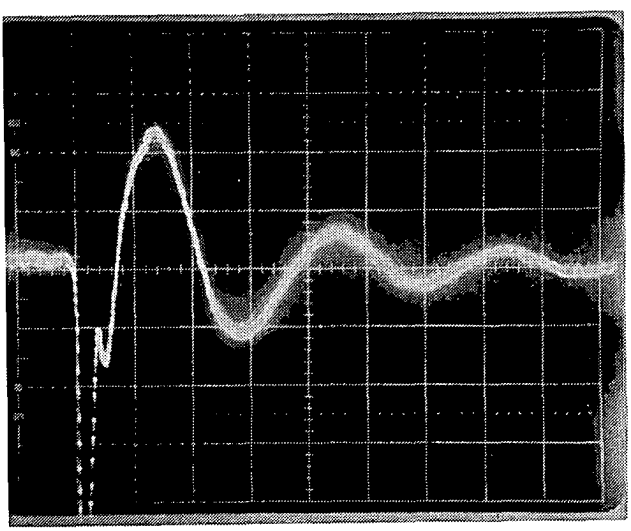

(*b*)

Fig.3.16 *Measured transient responses to step inputs of* (*a*) *tilt and* (*b*) *horizontal displacement. x–axis*: 50 *ms/div.*

The first maximum $c(t_1)$ and the second minimum $c(t_2)$ are measured. By defining a factor: $R_m = |(c(t_1) - 1)/(c(t_2) - 1)|$, it can be shown that:

$$\zeta = \sqrt{\frac{ln^2 R_m}{ln^2 R_m + \pi^2}} \tag{3.30}$$

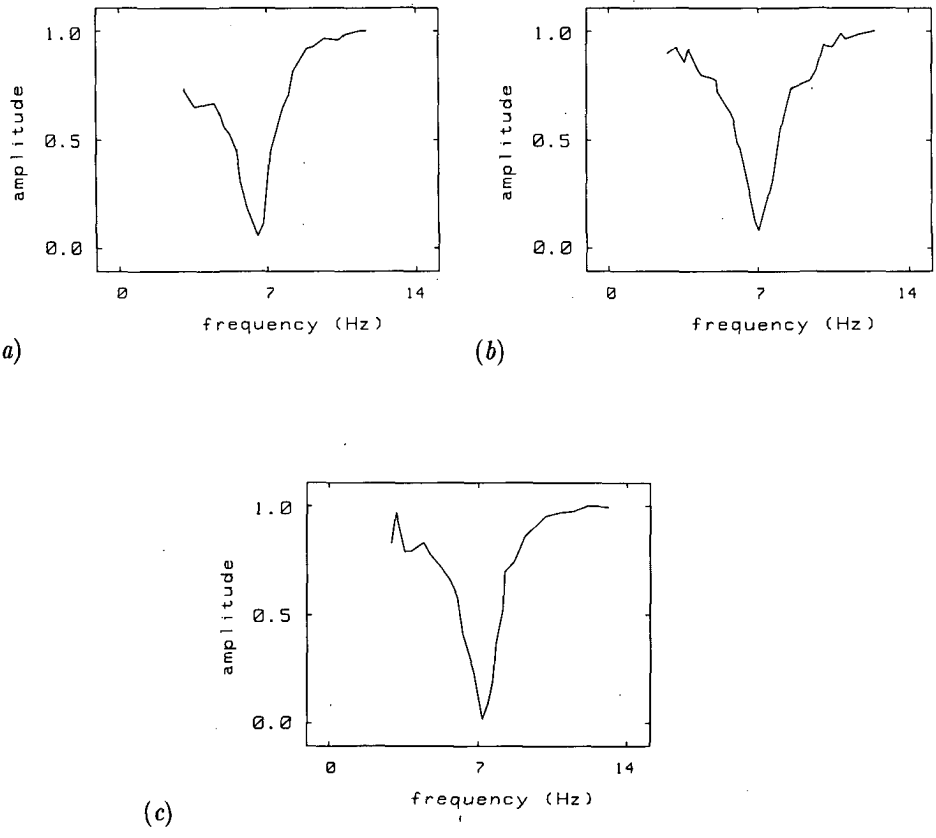

Fig.3.17 *Measured frequency responses of the sensor with bubble sizes of* (*a*) $V_b/V_v = 13$ %, $f_n = 6.8$ *Hz*, (*b*) $V_b/V_v = 19$ %, $f_n = 7.0$ *Hz*, *and* (*c*) $V_b/V_v = 25$ %, $f_n = 7.2$ *Hz*.

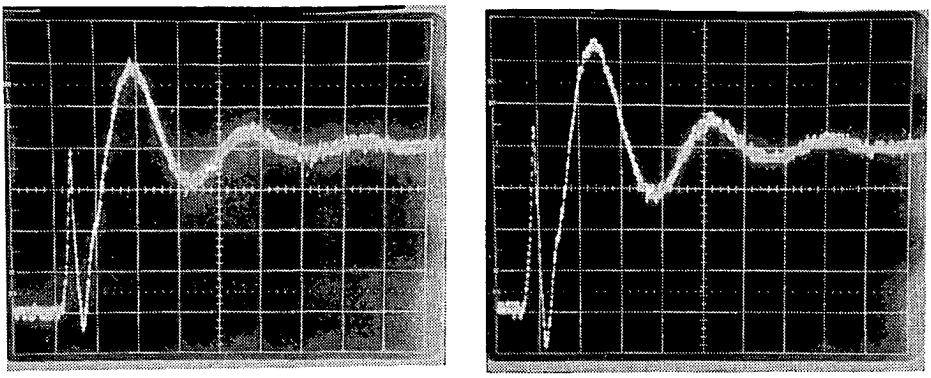

(*a*) (*b*)

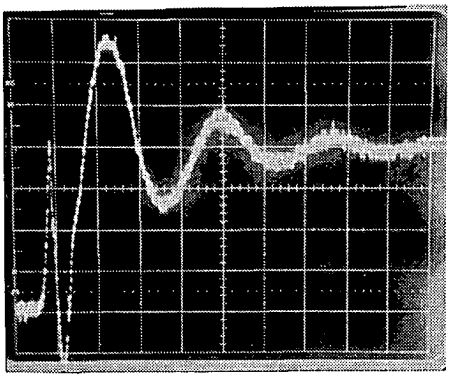

(*c*)

Fig.3.18 *Measured transient responses of the sensor with bubble sizes of:* (*a*) $V_b/V_v = 13\ \%$, $\zeta = 0.23$, (*b*) $V_b/V_v = 19\ \%$, $\zeta = 0.22$, *and* (*c*) $V_b/V_v = 25\ \%$, $\zeta = 0.20$. *x–axis*: 50 *ms/div.*

The damping ratio lies in the order of 0.2 and decreases with the bubble size. From Fig.3.18 we can see that the sharp minimum in the step response increases with the bubble size. This may be because large bubbles are relatively easier to break than small bubbles. The settling time T_s for a second–order system is defined as [3.17]: $T_s = 4/\omega_n\zeta$. $T_s = 0.45$ s for $f_n = 7$ Hz and $\zeta = 0.2$.

3.5 CONCLUSIONS

The selection criterion for the working liquid is based on its physical properties. Liquids which have a large contact angle with the vial are considered as not suitable for the application to a tilt sensor. For liquids with a small or zero contact angle it is preferable to use liquids which have a small surface–tension–to–mass–density ratio. Comparisons between mercury, water and alcohol have made it clear that alcohol possesses many favorable properties for our application. The treatment of the vial surface is also of great importance as roughness of the solid surface will increase the contact angle and the contact angle hysteresis.

Compared with an incandescent lamp the IRLED has the virtues of high light emitting efficiency, a narrow light distribution spectrum and less heat generation. A disadvantage of the IRLED is its price, which is relatively high. The illumination of the vial by the light source is generally not uniform. But when the center of the light source coincides with that of the vial, the light density variation along the track of the air bubble is minimized. The influence of the light density variation on the sensor accuracy can further be reduced when a position–sensing unit is used which measures the center of gravity of an incident light spot. Methasol Nigrosine is considered as a suitable dye because of its wide absorption spectrum and high absorption coefficient. The concentration of the dye must be higher than 2 mg/ml for a vial with a thickness of 5 mm.

By using the rigid body assumption and the small signal analysis second–order, linear differential equations are established for the description of the dynamic response of the tilt sensor. Transfer functions are obtained for both tilt and horizontal displacement inputs. The tilt sensor exhibits an inherently well–damped dynamic response with a natural frequency of 7 Hz and a damping ratio of 0.2. The natural frequency and the damping ratio included in the transfer functions are dependent on the shape of the air bubble, which in turn depends on the amount of the working liquid in the vial. Experiments show that, although during turbulent disturbances the air bubble can easily be broken, it possesses the capability of recovering its shape within a very short time interval after the disturbances disappear. This time interval is much shorter than the time in which the bubble oscillates within the vial. Therefore, the simplified model can still be used in the estimation of the settling time of the tilt sensor, which is actually the primary goal of the dynamic response analysis.

References

[3.1] E. Wolfram and R. Faust, "Liquid drops on a tilted plate, contact angle hysteresis and the Young contact angle", in "Contact angle, wettability, and adhesion", editor R. F. Gould, American Chemical Society, Washington, D. C., pp.213–222, 1964.

[3.2] R. H. Dettre and R. E. Johnson, jr., "Contact angle hysteresis, II. Contact angle measurements on rough surfaces", in "Contact angle, wettability, and adhesion", editor R. F. Gould, American Chemical Society, Washington, D.C., pp.136–144, 1964.

[3.3] H. Lomas, "Calculation of advancing and receding contact angles, I. drops on inclined planes", J. Coll. and Interface Sci., Vol.33, pp.548–553, 1970.

[3.4] C. G. L. Furmidge, "Studies at phase interfaces; I. The sliding of liquid drops on solid surfaces and a theory for spray retention", J. Coll. Sci., Vol.17, pp.309–324, 1962.

[3.5] N. J. Kreidl, "Glass surfaces then and now", J. Non–Crystalline Solids, Vol.49, pp.331–338, 1982.

[3.6] G. Navascues, "Liquid surfaces: theory of surface tension", Rep. Prog. Phys., Vol.42, pp.1131–1185, 1979.

[3.7] R. C. Weast, editor, "Handbook of chemistry and physics", 52nd edition, The Chemical Rubber Company, Ohio, 1971.

[3.8] G. Macdougall and C. Ockrent, "Surface energy relations in liquid/solid systems; I. The adhesion of liquids to solids and a new method of determining the surface tension of liquids", Proc. Roy. Soc., Vol.180, pp.151–172, 1942.

[3.9] D. Talmud and N. M. Lubman, "Neue (Mikro–)Methode zur Messung der Randwinkel", Z. Physik. Chem., Vol.148A, pp.227–232, 1930.

[3.10] H. K. Livingston, "Contact angles and adsorption on solid surfaces", J. Phys. Chem., Vol.48, pp.120–124, 1944.

[3.11] G. R. Elion and H. A. Elion, "Electro–optics handbook", Marcel Dekker, Inc., New York, 1979.

[3.12] T. Vickersaff, "The physical chemistry of dyeing", Oliver and Boyd, London, 1950.

[3.13] E. N. Abrahart, "Dyes and their intermediates", Edward Arrold Ltd., London, 1977.

[3.14] B. S. Massey, "Mechanics of fluids", 4th edition, Van Nostrand Reinhold Ltd., New York, 1979.

[3.15] H. Lamb, "Statics", Cambridge University Press, Cambridge, 1924.

[3.16] H. Schlichting, "Boundary layer theory", Pergamon Press Ltd., London, 1955.

[3.17] R. C. Dorf, "Modern control systems", Addison–Wesley Publishing Company, London, 1980.

CHAPTER 4 THE POSITION–SENSING UNIT

4.1 INTRODUCTION

In recent years, as a result of the rapid development of silicon planar IC–technology, numerous solid–state devices, such as photodiode arrays, charge–coupled devices, duo and quadrant detectors, and position–sensitive detectors, capable of measuring the position of an incident light beam became widely available. For application to the tilt sensor, the position–sensitive detectors (PSD's) utilizing the lateral photoeffect are considered as the most suitable. Their advantages over the other light spot position detectors are the high position–response linearity and the high position resolution. Photodiode arrays and charge–coupled devices have a limited resolution because these devices work with discrete photo–sensitive cells. Duo and quadrant detectors are not suitable for position measurement over large measurement ranges.

The principle of the position–sensitive detector as a semiconductor device has been known for a long time. After Wallmark's rediscovery in 1957 [4.1], considerable research was devoted to the lateral photoeffect, which is the elementary effect responsible for the operation of the PSD's. The basic differential equation which

describes the lateral photoeffect was presented by Lucovsky [4.2] in 1960. Allen [4.3] solved Lucovsky's equation for a circular PSD in which point electrodes were incorporated. Buzanova *et al.* [4.4] presented a formal solution of the Lucovsky's equation for a rectangular PSD with two extended electrodes. It was verified that rectangular PSD's with extended electrodes on opposite sides are capable of measuring the position of an incident light beam in a direction perpendicular to the electrodes with a good position–response linearity, independently of the light spot movement in the other direction. In due time it was also realized that PSD's offer better performances when they are operated in a reverse–biased condition [4.5]. Woltring [4.6] compared several PSD configurations and found that for the two–dimensional measurement the dual bilateral photodiode–type PSD was inherently linear. Silicon planar technology was used by Vassilov [4.7] for the purpose of fabricating a solar–cell type PSD. Noorlag and Middelhoek [4.8] used the standard IC process for the fabrication of a two–dimensional PSD with a high linearity. An analysis of the influence of doping homogeneity of the resistive layer on the position–response linearity was presented by Noorlag [4.9, 4.10]. Siebert [4.11] showed that the resolution of the PSD is limited by the shot noise in the total current, the thermal noise in the resistive layer and the feedback resistor, and the input offsets of the opamps. For a PSD with a resistance of 25 kΩ, a total current of 1.2 μA and a bandwidth of 10 kHz, the noise level was equivalent to a position resolution of 3 μm.

Photodiode–type two–dimensional PSD's are currently developed with two different structures. In the PSD presented by Woltring and others [4.12, 4.13] an n–type substrate is used as one of the resistive layers, while in the PSD presented by Noorlag [4.14] an epilayer is used. PSD's based on epilayers have several advantages, as electrodes can be provided on the front of the wafer and process steps on the back are avoided. Good electrical isolations along the edges of the device can also be obtained by using a deep p^+–type wall diffusion. In PSD's with the substrate as a resistive layer, such a measure is not applicable. However, the introduction of an epilayer creates also problems. Defects in the form of stacking faults in the epilayer are found, which cause distortions in the position–response grid [4.15]. An effective test method which can be used for the discovery of these defects is discussed by Xing [4.16].

Angular position measurement based on the use of position–sensitive detectors was earlier mentioned by Allen *et al.* [4.17]. Kelly [4.18] used a one–dimensional PSD for the measurement of the angular position of a rotating mirror. A one–dimensional PSD was also used by Reid *et al.* [4.19] in a tilt sensor for the determination of the position of the air bubble. In 1985, Xing and Boeder presented an angular position–sensitive detector (APD) [4.20]. The APD is able to provide output currents which are linear

functions of the angular position of an incident light beam. In order to avoid problems caused by the electrodes across the resistive layer, the device configuration was later modified and is now used in a 12–bit full–range optical encoder [4.21, 4.22].

In this chapter basic differential equations describing the lateral photoeffect in a position–sensitive detector are derived. The potential dependence of the resistive layer thickness is investigated for its effect on the position–response linearity. In section 4.3, the influence of defects and of substrate potential on the performance of two–dimensional PSD's based on epilayers are analyzed. An effective test method for the PSD is presented which can be used for the discovery of defects in the epilayer in an early stage. Angular position–sensitive detectors are discussed in section 4.4. Problems caused by the electrodes, which are placed across the resistive layer, are discussed. The choice between the two–dimensional PSD and the APD for use in the tilt sensor is considered in section 4.5.

4.2 OPERATION OF THE POSITION–SENSITIVE DETECTOR

4.2.1 The lateral photoeffect and the principle of the PSD's

A p–n^+ type junction of large dimensions is considered. It is assumed that the p–type layer thickness is small, and that the n^+–type layer can be considered as an equipotential plane. Two electrodes separated a distance apart are provided on the p–type layer. One electrode is provided on the n^+–type layer. It is further assumed that a light beam with a small diameter is projected on the surface of the p–type layer. In the device electron–hole pairs are generated by the incident light. A part of the holes generated in the n^+–type layer is able to arrive at the depletion layer by diffusion. These holes together with the holes generated in the depletion layer are swept to the p–type layer by the electrical field. A similar process appears for the electrons, as some of the electrons generated in the p–type layer together with the electrons in the depletion layer are swept to the n^+–type layer. These electrons and holes now become majority charge carriers and cancel a part of the space charge in the depletion layer. As a consequence, the depletion layer in the position of the incident light beam becomes thinner, and the electrical potential across the p–n^+ junction in that position becomes smaller. Since the n^+–type layer is an equipotential plane, the change of the potential across the junction occurs only in the p–type layer. Therefore,

a potential gradient is developed in the p–type layer. The potential gradient is dependent on the position of the light beam. It causes the holes in the p–type layer drifting away from the illuminated area along the junction.

Currently developed PSD's are operated with the p–n junction reverse biased. Because of the reverse–bias voltage, the electrons in the n^+–type layer and the holes in the p–type layer are unable to cross the junction and to recombine with the local majority charge carriers. These electrons are collected by the electrode on the n^+–type layer, and the holes by the electrodes on the p–type layer. The current distribution between the electrodes on the p–type layer are dependent on the distances between the light beam and the two separated electrodes. By sensing the currents, the position of the light beam is then determined.

4.2.2 The basic equations

For the derivation of the equations describing the lateral photoeffect in a PSD, a two–dimensional model in the plane parallel to the resistive layer is used. Let us consider the continuity equation for the charge carriers in a p–type layer:

$$\nabla \underline{J} = qG \tag{4.1}$$

with $\underline{J}$ the current density in the layer, G the net charge–carrier generation rate, q the charge of an electron. In Eq.(4.1), it is assumed that the system is in a steady state. The total current density can be described by:

$$\underline{J} = -\sigma_s \nabla \psi \tag{4.2}$$

with σ_s the sheet conductivity, and ψ the electrostatic potential. The net carrier generation rate consists of two components. One is the electric current across the p–n junction as the result of charge–carrier diffusion, which can be described by Shockley's ideal–diode approximation. The other is the electron–hole pair generation due to the presence of the incident light. The carrier generation rate in the p–type material is obtained:

$$(4.3) \qquad G = \frac{J_{pn}}{q} \qquad \text{with} \qquad J_{pn} = J_{ph} - J_s\left[exp\frac{q(\psi_p - \psi_n)}{kT} - 1 \right]$$

where J_{pn} is the current density across the junction, J_s the reverse saturation current density, J_{ph} the generated photocurrent density, kT/q the thermal potential, ψ_p and ψ_n the electrostatic potentials in the p–type and n–type layer, respectively. Substituting Eq.(4.2) and Eq.(4.3) into Eq.(4.1), we obtain the equation describing the lateral photoeffect in the p–type layer:

$$(4.4a) \qquad \nabla(\sigma_s \nabla \psi_p) = - J_{pn}$$

Following the same procedure, the equation for the n–type layer can also be obtained:

$$(4.4b) \qquad \nabla(\sigma_s \nabla \psi_n) = J_{pn}$$

When the conductivity and the thickness of the resistive layer are considered to be constant, Lucovesky's equations are obtained:

$$(4.5a) \qquad \nabla(\nabla \psi_p) = - \frac{J_{pn}}{\sigma_p w_p}$$

$$(4.5b) \qquad \nabla(\nabla \psi_n) = \frac{J_{pn}}{\sigma_n w_n}$$

in which w_p and w_n are the thicknesses, and σ_p and σ_n the conductivities of the p– and n–type resistive layers, respectively. Analytic solutions of Eq.(4.5) can be found when proper conditions are applied. For a photodiode–type PSD, the output currents I_1 and I_2 from the electrodes are derived as [4.14]:

$$(4.6a) \qquad I_1 = I_{pn}(1 - \frac{x_g}{l}) + \sigma_s(\psi_2 - \psi_1)$$

$$(4.6b) \qquad I_2 = I_{pn}\frac{x_g}{l} + \sigma_s(\psi_1 - \psi_2)$$

in which x_g represents the position of the center of gravity of the current density across the junction, l the distance between the two electrodes, I_{pn} the total current intensity across the junction with $I_{pn} = I_{ph} + I_s$, and ψ_1 and ψ_2 the potentials at the two electrodes, respectively. I_{ph} is the generated photocurrent and I_s the leakage current in the PSD.

The photodiode–type PSD can also be operated with voltages instead of currents as the outputs. Assuming that the two electrodes on the resistive layer are terminated with impedances R_1 and R_2 to a common potential, the voltage across the electrodes can be calculated as:

$$(4.7) \qquad V_{21} = \frac{x_g}{l} R_1' I_{pn} - R_2' I_{pn}$$

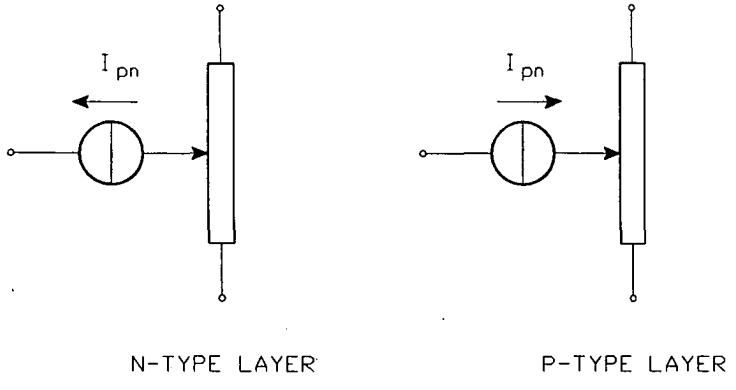

Fig.4.1 Equivalent schemes of one–dimensional position–sensitive detectors with an n–type resistive layer and a p–type resistive layer.

where $R_1' = R_P(R_1+R_2)/(R_1+R_2+R_P)$ and $R_2' = R_P R_1/(R_1+R_2+R_P)$ with R_P the resistance of the resistive layer. The photodiode–type PSD can thus virtually be described as a potentiometer with the resistance R_P combined with a current source I_{Pn}. The electronic equivalent schemes of one–dimensional PSD's are shown in Fig.4.1.

4.2.3 Potential dependence of the resistive layer thickness

In the equations derived by Lucovsky, the assumption is made that the thickness of the resistive layer is constant. However, the appearance of the lateral photoeffect is associated with a nonuniform space charge distribution and a nonconstant potential gradient. Therefore, the thickness of the resistive layer must be also dependent on the potential gradient generated by the light beam. The effect of the resistive layer thickness variation can be strong in PSD's operated with voltage outputs because of the unsymmetrical operational character and the relatively large potential variation.

The influence of the resistive layer thickness variation on the position–response linearity is estimated by means of a one–dimensional model. It is assumed that the light spot is located in the position x_g and it has an infinitely small dimension. The generation of photocurrent can be treated as a delta function of position. The abrupt junction model is used in the calculation of the depletion layer thickness. It can be shown that when the PSD is operated with current outputs, the position–response linearity is not affected. For PSD's operated with voltage outputs, the voltage across the electrodes can be derived to be:

$$(4.8) \qquad V_2 \approx V_m \frac{x_g}{l}\left[1 - \frac{\Delta w V_m}{4 w V_{Pn}} \frac{x_g}{l}\right]$$

where $V_m = I_{Ph}R_P$, V_{Pn} the reverse–bias voltage, w the thickness of the resistive layer, and Δw the depletion layer thickness in the resistive layer. For a p–type resistive layer, given the parameters $I_{Ph} = 10\ \mu A$, $R_P = 20\ k\Omega$, $w = 0.7\ \mu m$, $V_{Pn} = 5$ V, the doping concentrations in the n–type and p–type layers 5×10^{15} cm^{-3} and 2×10^{17} cm^{-3}, respectively, the nonlinear term in Eq.(4.8) is smaller than 0.1 % of the maximum output voltage V_m.

4.3 DEFECT AND SUBSTRATE INFLUENCE

4.3.1 Experiments

Two–dimensional PSD's based on epilayers are fabricated. The structure of the PSD is shown in Fig.4.2. The process parameters are given in [4.14]. The device is 10 × 10 mm^2. Eight devices can be fabricated on a two–inch wafer with the center place reserved for process–control modules (PCM's). For comparison, a test wafer is also made, in which an n–type instead of a p–type substrate is used. No epilayer is used in the test wafer. The p–type implanted layer is made on the n–type substrate.

electrical measurements

Before the wafers are cut and the PSD's are mounted in packages, electrical measurements are carried out on the wafer. Ninety percent of the measured PSD's have a low leakage current, which is typically 2 nA at a reverse–bias voltage of 2 V. The resistances of the resistive layers are measured. Figure 4.3(a) shows the resistance values of the p–type layers on one wafer. Figure 4.3(b) shows those on the test wafer. From the figure we can see that the p–type layers of the PSD's have a large resistance deviation. This is not caused by the ion implantation process, as the resistance deviation of the p–type resistive layers on the test wafer is much smaller.

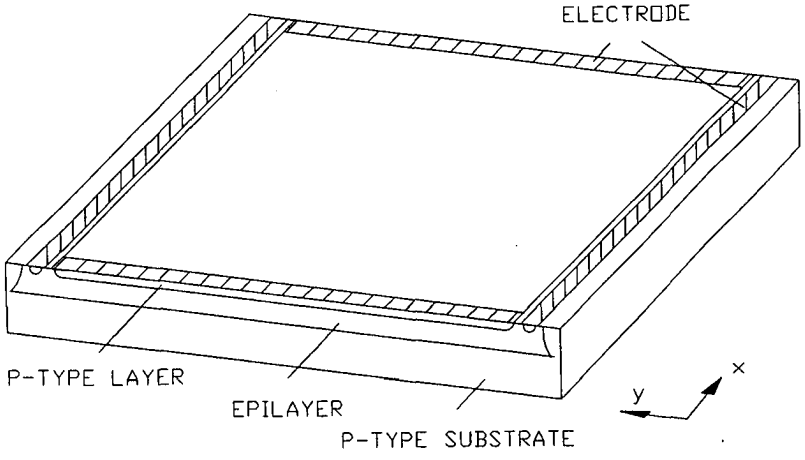

Fig.4.2 Structure of a two–dimensional PSD based on an epilayer.

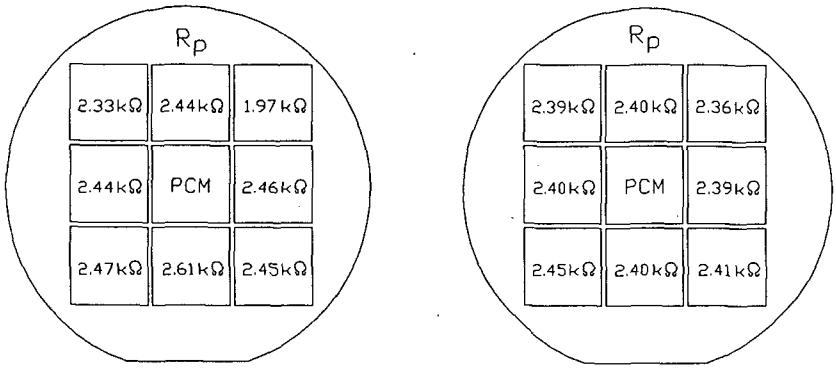

(*a*) $\underline{R} = 2.40\ k\Omega$, $\sigma_{n-1} = 0.19\ k\Omega$
$\sigma_{n-1}/\underline{R} \times 100 = 7.8\ \%$

(*b*) $\underline{R} = 2.40\ k\Omega$, $\sigma_{n-1} = 0.03\ k\Omega$
$\sigma_{n-1}/\underline{R} \times 100 = 1.0\ \%$

Fig.4.3 *Resistance values of the p–type implanted layers fabricated (a) on an epilayer and (b) on an n–type substrate. The standard deviation σ_{n-1} and the average value $\underline{R}$ are calculated.*

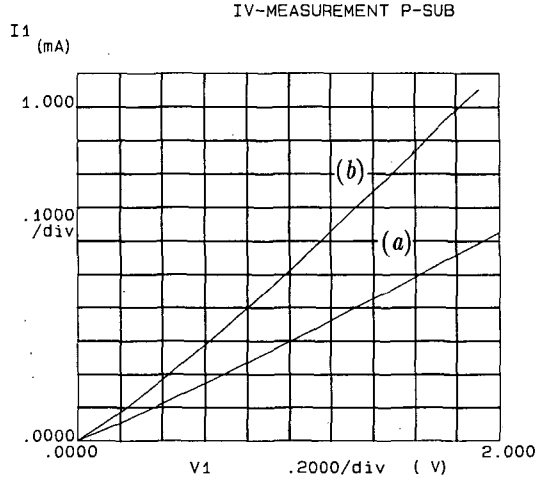

Fig.4.4 *Current–voltage characteristic between the p–type layer and the substrate of one PSD. (a) The measurement is done between one electrode on the p–type layer and the electrode on the substrate, (b) the two electrodes on the p–type layer are connected together.*

Measurements are also done by applying a voltage across the electrode on the p–type layer and the electrode on the substrate. The current is measured. The current–voltage characteristic of one of the PSD's is presented in Fig.4.4, which shows an ohmic relation between the voltage and the current. The typical resistance value is several kilo ohms.

optical measurements

In the optical measurement position–response grids are obtained by measuring the output currents from the electrodes while moving the laser beam in a manner shown in Fig.4.5. The measurement is concentrated on the p–type resistive layer. The measurement results on four PSD's are presented in Fig.4.6 to Fig.4.9. The value of the resistance R_{psub} between the p–type layer and the substrate is also given. For PSD's #1 to #3 measurements have been carried out under two different conditions: the substrate is electrically isolated (the substrate is floating) and the substrate is held at the same potential as the p–type layer. When the electrodes on the p–type layer are terminated with a virtual ground potential and the reverse–bias voltage is applied to the epilayer, the substrate is connected to the ground potential (the substrate is grounded). For PSD #4 the optical measurement is done for both the p–type resistive layer and the epilayer.

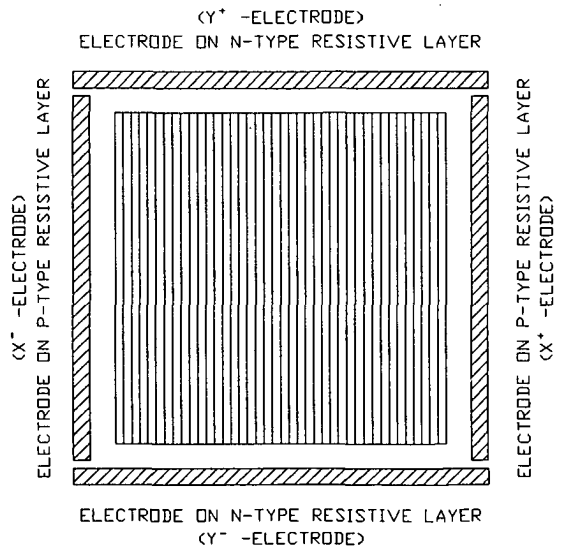

Fig.4.5 Loci of the laser beam. The scanning area is 8 × 8 mm².

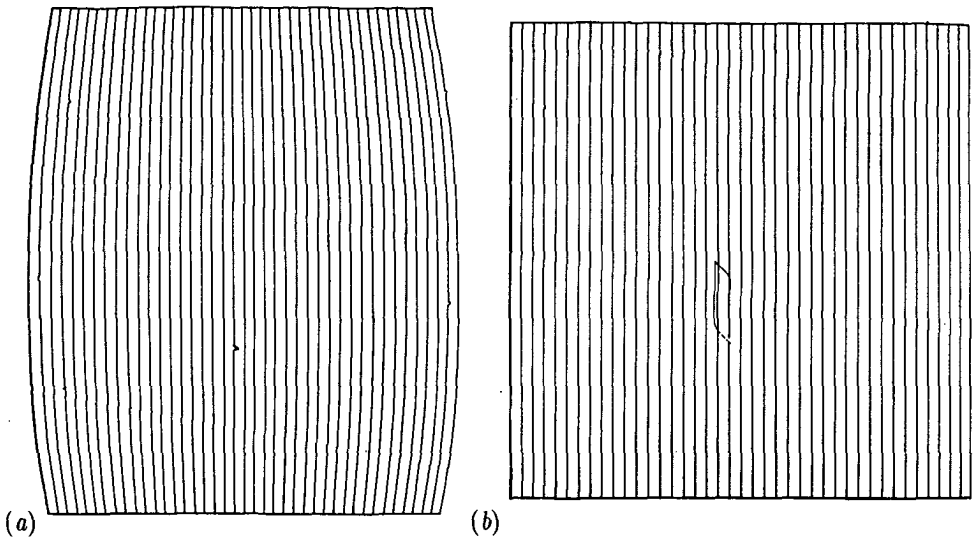

Fig.4.6 *Position–response grids of PSD #1, (a) the substrate is floating, and (b) the substrate is grounded.* R_{psub} *is infinitely large.*

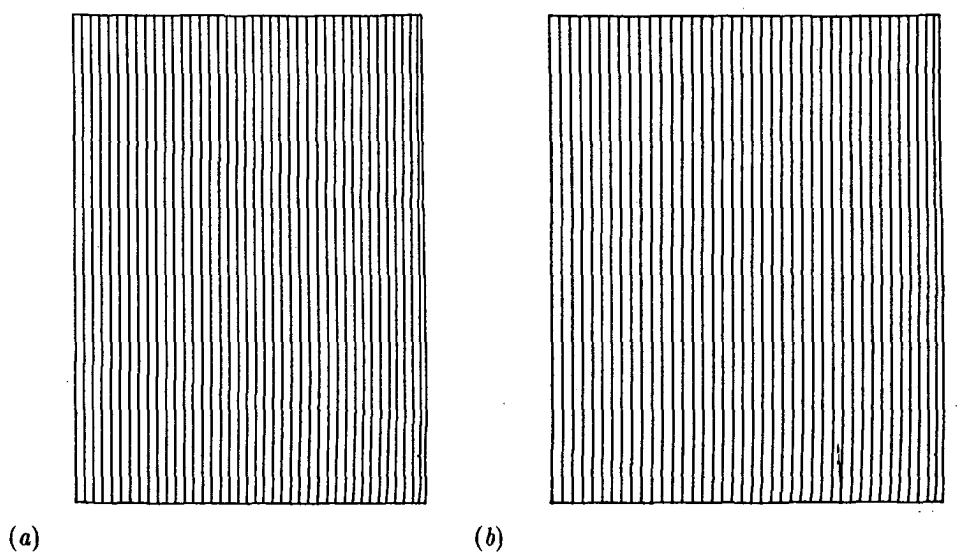

Fig.4.7 *Position–response grids of PSD #2, (a) the substrate is floating, and (b) the substrate is grounded.* $R_{psub} = 10$ *kΩ.*

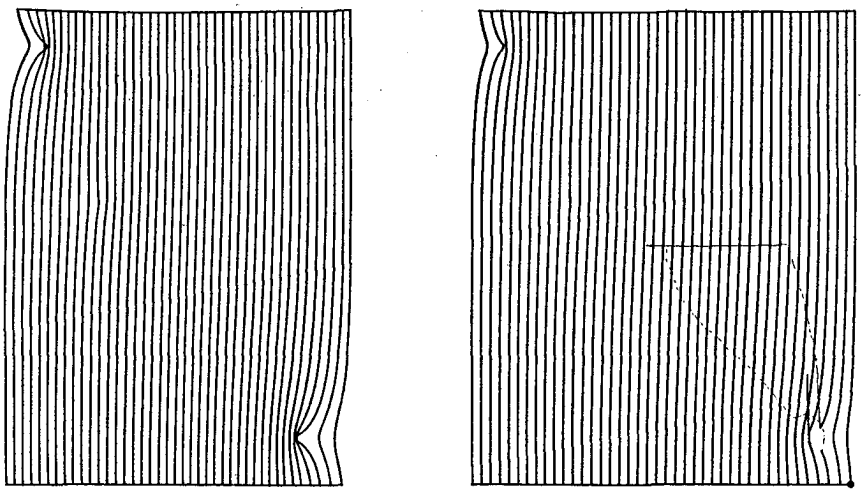

(*a*) (*b*)

Fig.4.8 *Position–response grids of PSD #3, (a) the substrate is floating, and (b) the substrate is grounded.* $R_{psub} = 1.6\ k\Omega$.

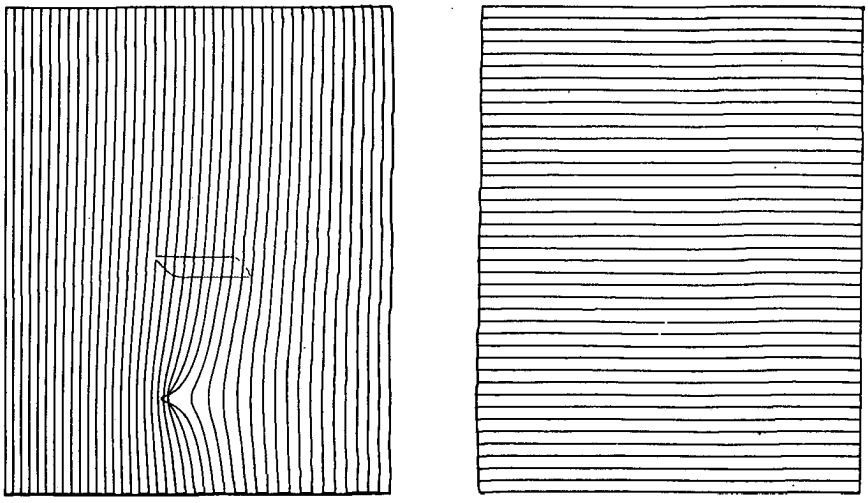

(*a*) (*b*)

Fig.4.9 *Position–response grids of PSD #4 with measurements concentrated (a) on the p–type layer, and (b) on the epilayer.* $R_{psub} = 2.4\ k\Omega$.

The resistance between the p–type layer and the substrate in PSD #1 is infinitely large. This PSD shows a good position–response linearity when the substrate is grounded. But as the contact on the substrate is disconnected, the position–response lines in the grid are deformed. The position–response lines are curved outwards. The grid is contracted in the x–direction and extended in the y–direction. The PSD's shown in Fig.4.7 to Fig.4.9 have finite p–type layer to substrate resistances. In Fig.4.7 no large deformation in the position–response lines can be seen. But the position–response grid in the x–direction is shorter than it should be. Comparing Fig.4.7(a) with Fig.4.7(b) we can see that when the substrate is floating the contraction of the response grid is larger. In Fig.4.8 and Fig.4.9 the position–response lines show large directional and localized distortions. In Fig.4.8 the position–response lines near the left defect bend towards the right electrode while the lines near the right defect bend towards the left. Comparing Fig.4.8(b) with Fig.4.8(a), we can see that when the substrate is put on a ground potential, the extent of the distortions becomes smaller. The PSD's #3 and #4 also show contracted response grids in the x–direction. Measurements are also done for the epilayer. The result is shown in Fig.4.9(b). From the figure it can be seen that no large deformations appear in the position–response grid for the epilayer, even at the locations where the position–response lines are strongly deformed in the p–type layer.

4.3.2 Analysis

PSD without ohmic connection

The position–response deformation shown in Fig.4.6(b) can be attributed to the presence of the potential gradient in the epilayer, which causes a nonuniform current injection from the substrate to the p–type layer. For a floating substrate, the excess holes in the substrate generated by the light are able to cross the junction by diffusion and recombine with the excess electrons in the epilayer. Since the diffusion length of the holes is longer than the thickness of the epilayer (10 μm), it is possible for a considerable number of holes to survive from the recombination process and to reach the lower edge of the upper junction. These holes contribute to the total current which is measured between the p–type layer and the epilayer. The diffusion current from the substrate to the p–type layer is modulated by the electrostatic potential across the lower junction. As the result of the lateral photoeffect, the potential across the lower junction is now dependent on the position of the light beam, and so is the injected current from the substrate to the p–type layer.

PSD with ohmic connection

For PSD's with an ohmic connection between the p–type layer and the substrate, p–type ohmic channels may exist in the epilayer. The localized deformations in the response lines shown in Fig.4.8 and Fig.4.9 suggest that the size of the defect may be very small, since the position response of the epilayer has barely been influenced. These defects, which cause directional deformations, are different from those described by Petersson and Lindholm [4.23]. Peterssons' defects show a symmetrical deformation around the defect location. The cause of the defects was attributed to crystallographic defects associated with precipitates of foreign material, or an inhomogeneous distribution of impurities. In fact, on surfaces of some of the fabricated PSD's, stacking faults are found by microscopic observation. Stacking faults can be formed during the growth of the epilayer if small particles are present on the substrate surface. The ohmic channel can be formed during ion implantation and in the subsequent high temperature process steps.

In the analysis a defect is considered as an extra current generating or absorbing source with a fixed position. When there is one defect in the epilayer, the length of the response grid l_{eff} and the shift of the zero point Δx for the p–type layer are:

$$(4.9) \qquad l_{eff} = \frac{I_{ph}}{I_{ph} + I_{def}} l \qquad \text{and} \qquad \Delta x = \frac{I_{def}(2x_d/l - 1)}{I_{ph} + I_{def}} l$$

in which I_{ph} is the photocurrent, l the resistive layer length, I_{def} the current through the defect, and x_d the position of the defect on the x–axis. The current I_{def} is defined as positive when it flows from the substrate to the p–type layer. From Eq.(4.9) we can see that due to the presence of the defect, the length of the response grid and the zero point measured by the PSD are changed.

Figure 4.10(a) shows the situation in which one defect is present and the substrate is floating. Since the photocurrent generated in the lower junction can only flow to the resistive layer through the defect, the value of I_{def} is always positive. Therefore, the position–response grid is shorter than the real resistive layer length. When the electrode on the substrate is grounded, as Fig.4.10(b) shows, the photocurrent generated in the lower junction flows directly to the electrode on the substrate. Because the local potential in the p–type layer is always higher than that in the substrate, the current I_{def} should be negative. This means an increased grid length.

But from Fig.4.7(b) we can see that the grid length is longer than when the substrate is floating, but it is still shorter than the real layer length. This might be due to the existence of contact resistance between the aluminum electrode and the silicon substrate. A portion of the photocurrent generated in the lower junction still can flow to the p–type layer.

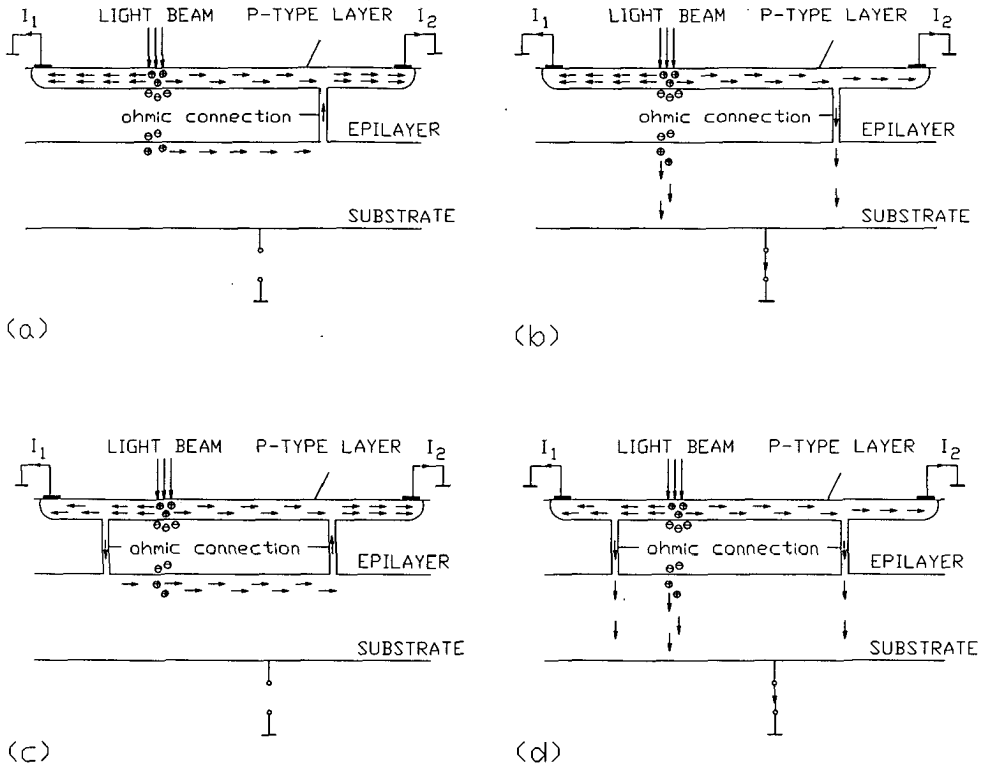

Fig.4.10 *Schematic illustrations of PSD's with ohmic connections between the p–type resistive layer and the substrate: (a) one defect, the substrate is floating, (b) one defect, the substrate is grounded, (c) two defects, the substrate is floating, and (d) two defects, the substrate is grounded.*

Figure 4.10(c) and Fig.4.10(d) depict the situations where the PSD has two defects in the epilayer. For a floating substrate the defects together with the substrate form a current path. As fig.4.10(c) shows, when the light beam is moved close to the left defect, a part of the photocurrent, which should go to the left electrode, is diverted to the substrate through the left defect, flows back to the resistive layer through the right defect and is finally collected by the right electrode. This causes a shift of the measured light spot position to the right. The measured position shift is smaller when the light beam is moved to the left of the left defect. Because, in this case, although by taking a different path, the photocurrent which is diverted to the substrate by the defects still flows to the same electrode as it should. This explains the directional deformation of lines in the position–response grid shown in Fig.4.8(a). When the substrate is put on a fixed potential, the directional deformation should disappear. But Fig.4.8(b) only shows a slight decrease in the deformation. This again may be the result of the contact resistance between the electrode and the substrate.

4.3.3 Numerical simulation

mathematical formulation of the computer model

In order to investigate the influence of the defect and of the substrate potential, numerical simulations are carried out. In the simulation the substrate is treated as an equipotential surface. For a PSD without an ohmic connection and operated with a floating substrate, the differential equations for the p–type layer and the epilayer, respectively, can be obtained by using a pnp transistor model [4.24]:

$$\text{(4.10a)} \qquad \nabla^2\psi_p = -\frac{1}{\sigma_s}\left[J_{ph,u} + J_{01}exp(\frac{qV_{se}}{kT})\right]$$

$$\text{(4.10b)} \qquad \nabla^2\psi_n = \frac{1}{\sigma_s}\left[J_{ph,u} + J_{ph,l} - J_{02}exp(\frac{qV_{se}}{kT})\right]$$

in which $J_{ph,u} = (x, y|x_0, y_0)$ and $J_{ph,l} = (x, y|x_0, y_0)$ are the photocurrent densities across the upper and lower junctions, respectively, J_{01} and J_{02} constants depending on geometric and material parameters, and $V_{se} = V_{se}(x, y)$ the local voltage across the junction between the substrate and the epilayer. The light spot is located at the position (x_0, y_0).

In the simulation of PSD's with defects, the photocurrent generation in the lower junction is ignored. The resistance values through each defect are considered to be equal. Suppose that the number of defects in the PSD is n ($n \geq 1$), then the extra boundary conditions imposed on the differential equation at places where the defects are located are:

(4.11a) $$\sum_{i=1}^{n} I_i = 0$$ for a floating substrate

and

(4.11b) $$I_1 + I_2 + \sum_{i=1}^{n} I_i = I_{ph}$$ for a grounded substrate

with $I_i = (\psi_i - \psi_{sub})/nR_{Psub}$, where I_i is the current through the ith defect, I_1 and I_2 the currents through the electrodes on the p–type layer, R_{Psub} the resistance between the electrodes on the p–type layer and on the substrate, ψ_i the potential in the p–type layer at the position where the ith defect is located, and ψ_{sub} the substrate potential. For a grounded substrate $\psi_{sub} = 0$.

The differential equations are solved by means of the finite difference method with a square net discretization. A large system of linear algebraic equations is obtained. This system has been solved on a computer with the aid of the successive over–relaxation method (sor). For each position of the light spot the potential distribution in the resistive layer is calculated and, accordingly, the output currents are obtained.

Since the computational time increases with the factor n^4, where n is the number of mesh points along one axis, a calculation of the light spot position at each mesh point is practically impossible. In order to reduce the computational work, two different position grids are used. One grid covers the whole device area with a large step size. The other is more locally concentrated in an area around the defect and has a smaller step size. Besides the influence on the accuracy of the numerical solutions, the number of mesh points n also determines the size of the defect, which is given by $l/(n-1)$, where l is the resistive layer length. For a PSD of 10 × 10 mm^2 and $n = 165$, the dimensions of the defect are 60.9 × 60.9 μm^2.

simulation results

The simulation results are presented in the form of relief maps. The maps overlay the resistive layer and the lines on the maps are the loci of the center of gravity of the light beam. The calculated position–response grid for the p–type layer of a PSD without an ohmic connection in the case of a floating substrate is presented in Fig.4.11, which shows a good agreement with the measurement results. Simulation results of the epilayer show an increased grid length in the y–direction, which is in agreement with the measurement results as well.

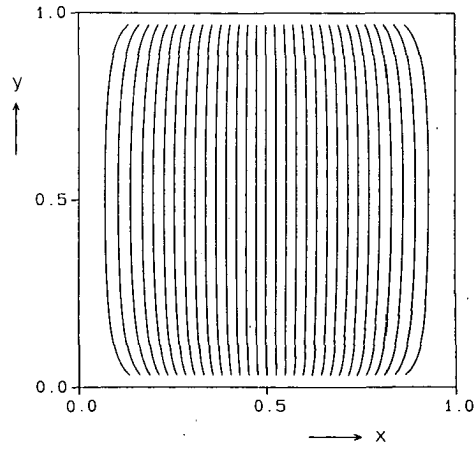

Fig.4.11 *Calculated position–response grid of a PSD without an ohmic connection between the p–type layer and the substrate in the case of a floating substrate.*

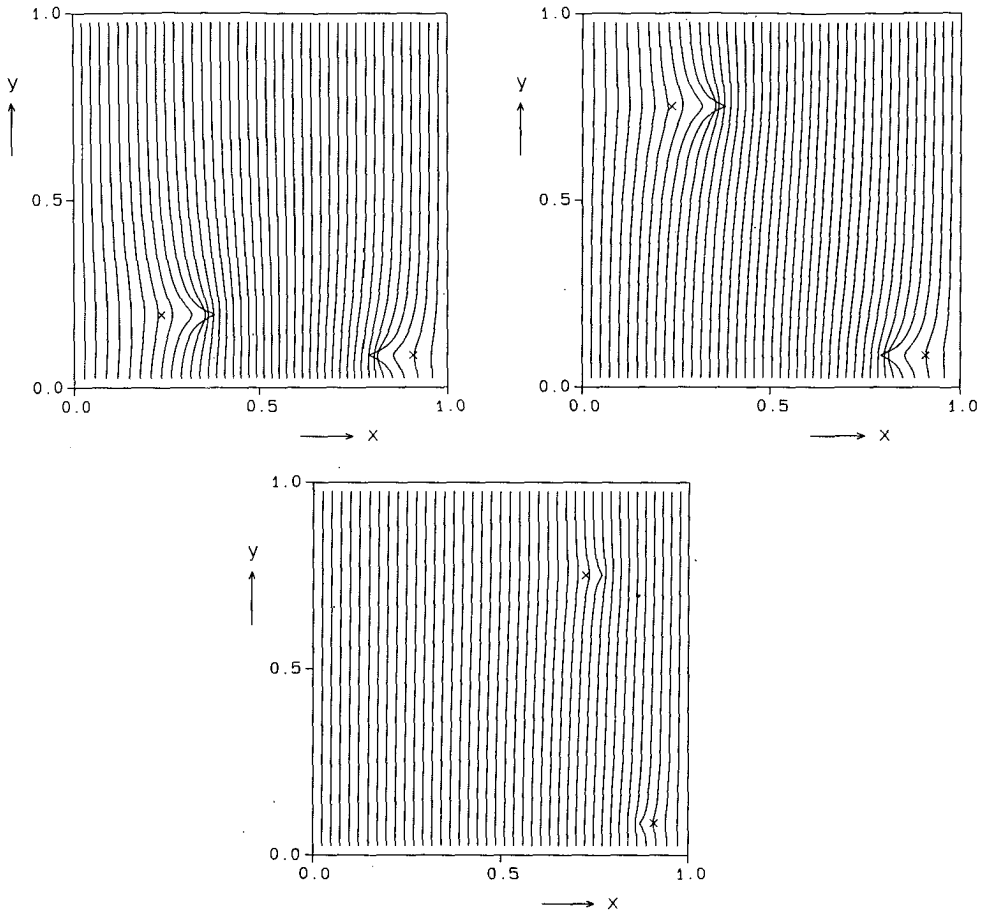

Fig.4.12 *Calculated position–response grids of PSD's with two defects in the epilayer at different locations. The substrate is floating.* $R_{psub} = 1\ k\Omega$.

The position–response grids for PSD's with two defects in the epilayer are presented in Fig.4.12 and Fig.4.13. The total p–type layer to substrate resistance is 1 kΩ. Calculations have been made for three different relative locations of the two defects. From Fig.4.12 we can see that, for a floating substrate, as the two defects approach each other in the x–direction, the deformation becomes smaller. The relative locations of the defects on the y–axis have a minor influence on the extent of the deformation. This is the result of the local potential difference between the two defects. When the distance between the defects in the x–direction becomes smaller, the potential difference becomes smaller, and also the diverted current.

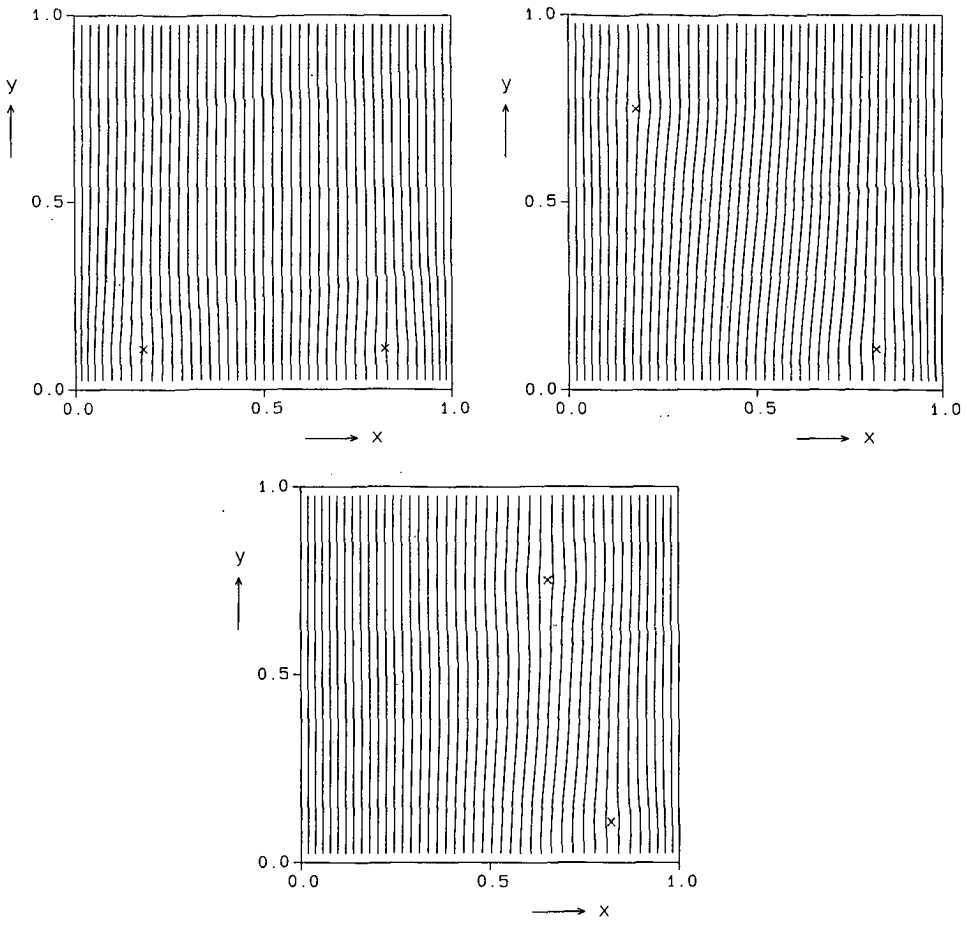

Fig.4.13 *Position–response grids of PSD's with two defects in the epilayer at different locations. The substrate is grounded.* $R_{\mathrm{psub}} = 1\ \mathrm{k\Omega}$.

Figure 4.13 gives the computational results for the case where the substrate is held on the same potential as the p–type layer. The large distortions in the position–response grid disappear on all the three maps. It can be seen that the largest deformation occurs when the defects are located in a diagonal position. The place where the largest deformation appears is not around the defect, but in a position between the two defects. The lines shift to the left when the light spot is moved into the lower half of the PSD, and shift to the right when the light spot is moved into the upper half of the device. This is because, when the light spot is in the lower half, relatively more photocurrent flows to the defect on the right. The electrode on the right receives less current than it should. The deformation in the lines is the smallest when the two defects are located at the same position on the y–axis.

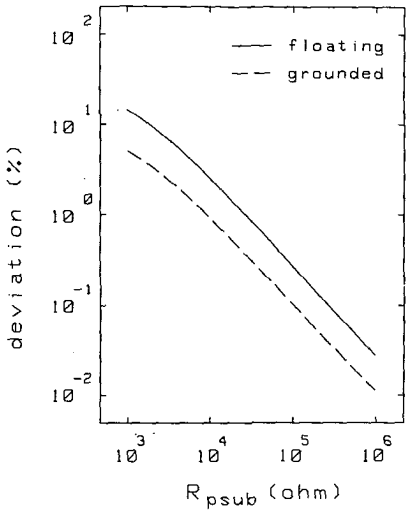

Fig.4.14 *Maximum deformation in the position–response grid as a function of the resistance R_{psub} for a floating and a grounded substrate.*

The maximum deformation as a function of the resistance between the p–type layer and the substrate for a floating and a grounded substrate are depicted in Fig.4.14. As the figure shows, the maximum deformation decreases with the p–type layer to substrate resistance. This indicates that during the electrical measurement the quality of the PSD's can be evaluated in regard to the resistance between the implanted layer and the substrate.

4.4 THE ANGULAR POSITION–SENSITIVE DETECTOR

4.4.1 Theory

In order to derive the relation between the position of an incident light beam and the output currents from the APD, a calculation is carried out on a p–type resistive layer. Referring to Fig.4.15, electrodes along the boundaries $\phi_1 = 0$ and $\phi_2 = \alpha$ $(0 < \alpha < 2\pi)$ of the p–type layer are assumed to have infinitely large conductivities, while perfect isolations (conductivity zero) are assumed along the sides $r = r_1$ and $r = r_2$. Following assumptions are further made: (a) the device operates in a steady

state, (b) the sheet conductivity of the resistive layer is constant, (c) a reverse–bias voltage is applied. Equation (4.4a) can be written as:

$$\nabla^2\psi_p = -\frac{1}{\sigma_s}J_{pn} \tag{4.12}$$

where ∇ is the partial differential operator in a cylindrical coordinate system, σ_s the sheet conductivity, and J_{pn} the current density across the junction.

The boundary conditions imposed on Eq.(4.12) are homogeneous or inhomogeneous Dirichlet conditions (potential zero or constant) along the edges $\phi_1 = 0$ and $\phi_2 = \alpha$, and homogeneous Neumann conditions (normal component of field strength $\mathbf{n}\cdot\nabla\psi = 0$) along the edges $r = r_1$ and $r = r_2$. Applying Green's theorem, Eq.(4.12) has a general solution in the form [4.25]:

$$\psi_p(r,\phi) = \iint_S \frac{1}{\sigma_s}J_{pn}(r_0,\phi_0)G(r,\phi|r_0,\phi_0)\,dS_0 + \oint_c \psi_p(r_0,\phi_0)\mathbf{n}\cdot\nabla_0 G(r,\phi|r_0,\phi_0)\,dc_0 + \oint_c G(r,\phi|r_0,\phi_0)\mathbf{n}\cdot\nabla_0\psi_P(r_0,\phi_0)\,dc_0 \tag{4.13}$$

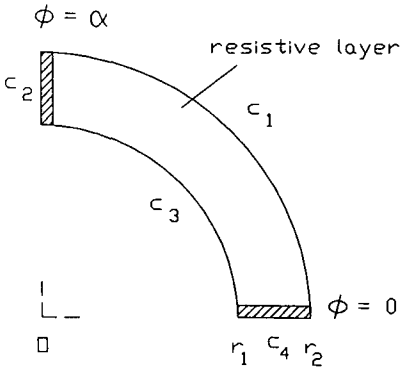

Fig.4.15
Sketch showing the resistive layer with parameter definitions.

where ∇_0 designates the differentiation with respect to r_0 and ϕ_0, and $G(r,\phi|r_0,\phi_0)$ is the Green's function defined as:

$$\nabla^2 G = -\frac{1}{r_0}\,\delta(r-r_0)\delta(\phi-\phi_0) \tag{4.14}$$

The following boundary conditions must be obeyed:

$$G|_{c_2} = G|_{c_4} = 0 \qquad \text{and} \qquad \boldsymbol{n}\cdot\nabla G|_{c_1} = \boldsymbol{n}\cdot\nabla G|_{c_3} = 0$$

The solution of Eq.(4.14) with the associated boundary conditions is found to be:

$$G(r,\phi|r_0,\phi_0) = \frac{1}{ln(r_2/r_1)}\begin{cases}\dfrac{\alpha-\phi_0}{\alpha}\,\phi \\ \dfrac{\phi_0}{\alpha}(\alpha-\phi)\end{cases} \tag{4.15}$$

$$+\sum_{n=1}^{\infty}\frac{2}{\pi n}\cos\left[\pi n\frac{ln(r_0/r_1)}{ln(r_2/r_1)}\right]\cos\left[\pi n\frac{ln(r/r_1)}{ln(r_2/r_1)}\right]$$

$$\times\begin{cases}\dfrac{sinh\beta(\alpha-\phi_0)}{sinh\beta\alpha}\,sinh\beta\phi & 0\le\phi<\phi_0 \\ \dfrac{sinh\beta\phi_0}{sinh\beta\alpha}\,sinh\beta(\alpha-\phi) & \phi_0<\phi<\alpha\end{cases}$$

where $\beta = \pi n/ln(r_2/r_1)$. The current from the ith electrode is determined by:

$$I_i = -\oint_{e_i}\sigma_s\boldsymbol{n}\cdot\nabla\psi_P\,de_i \qquad i=1,2 \tag{4.16}$$

where e_i represents the contour integral around the ith electrode. By substituting Eq.(4.13) into Eq.(4.16), the current I_1 from the first electrode becomes:

$$(4.17) \qquad I_1 = \int_{r_1}^{r_2} \frac{1}{r} \left[\frac{\partial}{\partial \phi} \iint_S J_{pn} G \, dS_0 + \oint_c \sigma_s \psi_p \boldsymbol{n} \cdot \nabla_0 G \, dc_0 \right] dr$$

Substituting Eq.(4.15) into Eq.(4.17) we obtain:

$$(4.18a) \qquad I_1 = I_{pn}(1 - \frac{\phi_g}{\alpha}) + \frac{\sigma_s}{\alpha} ln\frac{r_2}{r_1} (\psi_2 - \psi_1)$$

where

$$I_{pn} = \iint_S J_{pn} \, dS_0 \qquad \text{and} \qquad \phi_g = \frac{\iint_S \phi_0 J_{pn} \, dS_0}{\iint_S J_{pn} \, dS_0}$$

in which I_{pn} is the total current across the p–n junction and ϕ_g the center of gravity of the current density across the junction. The current from the second electrode can be obtained by following the same procedure:

$$(4.18b) \qquad I_2 = I_{pn} \frac{\phi_g}{\alpha} + \frac{\sigma_s}{\alpha} ln\frac{r_2}{r_1} (\psi_1 - \psi_2)$$

Equation (4.18) is very similar to Eq.(4.6) which is found for the rectangular PSD's.

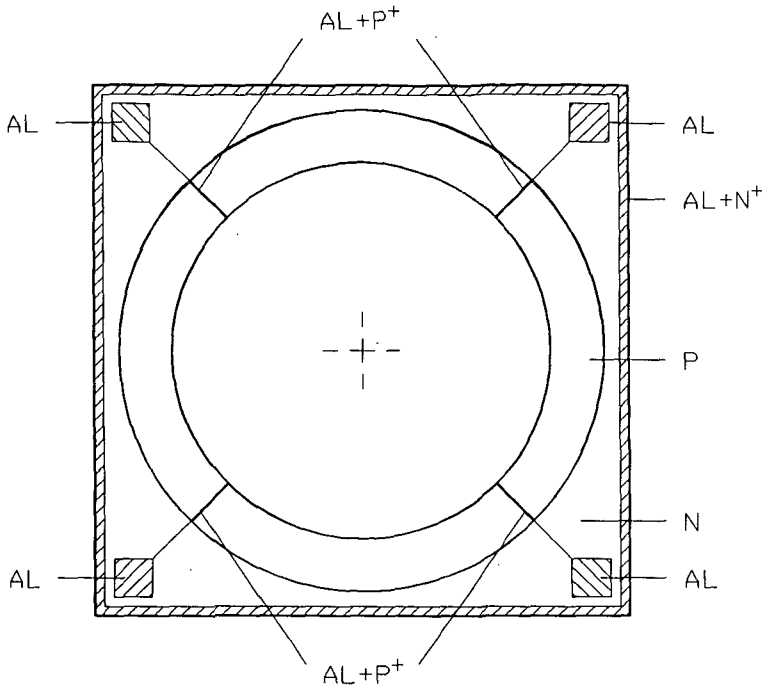

Fig.4.16 Structure of the angular position–sensitive detector.

4.4.2 Design considerations and process technology

The top view of an angular position–sensitive detector is shown in Fig.4.16. A shallow ring–shaped p–type layer is implanted on an n–type high ohmic substrate. Four equidistant aluminum electrodes are placed across the resistive layer. These electrodes are necessary for the measurement of the light spot position in a 360–degree range. Beneath each electrode p^+ diffusion is applied to provide a good ohmic contact to the ion–implanted layer. Both the aluminum electrode and the p^+–diffusion layer are made as narrow as possible (10 μm). Along the edges of the detector n^+–type diffusion is performed and aluminum electrodes are supplied to provide contacts to the substrate. The device is 15 × 15 mm^2. The inner radius r_1 = 4.75 mm and the outer radius r_2 = 6.5 mm.

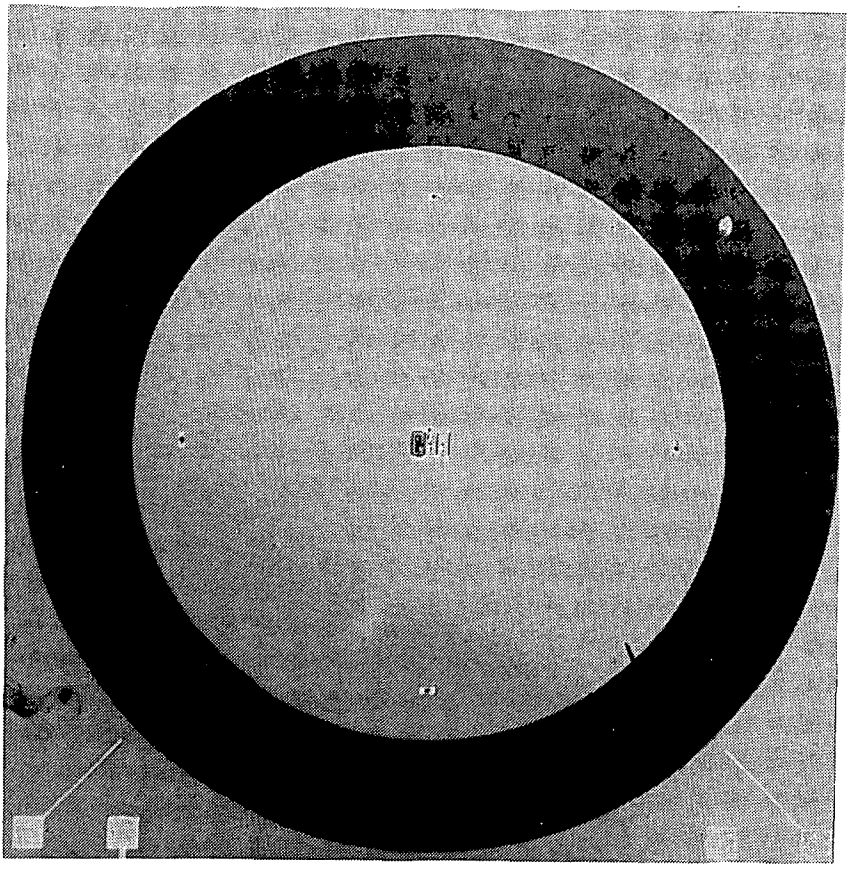

Fig.4.17 Photograph showing the angular position–sensitive detector.

Five masks have been used in manufacturing the APD:

– one for the p^+–type contact diffusion,
– one for the p–type ion implantation,
– one for the n^+–type contact diffusion,
– one for etching contact holes,
– one for the aluminum electrodes.

A modified TUD–01 process is used which starts with boron deposition for the p^+–type contact diffusion (temperature: 920 ^{0}C, time: 20 min) on an n–type substrate (resistivity: $5 - 8\ \Omega$cm, thickness: 500 μm). It is followed by a drive–in step (temperature: 1130 ^{0}C, drive time: 50 min, cooling time: 45 min). The n^+–type diffusion is then carried out with phosphorus deposition (temperature: 1000 ^{0}C, time: 12 min) followed by a drive–in step (temperature: 100 ^{0}C, drive time: 30 min, cooling time: 20 min). After 15 min oxidation at a temperature of 1000 ^{0}C, boron

implantation is carried out with a dose of 3×10^{13} cm^{-2} and an energy of 70 keV. This is followed by an annealing step (temperature: 900 ^{0}C, time: 30 min) and a drive–in step (temperature: 1000 ^{0}C, drive time: 15 min, cooling time: 45 min). The process is ended with the mask for the contact holes, the aluminum evaporation, the mask for the aluminum electrodes, and an alloying step at a temperature of 450 ^{0}C with a duration of 20 min. The resistive layer has a sheet resistivity of 2 kΩ. The leakage current of the APD is measured with a Keithley Electrometer. It has a typical value of 2.5 nA for a reverse–bias voltage of 1 V. The breakdown voltage is normally higher than 15 V. A photograph of the device is shown in Fig.4.17.

4.4.3. Experimental results

The currents from the electrodes are measured with current–voltage converters built with low offset opamps and feedback resistors (100 kΩ). The reverse–bias voltage is applied to the n–type substrate. Figure 4.18 shows the measured output current from one of electrodes as a function of the angular position of the light spot. It can be seen that the output current varies linearly with the angular position of the light spot. In order to investigate the dependence of the output current on the radial position of the light spot, the light spot is moved across the active layer in the radial direction several times with fixed angular positions. Figure 4.19 shows the results. In the figure, the output current increases slightly as the light spot moves outwards, which is probably the result of a concentric error of the device with the rotation table.

The APD shows a high linearity within its main active area, but in positions around the electrodes deviations occur. Measurement results show that the total current has a 1 % to 7 % decrease when the light spot moves across the electrode. The decrease in the total current depends on the size of the light spot. A small light spot results in a large decrease. In case of directly using the output current as a measure of the light spot position, a decrease in the total current means a deviation of the measured light spot position from the real position. For a light spot with a diameter of 0.3 mm, a maximum deviation of about 6 degrees is measured. By enlarging the light spot diameter to 1.1 mm, the deviation is reduced to about 2 degrees. The device linearity around the electrode is greatly improved when the output currents are divided by the total current. In this case the deviation for a 0.3 mm light spot is reduced to 0.4 degrees, while for a 1.1 mm light spot the deviation is still about 2 degrees.

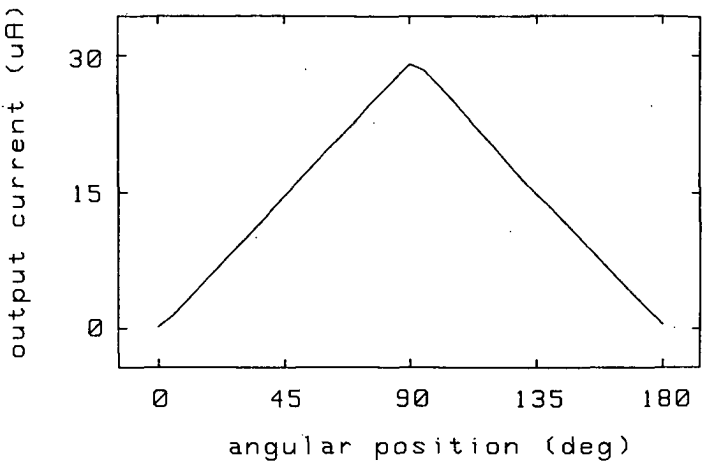

Fig.4.18 *The output current measured from one of the electrodes as a function of the angular position of the light spot. Reverse–bias voltage*: 3 *V, radial position*: 5.7 *mm, light spot size*: 0.3 *mm.*

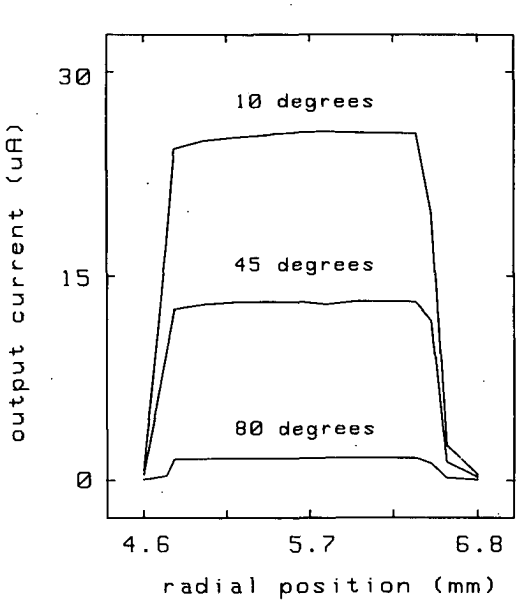

Fig.4.19 *The output current measured from one of the electrodes as a function of the radial position of the light spot with the angular position as a parameter. Reverse–bias voltage*: 3 *V, light spot size*: 0.3 *mm.*

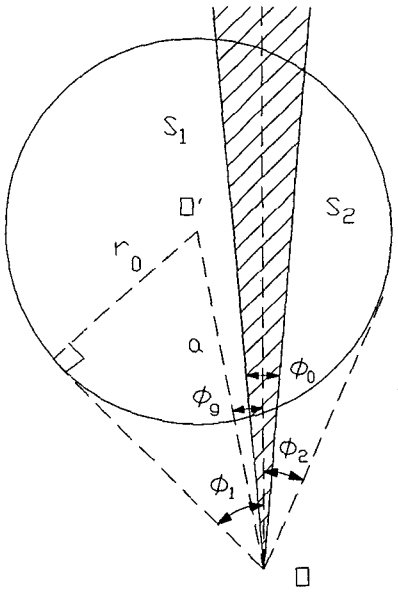

Fig.4.20
Sketch showing the fan-shaped electrode illuminated by a circular light spot.

The influence of the electrodes can be evaluated by means of a simple model. It is assumed that the electrodes have a fan shape with an angle ϕ_0, as shown in Fig.4.20. The light spot has a uniform density distribution. The generated photocurrent density in the device can thus be described by: $J_{ph} = J_{ph0}$ in the region illuminated by the light spot and $J_{ph} = 0$ otherwise. The photocurrent generation in the region masked by the aluminum electrode is also zero.

As Fig.4.20 shows, when the light spot moves across the electrode, the light spot is divided into two subregions S_1 and S_2. The angular positions of the centers of gravity of the light spots in each subregion are ϕ_{g1} and ϕ_{g2}, respectively. ϕ_g is the exact angular position of the light spot. The photocurrent I_1 from this electrodes is then:

$$(4.19) \qquad I_1 = I_{s1} + I_{s2} = I_{ph1}(1 - \frac{\phi_{g1}}{\alpha}) + I_{ph2}(1 + \frac{\phi_{g2}}{\alpha})$$

where α is the distance between the electrodes, I_{s1} and I_{s2} the currents from the two subregions S_1 and S_2, respectively, and I_{ph1} and I_{ph2} the photocurrents generated in these subregions. The relations between ϕ_g, ϕ_{g1} and ϕ_{g2} are found to be:

$$\phi_{g1} = \frac{2a}{A_1} \int_{\phi_0/2}^{\phi_1} \phi cos(\phi_g - \phi) \left[r_0^2 - a^2 sin^2(\phi_g - \phi) \right]^{1/2} d\phi \tag{4.20}$$

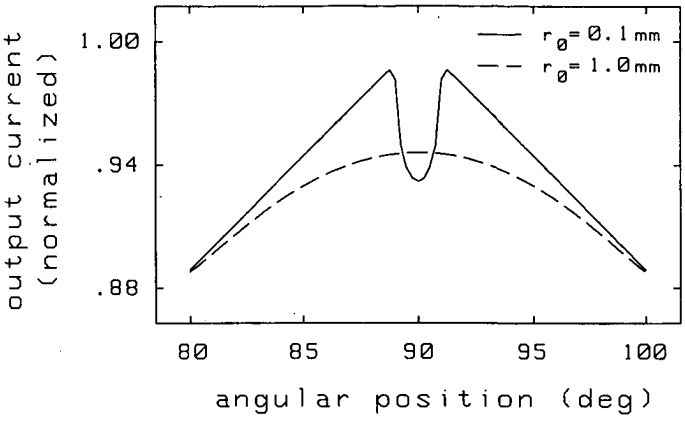

Fig.4.21 *The calculated output current from one electrode as a function of the light spot position with the radius of the light spot r_0 as a parameter. Center position of the electrode: 90 degrees.*

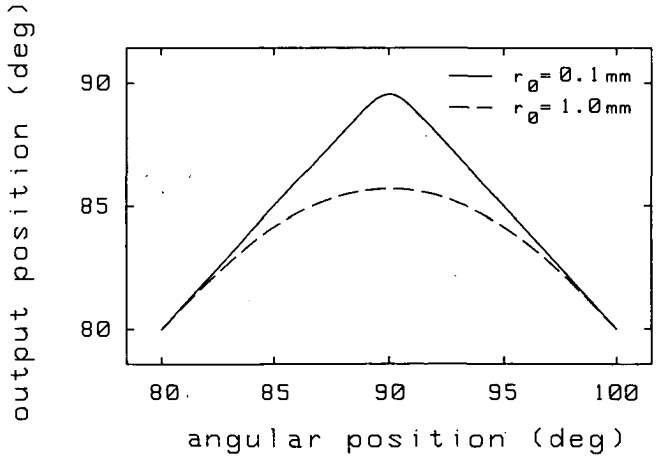

Fig.4.22 *For the same electrode. The output current is divided by the total current. Center position of the electrode: 90 degrees*

and

$$(4.21) \qquad \phi_{g2} = \frac{2a}{A_2} \int_{\phi_2}^{-\phi_0/2} \phi cos(\phi_g - \phi) \left[r_0^2 - a^2 sin^2(\phi_g - \phi) \right]^{1/2} d\phi$$

in which $\phi_1 = arcsin\ (r_0/a) + \phi_g$ and $\phi_2 = -\ arcsin\ (r_0/a) + \phi_g$ with r_0 the radius of the light spot, a the distance between the center of the detector and the center of the light spot, A_1 and A_2 the areas of the subregions S_1 and S_2, respectively.

The integrals in Eq.(4.20) and Eq.(4.21) are solved numerically. The values applied in the calculations are $\alpha = 90$ degrees, $\phi_0 = 0.1$ degree and $a = 5.6$ mm. The results are depicted in Fig.4.21 and Fig.4.22, which show agreement with the experimental results. From the figure it can be seen that, for a light spot with a small size, the current drops sharply when it is moved across the electrode. The deviation is reduced after the output current is divided by the total current. The maximum deviation is reduced only a little when the light spot is large. The residual deviation can be calculated when the light spot is at the position $\phi_g = 0$, then it holds that $\phi_{g1} = -\phi_{g2}$ and $I_{ph1} = I_{ph2}$. From Eq.(4.19) we obtain:

$$(4.22) \qquad \phi_{out} = \frac{I_{s1} + I_{s2}}{I_{ph}} = (1 - \frac{\phi_{g1}}{\alpha})\ \alpha$$

From Eq.(4.22) we can see that the deviation $\Delta\phi = \alpha - \phi_{out} = \phi_{g1}$, never vanishes. Equation (4.22) also shows that the deviation of the measured value from the exact value becomes dependent on the size of the light spot. Calculated results show that the deviation increases with the size of the light spot. A good approximation can be made from Eq.(4.22) if we assume that $a >> r_0 >> a\phi_0$, which leads to:

$$\Delta\phi \approx \frac{240}{\pi^2 a} r_0 \text{ (deg)}$$

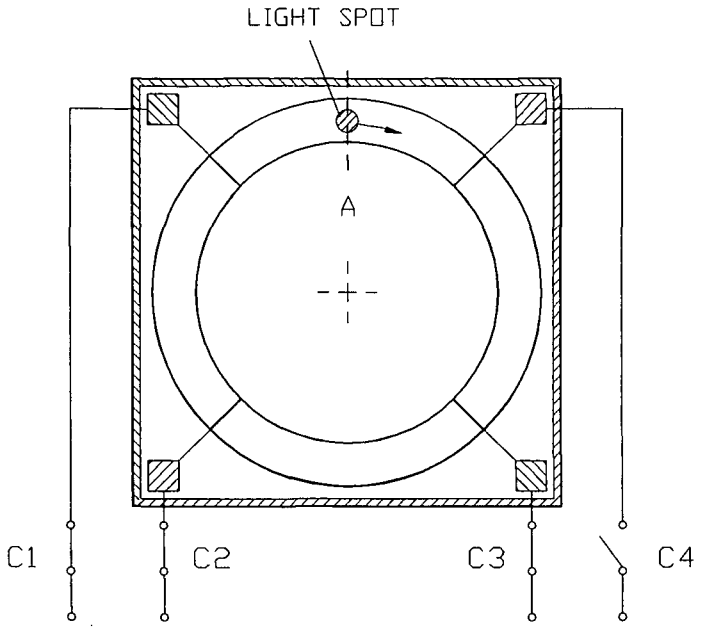

Fig.4.23 *The APD is operated with current switches to avoid problems caused by the electrodes.*

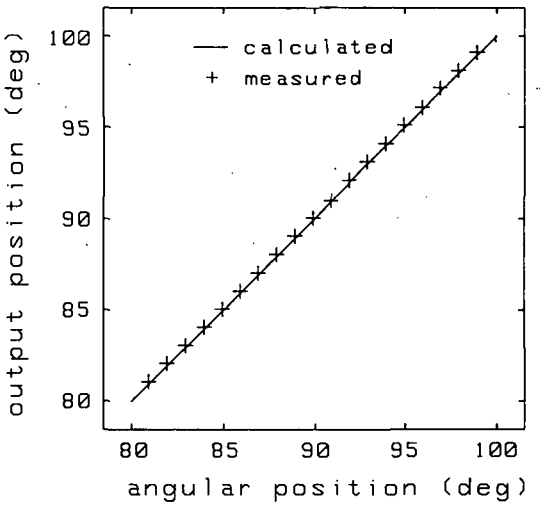

Fig.4.24 *Measurement and calculated results of the position response around one electrode. Center position of the electrode:* 90 *degrees.*

4.4.4 Improvements

Improvements in the performance of the angular position–sensitive detector around the electrodes can be made by either operating the APD in a different way, or by adopting a configuration in which electrodes across the resistive layer are not required.

operating the APD with current switches

The problem of having two separate light spots is avoided when the APD is operated in a way shown in Fig.4.23. Four current switches are used, one for each electrode. During operation, when the light spot moves across a certain predefined line, say line A, the switch C_4 is set open, while the other three remain closed. The electrode connected with the switch C_4 then becomes an obstacle on the device surface, which only causes a slight drop in the photocurrent. When the output currents measured from the other electrodes are divided by the total current, the deviation disappears at the point where the center of gravity of the light spot coincides with the center line of the electrode. The measurement range becomes now 180 degrees. The light spot position determined by measuring the currents from the neighboring electrodes is now determined by:

$$\phi_{out} = \frac{\phi_{g1} I_{s1} + \phi_{g2} I_{s2}}{I_{ph}} \tag{4.23}$$

When $\phi_g = 0$, $I_{s1} = I_{s2}$ and $\phi_{g1} = -\phi_{g2}$, $\Delta\phi = \phi_g - \phi_{out} = 0$. The measurement results and the calculated values are presented in Fig.4.24.

APD with two separate resistive layers

Figure 4.25 illustrates an APD with two separate resistive layers which are rotated 180 degrees with respect to each other. Each resistive layer extends 270 degrees. Since only a measurement range of 180 degrees is used, the disturbances from the electrodes are avoided. APD's with this configuration are fabricated by using the TUD–01 process and later on also by using the TUD–06 process, which allows the integration of on–chip signal– processing circuits (Chapter 5). The device is 10 × 10 mm^2. The outer resistive layer has an outer diameter of 4.8 mm and an inner diameter of 3.825 mm; the inner resistive has an outer diameter of 3.775 mm and an inner diameter of 2.8 mm.

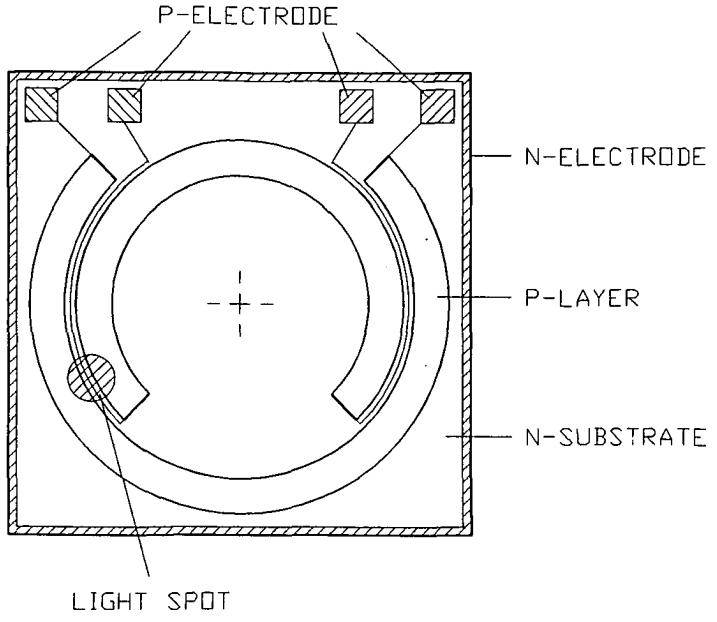

Fig.4.25 *Structure of the modified APD consisting of two separate resistive layers. Each layer extends 270 degrees.*

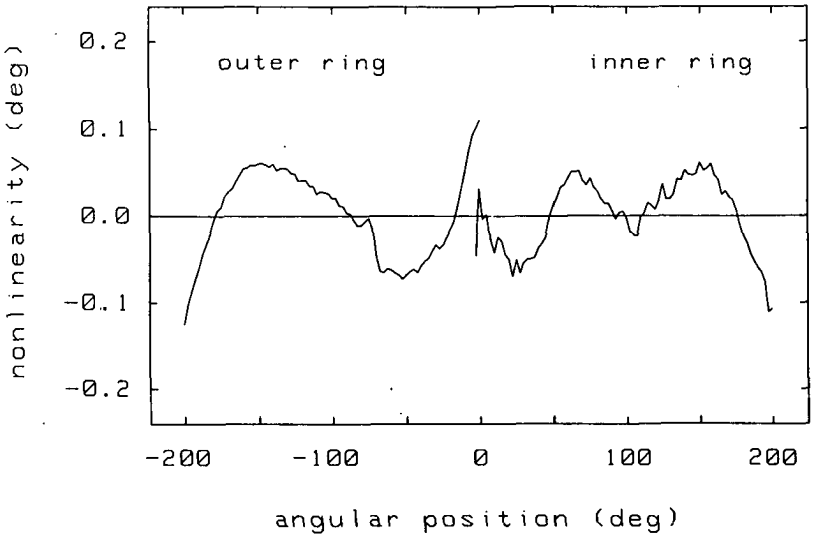

Fig.4.26 *The measured position–response nonlinearity of the modified APD. Reverse–bias voltage: 3 V, light spot size 0.3 mm.*

As Fig.4.26 shows, the measured position–response linearity with respect to the best straight line is ± 0.1 degree in the main region of each layer. The nonlinearity in the position response is, in fact, the result of a concentric error between the center of the circular track of the light spot and the center of the APD. Another factor which may cause position–response nonlinearity is the inhomogeneity of the resistive layer. During the ion–implantation step, the wafer is tilted 7 degrees away from the direction of the incident ion beam in order to avoid channeling effects. This can cause a resistance variation of the resistive layers over the wafer. Principally this problem can be avoided by carrying out the implantation in two steps at opposite directions.

4.5 CONCLUSIONS

The existence of defects in position–sensitive detectors based on epilayers is characterized by the wide spread of resistance values of the p–type resistive layers over the whole wafer, and more typically by the ohmic connection between the top p–type layer and the substrate. The following aspects can be summarized for the operation and the testing of this type of PSD: (a) PSD's based on epilayers should be operated with the junction between the epilayer and the substrate reverse biased. (b) Besides the leakage current and the resistance distribution of the resistive layers, the current–voltage characteristic between the p–type layer and the substrate can be used as one of the criteria for qualifying PSD's. This kind of defect can be discovered in an early stage when the current–voltage characteristic shows an ohmic character. (c) The influence of the defect on the position–response linearity decreases with the p–type layer to substrate resistance.

The angular position–sensitive detector has the following properties: (a) The photocurrents measured from the electrodes are linear functions of the angular position of the light spot. (b) The output currents remain constant when the light spot moves in the radial direction. (c) The APD measures the center of gravity of the current density across the junction. The APD is first designed with a ring–shaped resistive layer intercepted by four electrodes. The deviation in the measured values caused by the electrode increases with the size of the light spot. This problem is solved in the modified APD, in which two separate resistive layers are fabricated with each layer responsible for the measurement of 180 degrees.

For the application to the tilt sensor, the two–dimensional PSD and the APD theoretically provide measurement accuracies of the same order. The choice is mainly based on technical considerations. In general, the APD provides a better performance because it uses only one resistive layer which can be made by ion implantation. Secondly, since the active area of the two–dimensional PSD is much larger than that of the APD, the chance of having defects in the two–dimensional PSD's is much larger. The process technology of the APD is comparatively simple and straightforward. An advantage of the two–dimensional PSD over the APD might be that it provides the possibility of determining the center of the vial in a photo–electrical way and, therefore, the problem of concentricity is avoided.

References

[4.1] J. T. Wallmark, "A new semiconductor photocell using lateral photoeffect", Proc. IRE, Vol.45, pp.474–484, 1957.

[4.2] G. Lucovsky, "Photoeffects in nonuniformly irradiated p–n junctions", J. Appl. Phys., Vol.31, pp.1088–1095, 1960.

[4.3] D. A. Allen, "An analysis of the radiation tracking transducer", IRE Trans. on Electron Devices, Vol.ED–9, pp.411–416, 1962.

[4.4] L. K. Buzanova, A. M. Vasil'ev, A. Y. Gliberman and A. P. Landsman, "Photocells exhibiting the longitudinal photoeffect", Radio Eng. and Electron Phys., Vol.10, pp.109–116, 1965.

[4.5] W. P. Connors, "Lateral photodetector operating in the fully reverse–biased mode", IEEE Trans. on Electron Devices, Vol.ED–18, pp.591–596, 1971.

[4.6] H. J. Woltring, "Single– and dual–axis lateral photodetectors of rectangular shape", IEEE Trans. on Electron Devices, Vol.ED–22, pp.581–589, 1975.

[4.7] V. S. Vassilev, "The photoeffect in silicon planar positional photo–detectors with a high resistivity doped channel", Solid State Electron., Vol.20, pp.999–1001, 1977.

[4.8] D. J. W. Noorlag and S. Middelhoek, "Two–dimensional position–sensitive photodetector with high linearity made with standard IC–technology", IEE J. Solid–State and Electron Device, Vol.3, pp.75–82, 1979.

[4.9] D. J. W. Noorlag, "Quantitative analysis of effects causing nonlinear position response in position–sensitive photodetectors (PSD)", IEEE Tran. on Electron Devices, Vol.ED–28, pp.158–161, 1982.

[4.10] D. J. W. Noorlag, "Nonlinear position responses in position–sensitive photodetectors", Sensors & Actuators, Vol.3, pp.1–15, 1983.

[4.11] H. P. Siebert, "Optoelektronische Positionsdetektoren PSD: Vollig aufgelost...", Elektronik, no.13, pp.84–88, 1984.

[4.12] H. J. Woltring, "Measurement and control of human movement", Ph.D. Thesis, Catholic University of Nijmegen, Peters & Haarsma, Nymegen, 1977.

[4.13] L. E. Lindholm and G. P. Petersson, "Position–sensitive photodetectors with high linearity", Proc. Int. Electron Devices Meeting, Washington DC, pp.408–411, 1976.

[4.14] D. J. W. Noorlag, "Lateral–photoeffect position–sensitive detectors", Ph.D. Thesis, Delft University of Technology, Delft University Press, Delft, 1982.

[4.15] H. Yashiro, Y. Z. Xing and S. Middelhoek, "Influence of surface defects on the performance of Si position–sensitive detectors", Proc. 4th Int. Conference on Solid–State Sensors and Actuators, Tokyo, pp.423–426, 1987.

[4.16] Y. Z. Xing, "Substrate and defect influences on the position–response linearity of position–sensitive detectors", Proc. ESSDERC'88, Montpellier, pp.821–824, 1988.

[4.17] D. Allen, I. Weiman, and J. Winslow, "Radiation tracking transducer", IRE Trans. on Instrumentation, Vol.I–9, pp.336–341, 1960.

[4.18] B. O. Kelly, "Lateral–effect photodiodes", Laser Focus, Vol.12, pp.38–40, 1976.

[4.19] G. T. Reid, H. Messer and H. Stewart, "Optical sensors for position and displacement measurement", Proc. 7th Int. Conference on Automated Inspection and Product Control, Birmingham, pp.323–330, 1985.

[4.20] Y. Z. Xing and C. P. W. Boeder, "A new angular–position detector utilizing the lateral photoeffect in Si", Sensors & Actuators, Vol.7, pp.153–166, 1985.

[4.21] M. Stuivinga, Y. Z. Xing and C. P. W. Boeder, "Encoder disk using a PSD", Proc. 1985 Test+Transducer Conference, Wembley, Vol.2, pp.147–160, 1985.

[4.22] M. Stuivinga and Y. Z. Xing, "Development of a 12–bit angular encoder", Proc. Sensor and Actuator Sym., Enshede, pp.247–255, 1986.

[4.23] G. P. Petersson and L. E. Lindholm, "Position–sensitive detectors with high linearity", IEEE, J. Solid–State Circ., Vol.SC–13, pp.392–399, 1978.

[4.24] S. M. Sze, "Physics of semiconductor devices", 2nd edition, John Wiley & Sons, New York, 1981.

[4.25] R. E. Collin, "Field theory of guided waves", McGraw–Hill, New York, 1960.

CHAPTER 5 THE SIGNAL–PROCESSING UNIT

5.1 INTRODUCTION

In Chapter 4, it was shown that the output signals from the position–sensitive detector utilizing the lateral photoeffect contain not only information about the position of an incident light spot, but also a component which is proportional to the total generated photocurrent intensity. This component is unwanted but inherent to the principle of operation of the PSD. Variations in the photocurrent intensity can lead to measurement errors. In respect to the PSD, photocurrent variations can be caused by the presence of obstacles on the device surface such as dust and wires, and by an inhomogeneous spectral sensitivity. In respect to the light source, variations in the light intensity can occur due to fluctuations in the power supply, the temperature dependence of the irradiation and the limited lifetime of the light source. In the particular case of the tilt sensor, the light intensity can also vary along the track of the air bubble as the result of a nonuniform illumination of the vial. Therefore, in order to achieve a high accuracy the photocurrent dependent component must be removed from the output signal. This is usually accomplished by electronic means.

The conventional signal–processing circuit which is used for the suppression of the disadvantageous effect of the photocurrent is based on analog dividers. The one constructed by Noorlag [5.1] consisted of a current–current converter, a current mirror and an analog divider (for a p–type resistive layer). The current–current converter and the current mirror were built with operational amplifiers (opamps) and the analog divider was made of a couple of transistor pairs. In 1985, Erb [5.2, 5.3] presented a circuit configuration which could easily be interfaced to a microcomputer. The currents measured from the electrodes were compensated by a switching current source. The current from one of the electrodes controlled the current source by means of an integrating amplifier. The other controlled the duty cycle of the switch via a second integrator and a pulse duration modulator. The duty cycle of the binary switch–controlled signal was proportional to the position of the light spot. The amplifiers and the current switches were integrated on a single chip. In 1988, Goto and Kato [3.4] presented a circuit using switching capacitors. The output currents from the PSD were charged into two capacitors and then converted into voltages. The voltages were proportional to the time of charging and the output currents. Division was accomplished by converting the differential voltage between the two outputs into a binary number with the summation voltage of the outputs as a reference. The circuit had a nonlinearity of 0.1% for photocurrents larger than 1 μA.

In this research work, a feasibility study is made on the design and realization of an electronic circuit which can be integrated with a one–dimensional PSD by using a bipolar IC process. The signal–processing circuit should be able to provide an output signal which varies linearly with the light spot position on the PSD, and which is insensitive to the variation in the generated photocurrent. In this chapter, the configuration of the circuit is first presented and its functional aspects are discussed. The accuracy and stability of the circuit are analyzed. An angular position–sensitive detector is fabricated with the signal–process circuit on one chip. Experiments on the position–response linearity and the temperature stability of the circuit are carried out. Advantages and shortcomings of this circuit are discussed in the last section.

5.2 THE CIRCUIT USING JFET'S

In Chapter 4, it was shown that when a position–sensitive detector is operated with a voltage output, the voltage across the electrodes of the PSD depends on the

photocurrent in the device, the resistance of the resistive layer, and the resistors which are connected to the electrodes. Principally, if one of these resistors is made in such a way that it depends on the total photocurrent, compensation for the influence of the photocurrent variation in the output can be achieved.

5.2.1 Operation of the circuit

Figure 5.1 shows the principal circuit. The variable resistor is realized by employing a p–channel junction field–effect transistor (JFET) which operates in the linear region. The channel conductance of the JFET can be changed by changing the gate voltage. Due to the presence of the resistor R_0 at the drain of the JFET, the gate voltage now becomes a function of the photocurrent generated in the PSD, and so the channel conductance of the JFET. The leakage current in the PSD is assumed to be negligible. In operation, when the photocurrent decreases, the gate–to–drain voltage of the JFET increases and the channel conductance decreases. This compensates for the decrease in the output voltage caused by the decreasing photocurrent and, hence, a constant output voltage is obtained. The operation of the circuit is optimized with a proper adjustment of the voltage source V_B.

The performance of the signal–processing circuit depicted in Fig.5.1 depends greatly on the functional characteristics of the JFET. Basically, the channel conductance of the JFET is not a linear function of the gate voltage. It depends also on the drain–to–source voltage. Therefore, the position–response linearity of the circuit output will possibly be affected. Another problem is the large temperature dependence of the channel conductance of the JFET, which can cause temperature instability in the circuit output. These problems can be solved when the circuit is designed in a symmetric way, as shown in Fig.5.2. In this circuit a second, identical JFET is incorporated. The resistance values of the resistors R_p', R_g' and R_t' are equal to those of R_p, R_g and R_t. The total current in the PSD is amplified by the current–voltage converter built with the opamp *OP1* and the resistor R_g. Since the channel conductance of the JFET is only determined by the gate voltage, equal channel conductances are obtained in *J1* and *J2* when the outputs of *OP1* and *OP2* are fed to the input of the opamp *OP5* which controls the gate voltages of the JFET's. V_r is a reference voltage applied across the compensation resistor R_p'. It determines the maximum output of the circuit. The output voltage V_{out} is now given by:

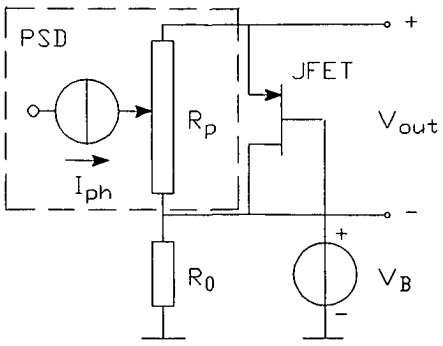

Fig.5.1 *The principal circuit using a JFET for the compensation for photocurrent variations.*

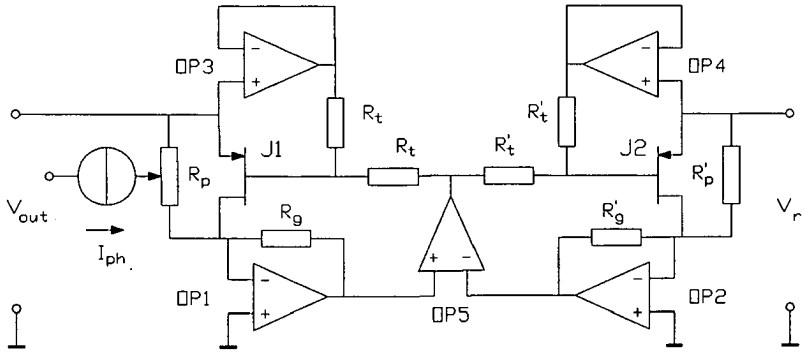

Fig.5.2 *The operational circuit.*

$$(5.1) \quad V_{out} = \frac{R_p I_{ph}}{1 + R_p G_{D_1}} \frac{x}{l}$$

in which I_{ph} is the total photocurrent, R_p the resistance of the resistive layer, x the position of the center of gravity of the light spot, and l the length of the resistive layer. G_{D_1} and G_{D_2} are the channel conductances of the JFET's *J1* and *J2*, respectively. In operation it holds $G_{D_1} = G_{D_2}$ and $G_{D_2} = I_{ph}/V_r - 1/R_p$. Substitute G_{D_2} into Eq.(5.1) we obtain:

$$(5.2) \qquad V_{out} = \frac{x}{l} V_r$$

The linearity of the drain current as a function of the source to drain voltage is improved when the source voltage of the JFET is coupled with the gate voltage [5.5]. This is done by means of the opamps *OP3* and *OP4* with the resistors R_t and R_t'. When the JFET's are well matched, the problem with the nonlinear relation between the channel conductance and the gate voltage is avoided and the influence of the large temperature coefficient of the channel conductance is suppressed.

The maximum tolerable variation in the total photocurrent I_{ph} is determined by the condition:

$$(5.3) \qquad \gamma_{GD} G_0 < G_D < G_0$$

in which G_0 is the maximum channel conductance of the JFET and γ_{GD} a constant factor. γ_{GD} determines the minimum channel conductance which can be obtained by varying the gate voltage without forcing the JFET into the subthreshold region [5.6, 5.7, 5.8]. It can experimentally be determined. The ratio between the minimum and the maximum of I_{ph} is then:

$$(5.4) \qquad \frac{I_{ph,min}}{I_{ph,max}} \approx \frac{1 + \gamma_{GD} R_p G_0}{1 + R_p G_0}$$

In order to achieve a large tolerable variation in the photocurrent, it is desired to have: $R_p G_0 >> 1$ and $\gamma_{GD} << 1$. The relation between the maximum photocurrent $I_{ph,max}$ and the reference voltage V_r with given values of the resistance of the resistive

layer R_p and the maximum channel conductance of the JFET G_0 is found to be:

$$V_r = \frac{R_p I_{ph,max}}{1 + R_p G_0} \tag{5.5}$$

5.2.2 The accuracy and stability

the accuracy

The accuracy of the signal–processing circuit is highly dependent on the symmetry of the circuit. Mismatchings between diverse components, such as the resistors, the JFET's and the opamps, are the main sources leading to an incomplete compensation for the photocurrent variation and an increase in the circuit inaccuracy. A couple of the error sources are analyzed as follows:

(a) The matching error between the resistive layer R_p and the compensation resistor R_p'. If the matching error is expressed as: $\delta_R = (R_p - R_p')/R_p$, the variation in the output voltage as the result of a change in the photocurrent $\delta_I = \delta I_{ph}/I_{ph}$ is calculated as: $(V_r/I_{ph}R_p)\delta_I\delta_R$.

(b) The pinchoff voltages of the JFET's J_1 and J_2 differ from each other. Suppose the difference in the pinchoff voltages can be expressed as: $\delta_p = \Delta V_p/V_p$, the variation in the output voltage as the result of a change in the photocurrent is calculated as: $(G_0 V_r/I_{ph})\delta_I\delta_P$.

(c) Unequal bias currents in the opamps: $\delta_{I_{bias}} = (I_{bias1} - I_{bias2})/I_{ph}$, will result in a output voltage change: $\delta_{I_{bias}}\delta_I$. Unequal offset voltages in the opamps will result in a change of the sensitivity of the circuit.

(d) Inaccuracy in the feedback resistors R_g and R_g'. The output voltage is then: $V_{out} = (R_g'x/R_gl)V_r$, which shows that a mismatching between the two resistors causes a change in the circuit sensitivity.

From the above equations we can see that large values of the total photocurrent I_{ph} and the resistance of the resistive layer R_p, as well as small values of the reference voltage V_r and the maximum channel conductance G_0 lead to a high circuit accuracy. The photocurrent in the PSD is mainly determined by the optical power of the light source, the size of the air bubble and the spectral sensitivity of the PSD. The resistance of the resistive layer is determined by the geometry of the PSD and the fabrication process. Changing the geometry of the PSD can increase the resistance of

the resistive layer, but the position–response nonlinearity caused by the variation in the resistive layer thickness will also increase, as previously evaluated. A large resistive layer also means a large source impedance for the voltage amplifier, which increases the signal transfer error. On the other hand, the values of G_0 and V_r cannot be made too small, since the compensation range is also dependent on G_0 and for a small value of V_r, drift in the opamps will increase their influence on the circuit accuracy. Therefore, in the practical design, compromises must be made.

the stability

In the analysis of the circuit stability, the right–hand half of the circuit is considered as a voltage amplifier built with the opamp *OP5* in combination with a feedback circuit consisting of *J2* and *OP2*. The feedback circuit functions also like a voltage amplifier. In the feedback circuit, since the source impedance is very small within the frequency range of interest, the JFET *J2* can be interpreted with an unilateralised equivalent scheme. If C_t is the total parasitic capacitance in the JFET, the feedback fraction β_t of the feedback loop is given by:

$$\beta_t = \frac{g_m R_g'}{2(1 + s/p_1)(1 + s/p_2)} \tag{5.6}$$

where g_m the transconductance of the JFET, $p_1 = 2/C_t R_t'$ and $p_2 = p_c/(1 + G_0 R_g')$. p_c is the unit gain corner of the opamp. The feedback factor of the system is:

$$F(s) = A_{OP}\beta_t = \frac{g_m R_g' A_0}{2(1 + s/p_1)(1 + s/p_2)(1 + s/p_3)} \tag{5.6}$$

in which A_{OP} and A_0 are the open–loop gain and the maximum open–loop gain of the opamp, respectively, and $p_3 = p_c/A_0$. By using the Routh–Hurwitz criterion [5.9], it can be shown that, in order to obtain a stable system, it must be satisfied that $g_m R_g' < 2p_1/p_c$, with the assumption that $p_1 >> p_2 >> p_3$. The open–loop gains of the opamps are assumed to be equal. Given the values: $f_c = 100$ kHz, $C_t = 40$ pF, $R_t' = 10$ kΩ, we obtain $g_m R_g' < 16$. By using the equation $g_m = G_0 V_D / V_P$ it can be shown that R_g' must be smaller than 800 kΩ with $G_0 = 0.2$ mS, $V_D = 0.1$ V and $V_P = 1$ V.

5.3 EXPERIMENTS

5.3.1 Fabrication of the chip

The electronic signal–processing circuit is integrated with the angular position–sensitive detector on the same chip. The standard TUD–06 process [5.10] is used. The sheet resistivity of the resistive layer has a value of 1 kΩ. The leakage current of the outer ring has a typical value of 2.1 nA at room temperature for a reverse–bias voltage of 3 V. This is larger than devices with the same configuration fabricated with the TUD–01 process, which, as a comparison, have a typical leakage current of 0.6 nA under the same measurement conditions. This may be attributed to the higher complexity of the TUD–06 process.

A photograph of the device is shown in Fig.5.3. At the two corners of the chip four pairs of JFET's are integrated with different values of the maximum channel conductance, while along the lower edge of the chip opamps are placed. The JFET's have a circular gate with an outer radius of 140 μm and an inner radius varying from 60 μm to 100 μm. During the operation the upper and the lower gates are connected, which gives a pinchoff voltage of approximately 0.9 V. Because of a process failure the lateral pnp–transistors in the opamps do not function properly. Therefore, the experimental circuit is built with the JFET's integrated with the APD, and with discrete components (opamps and resistors). The device parameters are given in Table 5.1.

Table 5.1 Specifications of the components used.

component	value/type
JFET	p–type V_P : 1 V G_0 : 0.17 – 1.4 mS
opamp	OP–07C
R_g and R_g'	100 kΩ
R_t and R_t'	10 kΩ
R_p and R_p'	inner ring : 21.7 kΩ outer ring : 28.3 kΩ

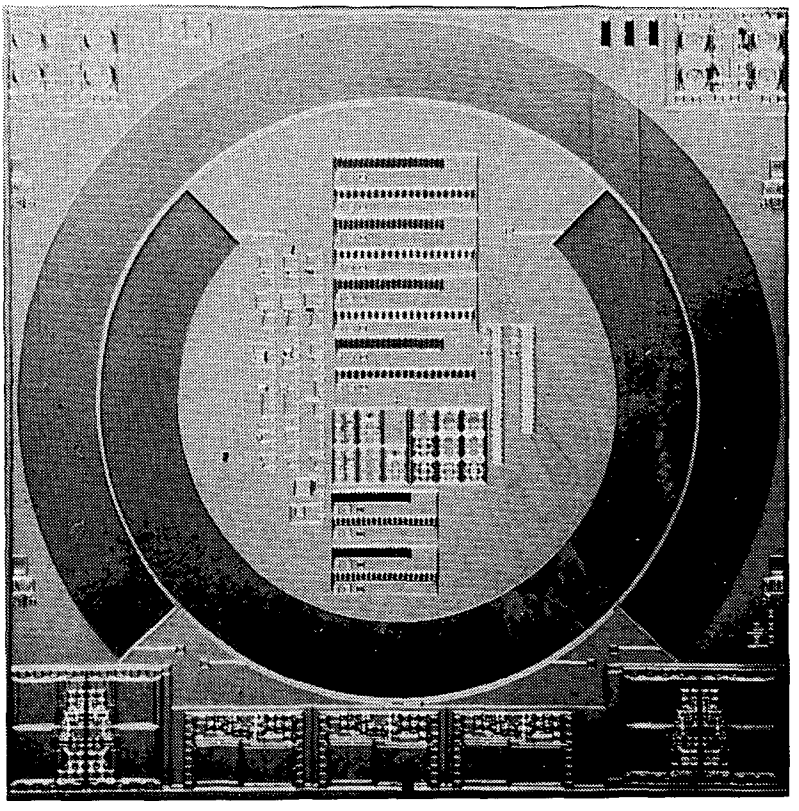

Fig.5.3 Photograph showing the angular position–sensitive detector with the integrated electronic signal–processing circuit.

5.3.2 Experimental results

The dependence of the output voltage as a function of the photocurrent is first investigated with the position of the light spot as a parameter. Experiments are carried out by measuring the output voltage while varying the light intensity. The measurement results are depicted in Fig.5.4, which show that the output voltages tend to be constant within ·0.15 % ·of the maximum output voltage with a photocurrent intensity decrease of 50 %. The nonlinearity of the drain–current–to–drain–voltage characteristic is also measured as a function of the gate voltage with a drain–to–source voltage of 0.2 V. As Fig.5.5 shows, the nonlinearity is smaller than 0.08 % of the total measurement range when the gate voltage is smaller than the pinchoff voltage. The parameter γ_{GD} defined in Eq.(5.3) is thus calculated as 0.2.

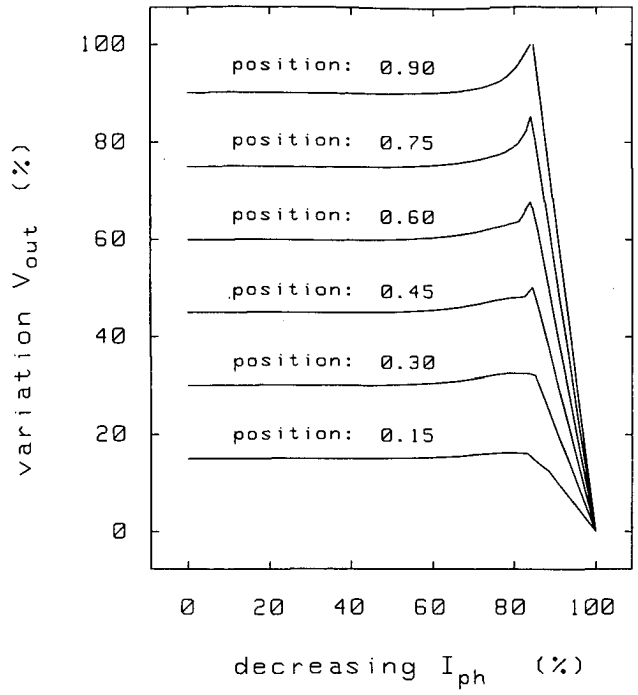

Fig.5.4 *The output voltage V_{out} measured with a decreasing total photocurrent intensity I_{ph} with the light spot position (normalized) as a parameter. $V_r = 100\ mV$; $I_{ph,max} = 31\ \mu A$.*

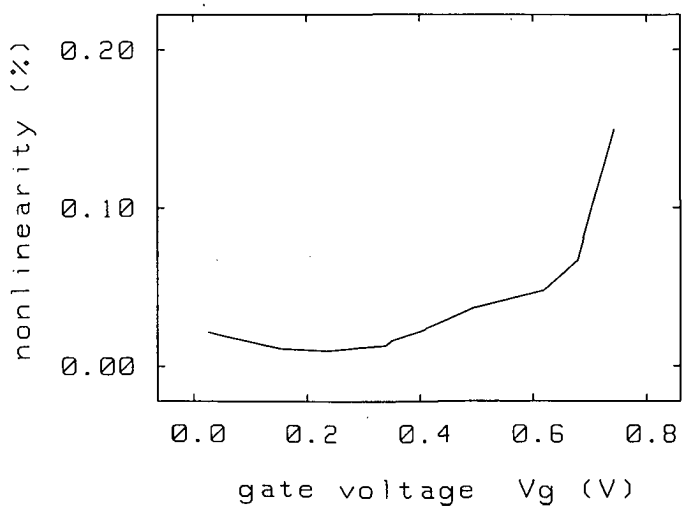

Fig.5.5 *Nonlinearity in the drain–current–to–drain–voltage characteristic as a function of the gate voltage. $V_p = 0.9\ V$; $V_d = 0.2\ V$.*

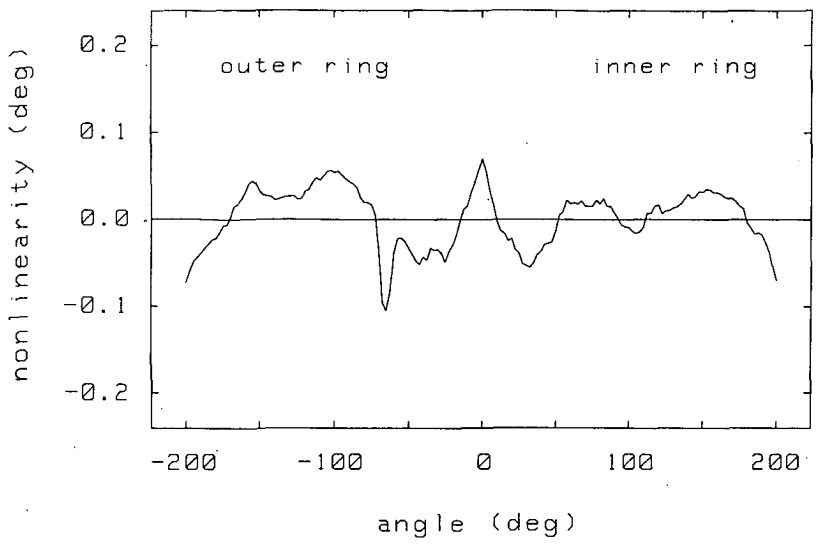

Fig.5.6 *Position–response nonlinearity of the angular position–sensitive detector with its output signal processed by the circuit using JFET's.* $I_{ph} = 25\ \mu A$; $V_r = 100\ mV$.

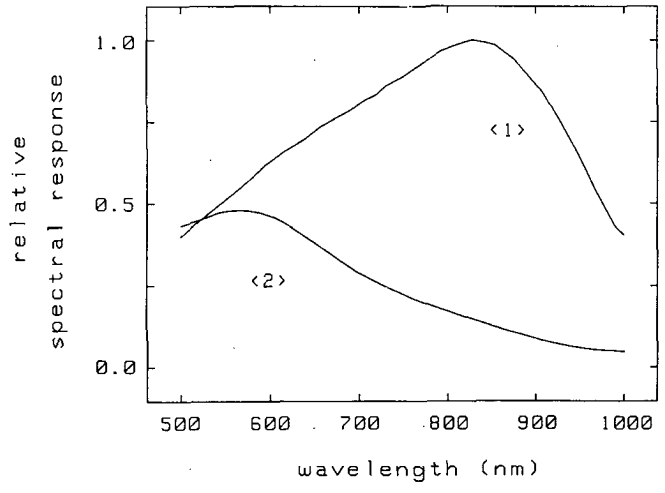

Fig.5.7 *Relative spectral responses of the APD's. Measurements were taken on the outer resistive layer of the device.*
<1> APD fabricated with the modified TUD–01 process.
<2> APD fabricated with the standard TUD–06 process.

The position–response linearity of the APD is measured. The output of the APD is processed by the signal–processing circuit. The JFET's on the same chip as the APD are used in the electronic circuit. As Fig.5.6 shows, the linearity with respect to the best straight line is within than ± 0.1 degree in the mean measurement region. Measurements are also carried out on the relative spectral response of APD's fabricated with the modified TUD–01 process and the standard TUD–06 process. The measurement setup is composed of a monochromator with a halogen light source and a reference photodetector (HUV series, EG&G). The measurement results are shown in Fig.5.7. During the measurement no bias voltage is applied. For the APD fabricated with the TUD–06 process, the epilayer and the substrate are connected together. The considerable lower spectral sensitivity of the APD made with the TUD–06 process in the infrared region is attributable to the three–layer structure of the device. The hole–electron pairs generated in the junction between the epilayer and the substrate are evidently lost. Improvements can be made in many aspects. First, there is the thickness of the epilayer which is only 4 μm in the standard process. Increasing the epilayer thickness will enhance the spectral response of the APD in the infrared region. Secondly, the possibility of using the epilayer as the resistive layer can be considered. As the APD now has a two–layer structure, the generated hole–electron pairs in the substrate can also be collected and the total photocurrent can be increased. It can be expected that devices with this structure may even have a higher spectral response in the infrared region, as the depletion layer in this case lies much deeper in the substrate. The problem with the relatively lower homogeneity of the epilayer can be solved when an n–type ion implantation on top of the epilayer is introduced. This n–type implanted resistive layer will then essentially determine the linearity of the APD.

The temperature stability of the circuit, and that of the circuit with the APD, have been examined. During the measurement of the temperature dependence of the circuit, the APD is replaced by a resistor and a current source. Measurement results show that the output voltage of the circuit has a temperature coefficient of 0.001 %/^{0}C of the maximum output voltage over a temperature range from 20 ^{0}C to 80 ^{0}C. The temperature dependence of the circuit with the APD is rather large, about 0.2 %/^{0}C over the same temperature range. This is attributed to the large temperature dependence of the resistivity of the resistive layer. Measurement results show that the resistance of the resistive layer has a 10 % increase as the ambient temperature changes from 20 ^{0}C to 80 ^{0}C. Compensation for this temperature dependence in present stage is difficult as the resistive layer and the discrete resistor do not have the same temperature coefficient.

5.4 CONCLUSIONS

An electronic signal–processing circuit using JFET's for the compensation for the influence of photocurrent variations in the APD has been realized. The circuit has been integrated with the APD on one chip with a bipolar IC process. It provides an output voltage which is a linear function of the light spot position on the APD, and which is insensitive to the photocurrent variation within a certain range. The experimental circuit shows a high linearity and a good temperature stability. The main error source is thought to be the mismatching between the resistance values of the resistive layer and the compensation resistor. This causes also a large temperature dependence of the circuit output. The problem will probably be solved when the resistive layer and the compensation resistor are fabricated on the same chip. The circuit has a compensation range for the photocurrent variation of approximately 50 % of the maximum photocurrent. In practice, the compensation range may possibly be sufficient when the angular position–sensitive detector is incorporated in the tilt sensor and the initial value of the total photocurrent intensity is known. The angular position–sensitive detector fabricated with the TUD–06 process provides a position–response linearity comparable with the device fabricated with the TUD–01 process. Since no optimization techniques have been applied in the current design, the APD has a considerably poorer spectral response in the infrared region. Improvements can be made in the structure of the APD and further research work is still required.

References

[5.1] D. J. W. Noorlag, "Lateral–photoeffect position–sensitive detectors", Ph.D. Thesis, Delft University of Technology, Delft University Press, Delft, 1982.

[5.2] K. J. Erb, "High resolution optical position sensor with integrated signal processing", Proc. 3rd Int. Conference on Solid–State Sensors and Actuators, Philadelphia, pp.57–59, 1985.

[5.3] K. J. Erb, "Hochauflosender optischer Positionssensor mit integrierter Signalverarbeitung", Bull. SEV/VSE, Vol.76, no.9, pp.268–271, 1985.

[5.4] M. Goto, S. Kato, "On the differential operation circuit based on the switched capacitor circuit", Proc. IEEE Int. Sym. on Circuits. and Systems, Helsinki, pp.2229–2232, 1988.

[5.5] H. P. von Ow, "Reducing distortion in controlled attenuators using FET", Proc. IEEE, Vol.56, pp.1718–1710, 1988.

[5.6] R. J. Brewer, "The 'barrier mode' behavior of a junction FET at low drain currents", Solid–State Electronics, Vol.18, pp.1013–1017, 1975.

[5.7] W. M. C. Sansen and C. J. M. Das, "A simple model of ion–implanted JFET's valid in both the quadratic and the subthreshold regions", IEEE J. Solid–State Circuits, Vol.SC–17, pp.658–666, 1982.

[5.8] Y. Z. Xing and W. J. Lian, "A novel integrated optical potentiometer", Proc. 4th Int. Conference on Solid–State Sensors and Actuators, Tokyo, pp.427–430, 1987.

[5.9] R. C. Dorf, "Modern control systems", Addison–Wesley Publishing Company, Inc., London, 1980.

[5.10] L. K. Nanver, "High–performance BIFET process for analog integrated circuits", Ph.D. Thesis, Delft University of Technology, Delft University Press, Delft, 1987.

CHAPTER 6 EXPERIMENTAL RESULTS

An electronic spirit level tilt sensor capable of operating over a 360–degree measurement range has been manufactured. As a prototype device, the mechanism of the sensor has been constructed in such a way that the sensor principle and performance can be examined. In this chapter the construction of the vial and the tilt sensor are first presented. Experimental setups, which have been used in the measurement of the dynamic response of the tilt sensor and in the measurement of the position–response linearity of the position–sensitive detector, are described. Measurement errors are evaluated. Measurement results on the position–response linearity and the temperature stability of the sensor are presented.

6.1 CONSTRUCTION OF THE SENSOR

The vial is constructed of glass and PVC plates, as shown in Fig.6.1. The plates A, B and D are made of transparent glass while the plate C is made of black PVC. The dimensions of the plates are 20 mm × 20 mm. The thickness of the plates A, B and D is 1 mm, and of the plate C 5 mm. A cylindrical hole is made in the central plate C

with a diameter of 10 mm. The vial is first fabricated with the plates *B*, *C* and *D*. The opaque working liquid is then introduced into the vial through a small hole (diameter 1 mm) in the center of the plate *B*. The hole is then sealed off with the plate *A*. The adhesive used for gluing the plates is MOR–AD X 980 A/B.

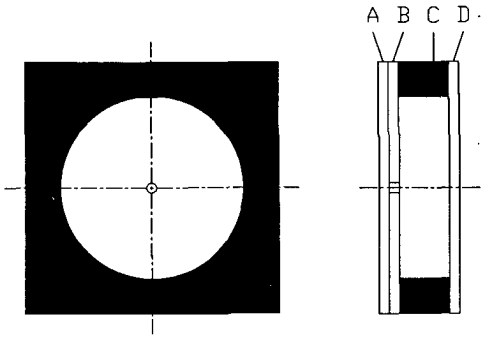

Fig.6.1 Structure of the vial.

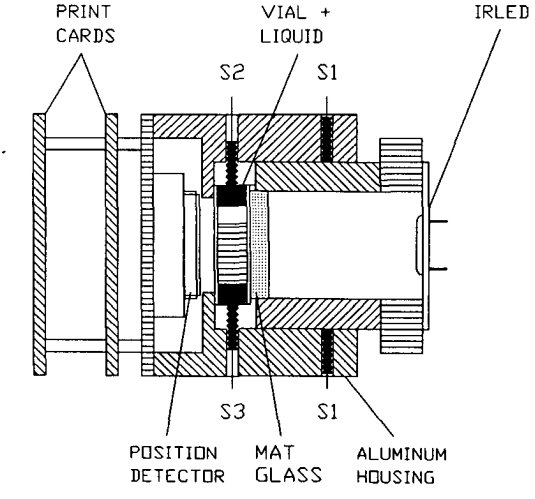

Fig.6.2 Structure of the tilt sensor.

The structure of the tilt sensor is shown in Fig.6.2. The form of the device is cylindrical. The aluminum case, in which the light source is mounted, has a length of 21 mm, an inner diameter of 20 mm and an outer diameter of 34 mm. The light source, which is an IRLED, is placed at one end of the case and at the other end a semi–transparent mat glass plate is mounted for the purpose of light diffusion. The housing, which holds the vial and the APD, is also made of aluminum. It has a length of 50 mm and a diameter of 60 mm. The case of the light source can be plugged into and removed from the housing when desired. The light source is fixed by the screw *S1*. The vial is secured by the screw *S2* and the spring *S3*, which also provide the possibility of moving the vial in two directions parallel with the APD. The bottom plate with the IC package can be dismantled from the housing to mount the APD. Two print cards are provided at the end of the housing for the electrical signal–processing unit. A photograph showing the tilt sensor, the vial and the mounted APD is presented in Fig.6.3.

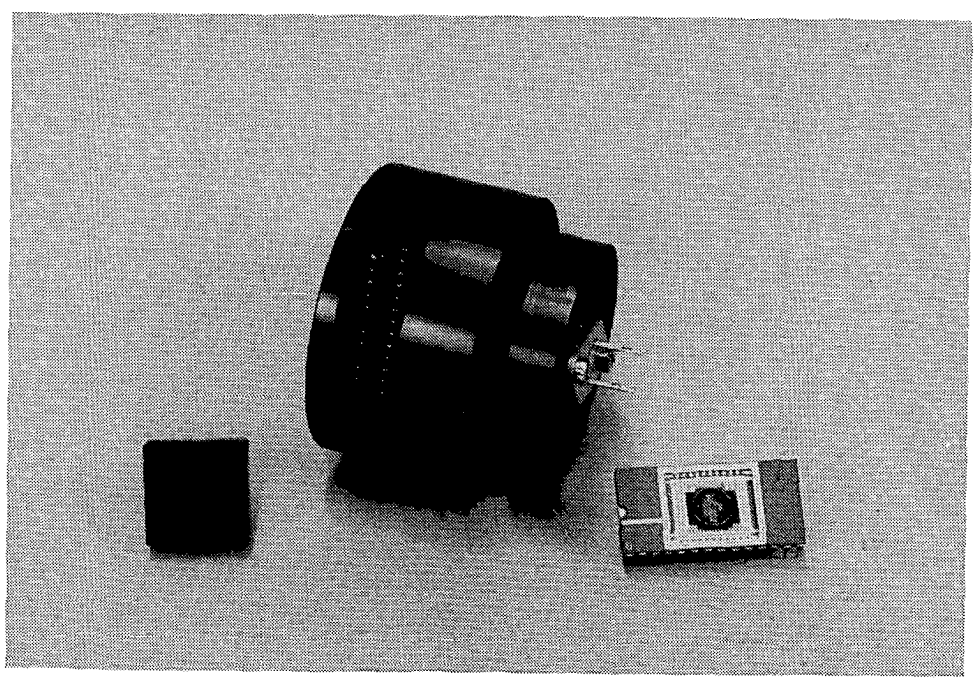

Fig.6.3 Photograph showing the tilt sensor, the vial and the mounted APD.

6.2 EXPERIMENTAL SETUP AND PROCEDURE

6.2.1 Measurement of the dynamic response

mechanism generating input signals

In order to measure the dynamic response of the tilt sensor, equipment is required which is capable of making various kinds of motion as the input signals for the sensor. These are an oscillatory tilt around the center of the sensor, an oscillatory displacement in the horizontal direction, and abrupt changes in the tilt as well as in the horizontal position (step functions). In the first two measurements it must be possible to vary the oscillation frequency from nearly DC to tens of hertz. In the step response measurement, the change of the sensor position must be carried out within a time interval which is shorter than the oscillation period of the sensor. After the device arrives in its end position, the mechanical vibration of the tilt sensor around its new position must be kept at an acceptable low level.

Figure 6.4 shows the mechanism used for the measurement of the frequency response with a tilt and a horizontal displacement as the inputs. It consists essentially of a DC motor (12 V maximum operational voltage), a platform on which the sensor is mounted and a steel rod which transmits the power developed by the motor to the platform. The moving parts are supported by the motor and two metal brackets on the side of the platform. There are open grooves in the steel rod and the brackets, in which the axes of the motor and the platform can move freely. The rotational motion of the motor is converted by the grooves into an oscillatory tilt or an oscillatory displacement motion on the side of the platform. The kind of motion which is carried out by the platform is determined by the metal blocks which can be mounted on and dismounted from the brackets and the rod. When the metal blocks are mounted on the brackets and the block on the rod is removed, the motion of the platform can be described by: $\theta(t) \approx R/l sin\ \omega t$ with $R << l$, where $\theta(t)$ is the tilt angle as a function of time, ω the angular velocity of the motor, l the length of the rod and R the length of the motor's rotating arm. For the frequency response measurement with a tilt input, R is 4 mm and l is 200 mm, which give a maximum swing of a tilt of about 2.3 degrees.

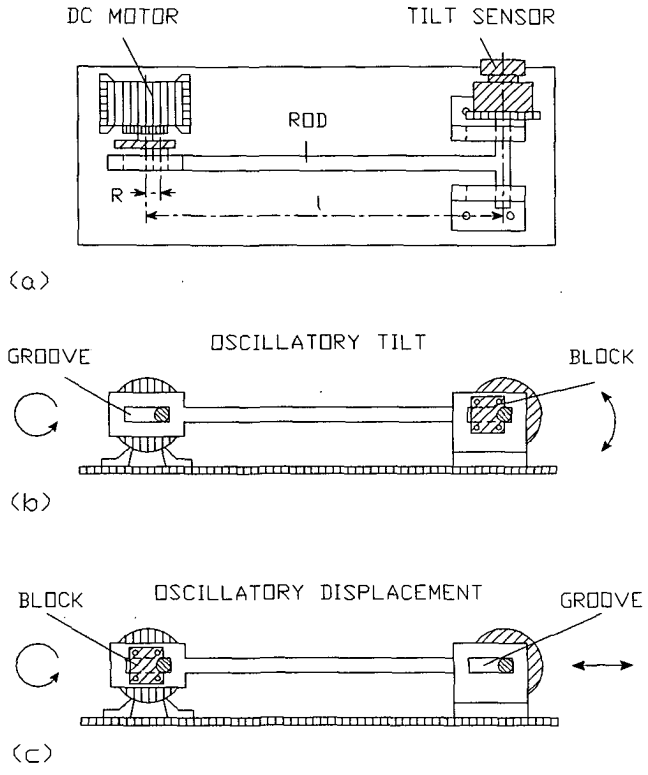

Fig.6.4 *Mechanism used in the frequency response measurement. (a) The top view. (b) The mechanism is prepared with a tilt as the input signal. (c) The mechanism is prepared with a horizontal displacement as the input signal.*

An oscillatory displacement in the horizontal direction is obtained when the block is mounted on the rod and the blocks are removed from the brackets. The motion of the platform can now be described by: $d(t) = R\cos \omega t$, in which $d(t)$ is the displacement of the platform from the center point of the groove. In this case $R = 0.5$ mm. The whole of the equipment is mounted on a heavy metal base in order to reduce harmonic oscillations at higher rotation frequencies of the motor. In the practical implementation a flywheel is mounted on the axis of the motor to increase the stability of the motion. It is omitted in the figure.

During the measurement the oscillation frequency is changed by varying the DC voltage to the motor. The voltage is derived from a programmable DC power supply. A low pass filter with a cutoff frequency of 200 Hz is placed behind the signal–processing unit to suppress noise in the higher frequency range. The output signal is recorded by a Biomation digital waveform recorder in combination with an oscilloscope. The amplitude of the output signal is then measured. Since we are only interested in the relative change of the amplitude as a function of the frequency, the true *rms* of the output signal can also be measured by means of an HP multimeter. In order to determine the rotation frequency of the motor, a miniature lamp and a photodiode are placed on either side of the rod. The light received by the photodiode is chopped by a thin metal plate mounted on the rod. The output current from the photodiode is amplified by a current–voltage converter and finally measured by the multimeter. Through HP–IB buses, the power supply and the multimeter are connected with an HP–310 computer, which determines the DC voltage on the motor and the times at which the rotation frequency and the output voltage are measured. It also acquires data from the multimeter and stores them on a hard disk. The measurement setup is schematically illustrated in Fig.6.5.

A step function of the tilt position is obtained by placing the steel rod between two magnetic coils. The coils can alternately be excited and released by changing the voltage of the power supply. The DC motor is removed from the setup. As shown in Fig.6.6, before the measurement starts, the rod is held in the upper position by exciting the upper magnetic coil while releasing the lower coil. An abrupt change of the rod from the upper position to the lower position is accomplished when the lower magnetic coil is excited on the release of the upper coil. The output from the low pass filter is sent to the waveform recorder. The step response of the tilt sensor is seen on the oscilloscope. The step input of the tilt is 3 degrees while that of the horizontal displacement is 0.5 mm.

measurement procedure and possible error sources

In the frequency response measurement, measurement errors can be caused by various sources:

(a) Resonant vibration of the mechanism. The amplitude of the vibration increases with the frequency. This is mainly due to the deformation of the axis of the DC motor at high rotation frequencies.

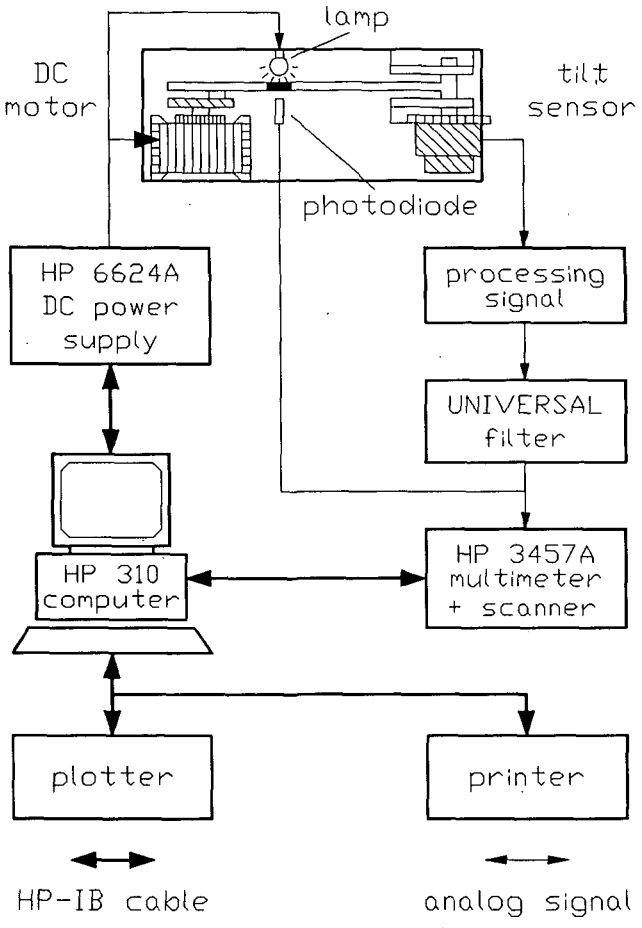

Fig.6.5 Setup used in the measurement of the dynamic response of the tilt sensor.

(b) During the measurement of tilt, an interferential horizontal displacement input occurs when the axis of the sensor is not concentric with that of the rotating platform. Its influence is small when $d_a\omega^2/g < 1$, where d_a is the misalignment between the two axes.

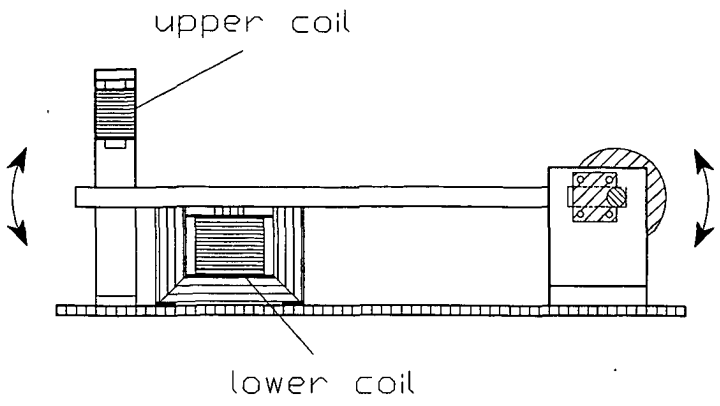

Fig.6.6 Mechanism used for the step response measurement of the tilt sensor.

(c) During the measurement of horizontal displacement, an interferential tilt input occurs as the result of the construction of the mechanism. It has a significant influence only for angular velocities with $\omega^2 < g/l$.

(d) Measurement error in the multimeter at frequencies lower than 10 Hz. This error can greatly be reduced by calibration.

(e) Drift in the angular velocity of the DC motor.

The multimeter is calibrated by using a counter and an oscillator. The measurement setup is tested before being used in the experiments. The test is carried out by removing the vial and the light source from the sensor housing and sending a laser beam to the APD. The rotation frequency varies from 2 Hz to 40 Hz. The measurement result is shown in Fig.6.7. The decrease in the output signal at low frequencies is caused by the decreasing sensitivity of the multimeter.

In the measurement of the transient response to a step input, possible errors are:

(a) An interferential displacement input during the measurement of tilt because of the misalignment of the axes. The result has been evaluated in Chapter 3.

(b) Vibrations in the mechanism after the rod arrives in the end position.

(c) A finite time interval in which the sensor moves from the starting position to the end position.

The latter two aspects can be reexamined by replacing the vial and the light source by a laser beam. The measurement result is shown in Fig.6.8, where we can see that the amplitude of vibration is at an acceptably low level, and that the rise time of the rod is much shorter than the oscillation period of the tilt sensor.

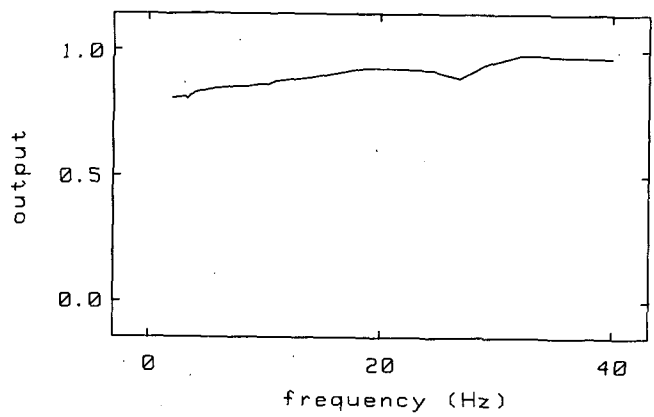

Fig.6.7 *Test result of the setup used in the frequency response measurement.*

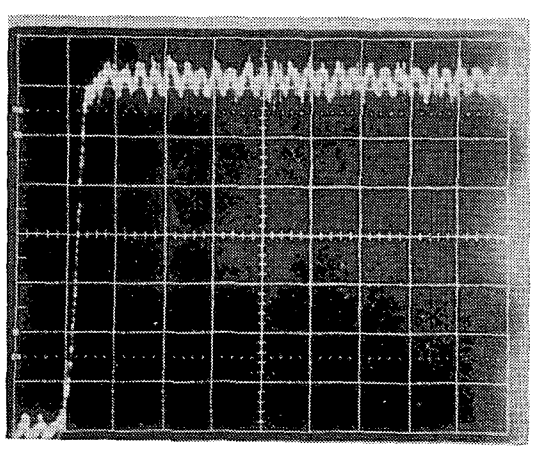

Fig.6.8 *Test result of the setup used in the transient response measurement to a step tilt input. x–axis*: 40 *ms/div. y–axis*: 20 *mV/div.*

6.2.2 Measurement of the position response

measurement setup

For the measurement of the position response of the two–dimensional PSD and the APD, computer controlled moving tables are used. As shown in Fig.6.9, the positioning of the PSD in the x–direction and the y–direction with respect to the light beam is accomplished by two translation tables, the x–table and the y–table. A rotational movement of the device is obtained by means of a rotation table, the w–table, which is stationed under the translation tables. During the measurement of the position response of the two–dimensional PSD, the w–table is unused. During the measurement of the APD, the sensor is centered with respect to the w–table by means of the x–table and the y–table. The manually controlled m–table aligns the light beam on the sensitive area of the APD in the radial direction. The light beam is derived from a 10 mW He–Ne laser. The light intensity received by the sensor can be varied by a polarizer placed in front of the laser. The beam is projected onto the device through a microscope and the size of the light spot can be changed by properly adjusting the vertical position of the microscope. In order to reduce seismic vibrations, the whole of the equipment is placed on a heavy metal base which is supported at three points by shock dampers.

In the measurement of the two–dimensional PSD, the electronic signal–processing circuit described in [5.1] is used. The outputs from the circuit are measured by an HP multimeter or sent to an x–y recorder. In the measurement of the angular position–sensitive detector, the output currents are first processed by current–voltage converters and then measured by the multimeter. The multimeter is adjusted to an integration time of 0.02 s. The HP–310 computer controls the position of the moving tables, determines the time at which measurement samples are taken and acquires data from the multimeter. The situation is depicted in Fig.6.10. During the testing of the tilt sensor, the device is placed on a rotation table of the same kind as the w–table. The rotation table is placed in a vertical position. The output currents from the APD in the tilt sensor are amplified by current–voltage converters. The output voltages are measured by the multimeter. The data are then sent to the computer.

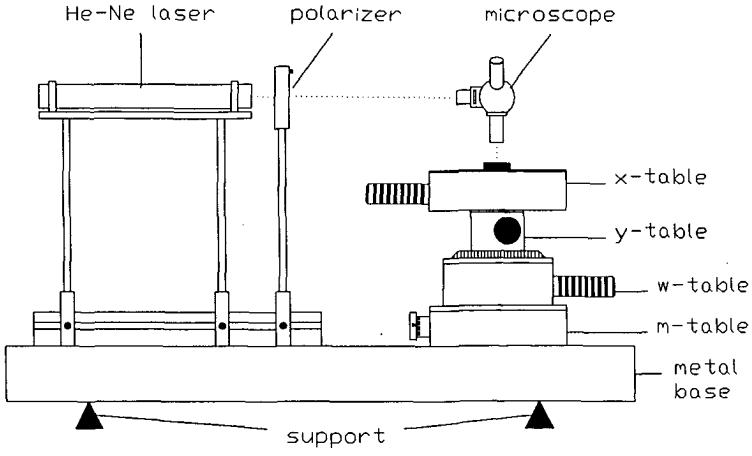

Fig.6.9 *Equipment used for the position–response measurement of the position–sensitive detectors.*

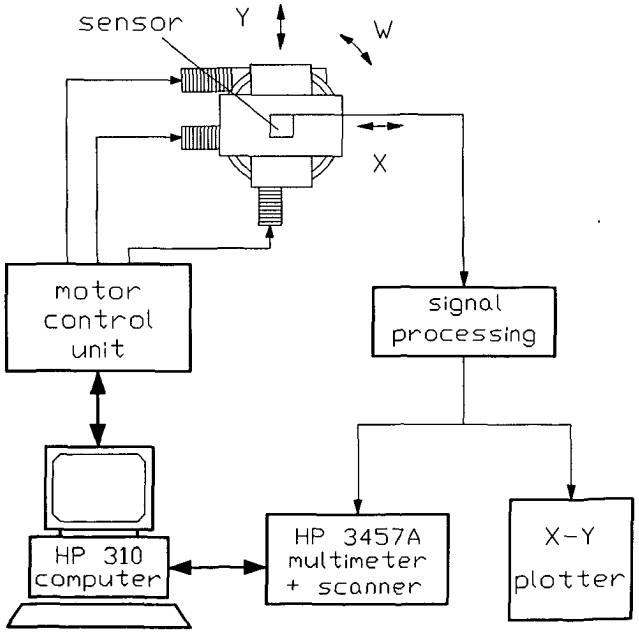

Fig.6.10 *Setup used in the position–response measurement of PSD's and APD's.*

measurement accuracy

The measurement accuracy is partly determined by the moving tables. The translation tables, the x–table and the y–table, have a step resolution of 1 μm, while the rotation table, the w–table, has a step resolution of 0.01 degrees. During the position–response measurement of the two–dimensional PSD, a small change in the form of the grid may occur when the two tables are not perfectly aligned in the orthogonal position.

A more significant measurement error occurs as the result of alignment inaccuracy. During the measurement of the APD, a misalignment can occur between the center of the rotation table and that of the device. The tilt sensor gives also a measurement error when a misalignment occurs between the axis of the cylindrical hole of the vial and the center of the APD. The misalignment causes a systematic error in the output. Referring to Fig.6.11, if O is the center of the APD, O' that of the track of the light spot, d the misalignment between the centers, R the radius of the track, ϕ' the angular position of the light spot and ϕ the angle measured by the APD, then the measurement error: $\Delta\phi = \phi - \phi'$ is calculated as: $\Delta\phi \approx d/R\ sin(\phi + \phi_0)$, for $d << R$. This shows that the concentricity error has a sinusoidal character with an amplitude of d/R and a period of 2π. The maximum error $\Delta\phi$ appears at the position $\phi = (n + 1/2)\pi - \phi_0$ with $n = 0, 1, 2 \ldots$ and $\Delta\phi_{max} = d/R$.

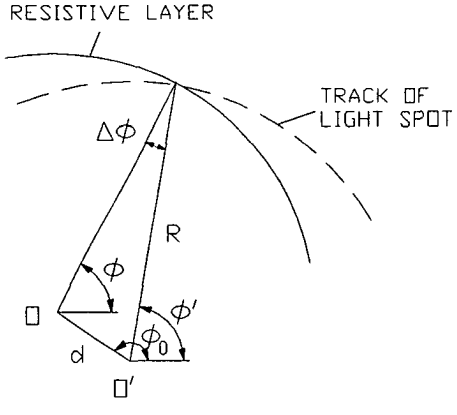

Fig.6.11
Concentric error in the measurement of the position response of the APD and the tilt sensor.

6.3 MEASUREMENT RESULTS

The measurement results of the position–response linearity of the tilt sensor referred to the best straight line is presented in Fig.6.12. The device shows a position–response linearity higher than ± 0.4 degrees. Besides the concentric error between the vial and the APD, a slightly stained inner surface of the vial and a variation in the light density along the track of the air bubble are thought to be responsible for the position–response nonlinearity. During the gluing process of the vial, a small portion of the adhesive crept into the inner space of the vial as the result of the capillary effect. When the colored alcohol is introduced into the vial, the liquid has the tendency to gather around the place where the adhesive is present. This hinders an optimal light transmission through the air bubble and causes a nonuniform distribution of the light density within the light spot. The light density variation along the track of the air bubble can also be caused by the concentric error of the light source with respect to the vial. The measurement result is reproducible for the same vial.

The resolution of the tilt sensor is defined as the smallest change in the tilt position which can still be detected by the device. It is determined in practice by the noise level in the APD and the associated electronic signal–processing circuit. In the measurement of the resolution of the tilt sensor, the rotation table is rotated with an increment of 0.02 degrees and the HP multimeter is adjusted with an integration time of 0.02 s. A clear response in the output of the tilt sensor can be observed for each increment in the angular position of rotation table.

In the investigation of the temperature stability, the tilt sensor is put into a furnace. Figure 6.13 shows the sensor output as a function of temperature. The change in the sensor output is actually the result of the increasing leakage current in the APD, as shown in the same figure. The center of gravity of the leakage current density can be considered as being located at the center of the resistive layer. When the light spot is moved into a position above the center of the APD, the measured output increases with the leakage current; when the light spot is moved into a position below the center of the APD, the output decreases with the leakage current. Secondly, as the temperature increases, the working liquid changes also its physical properties. For ethanol an increasing temperature from 20 ^{0}C to 50 ^{0}C causes a decreasing surface

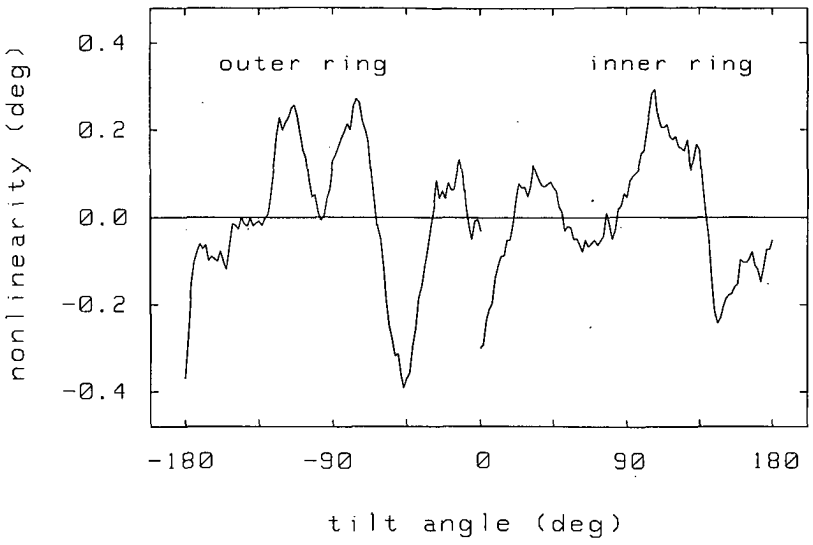

Fig.6.12 *Nonlinearity in the position response of the tilt sensor over a 360–degree range. Inner resistive layer: $I_{ph} = 0.9\ \mu A$, outer resistive layer: $I_{ph} = 1.6\ \mu A$*

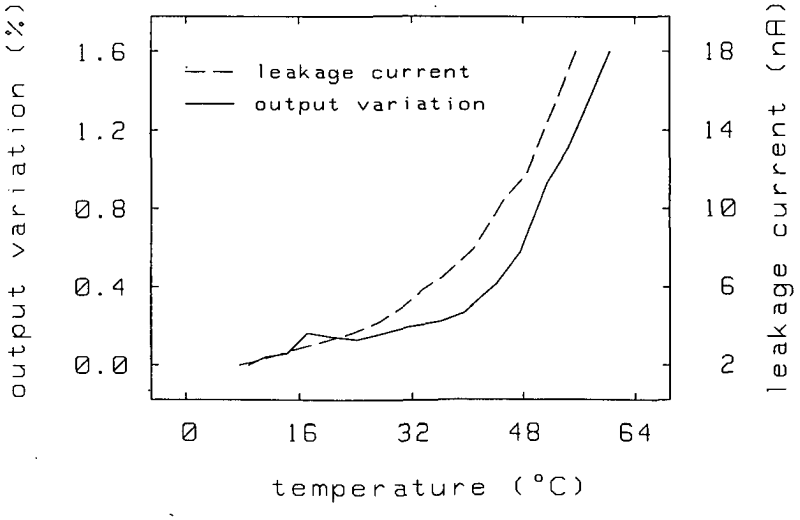

Fig.6.13 *Temperature dependence of the sensor output and the leakage current of the APD. Measurement was taken on the outer resistive layer. $I_{ph} = 1.6\ \mu A$ at room temperature.*

tension of approximately 13 %, which in turn causes a contraction in the height of the air bubble. Since the air bubble retains its symmetry during this process, no measurement error will occur. The irradiation efficiency of the IRLED shows a 30 % decrease as the temperature increases from 20 ^{0}C to 60 ^{0}C, which in turn causes a decrease in the photocurrent in the APD. An increased settling time with temperature can also be expected because of the decrease of the viscosity of the working liquid.

6.4 CONCLUSIONS

A summary of the performance of the prototype electronic spirit level tilt sensor is given in Table 6.1. One of the major sources of the position–response nonlinearity is believed to be the concentric error between the vial and the APD. This concentric error can be expected to be reduced when more advanced equipment is employed and the fabrication technique is improved. Improvements in the linearity of the tilt sensor can further be made in the construction of the vial, the adhesion technique and the liquid dye. Depending on the application it may sometimes be desired to change the settling time of the tilt sensor. This can be done by a proper adjustment of the size of the air bubble, or by changes in the viscosity of the alcohol by the addition of chemical substances. Precautions must be taken against the possible increase in the contact angle of the modified alcohol with the glass surface. The temperature stability of the tilt sensor can further be increased when the influence of the leakage current is diminished. On–chip compensation techniques and synchronous detection can be considered as subjects for further development.

Compared with the existing tilt sensor, the electronic spirit level tilt sensor shows certain distinguishing features. As no limitation is imposed on the number of rotations that the device can carry out during operation, new applications of the tilt sensor can possibly be exploited in the fields of position–control instruments and civil engineering. Without calibration the sensor provides a moderate linearity and temperature stability. It has no sliding noise and no undesired frictional drag force. The gravitation–orientation sensing unit of the sensor has a comparatively high temperature stability. These merits make the electronic spirit level tilt sensor, in some application areas, more advantageous than the pendulum based tilt sensors, which have been used so far in the large tilt angle measurement.

Table 6.1 Performance of the electronic spirit level tilt sensor

range	$n \times 360$ degrees
nonlinearity	± 0.4 degrees
hysteresis	0.02 degrees
resolution	0.02 degrees
natural frequency	7 Hz
damping ratio	0.2
settling time	0.45 s
drift	0.025 %/°C
diameter	60 mm
length	50 mm

SUMMARY

The primary aim of the research work presented in this thesis is to investigate the possibility of realizing an electronic tilt sensor which is small in size, suitable for mass production, and capable of operating over a 360–degree measurement range with a moderate linearity. An electronic tilt sensor consists of three basic units: the gravitation–orientation sensing unit, the position–sensing unit and the electronic signal–processing unit. The tilt sensor described in this thesis employs a gravitation–orientation sensing unit based on the spirit level principle. Compared with the pendulum based device, problems with mechanical friction associated with the pendulum mass are avoided in this liquid based sensor. The position of the air bubble is detected by means of an optical method, which yields the advantage of being a noncontact sensing method with a high linearity and a high resolution. In the design and realization of the signal–processing unit a study has been made on an electronic circuit which can be integrated with the position–sensing unit on one chip by using a bipolar IC process.

The gravitation–orientation sensing unit, which is the subject of Chapter 3, determines in many respects the performance of the tilt sensor. Alcohol is used as the working liquid because it has a zero contact angle with glass and a low surface–tension–to–mass–density ratio. This ensures a smooth motion of the air bubble. The liquid dye used for coloring the alcohol is Methasol Nigrosine which has a high absorption coefficient over a wide spectrum and a good solubility in alcohol. An IRLED is used as the light source because of its high irradiation power and low heat generation. Although no special measures are taken, the tilt sensor based on the spirit level principle exhibits a well–damped dynamic response. The dynamic property of the tilt sensor is, in the first place, dependent on the viscosity–to–mass–density ratio of the working liquid. The damping effect in the gravitation–orientation sensing unit increases with this ratio. Secondly, the damping effect is dependent on the size of the air bubble. A large bubble size results in a high natural frequency and a small damping ratio. Based on the rigid body assumption the tilt sensor can be described as

a second–order linear system. Frequency response and transient response analyses, therefore, can be used to describe the dynamic property of the tilt sensor.

In order to determine the position of the air bubble, an angular position–sensitive detector (APD) utilizing the lateral photoeffect in silicon is employed in the tilt sensor. The APD, which is described in Chapter 4, provides a high position resolution and a high position–response linearity. APD's which have a position–response linearity within ± 0.1 degrees were fabricated. In order to measure the position of a light spot over a 360–degree measurement range, two resistive layers are required to avoid problems with the electrodes. Compared with the two–dimensional bilateral position–sensitive detector (PSD), the APD has a higher position–response linearity and a higher production yield. The process technology is also comparatively simple and straightforward. However, when an on–chip electronic signal–processing circuit is required, attention must be paid to defects which may occur in the epilayer. The defects cause directional deformations in the position–response grid of the PSD. An effective method to discover this kind of defect in an early stage is to measure the current–voltage characteristic between the top p–type resistive layer and the p–type substrate. An ohmic characteristic usually implies the existence of the defect.

In Chapter 5, an electronic signal–processing circuit using JFET's is presented. It has a high linearity and a good temperature stability. The compensation range of the circuit for photocurrent variations is comparatively smaller than that obtained by using conventional techniques. Due to the presence of the epilayer, APD's fabricated with the TUD–06 process show a considerably lower spectral response in the infrared region than those fabricated with the TUD–01 process. Improvements can be expected when the thickness of the epilayer is increased, or when the epilayer, instead of the implanted layer, is used as the resistive layer in the APD.

In Chapter, 6 the experimental results of a prototype electronic spirit level tilt sensor are presented. The device has an operational range of $n \times 360$ degrees and a position–response linearity within ± 0.4 degrees. The natural frequency is 7 Hz and the damping ratio is 0.2. These give a settling time for the tilt sensor of 0.45 s.

SAMENVATTING

Het doel van het in dit proefschrift beschreven onderzoek is om een elektronische sensor te realiseren, waarmee hellingen gemeten kunnen worden. De sensor is klein van afmetingen, geschikt voor massaproduktie en maakt een meetbereik van 360 graden mogelijk. Een elektronische hellingssensor bestaat uit drie basiseenheden: een eenheid die gevoelig is voor de oriëntatie ten opzichte van het gravitatie veld, een eenheid die gevoelig is voor de positie van de in de eerste eenheid gebruikte massa en een eenheid voor de verwerking van elektronische signalen. De in dit proefschrift beschreven hellingssensor maakt gebruik van een gravitatie–oriëntatie gevoelige eenheid, die gebaseerd is op het waterpas principe. In vergelijking met een op een slinger gebaseerd instrument zijn de problemen, die verband houden met de mechanische wrijving tengevolge van de slingerbeweging, vermeden in deze op een vloeistof gebaseerde sensor. De positie van de luchtbel wordt langs een optische weg bepaald. Het voordeel hiervan is dat de positiegevoelige eenheid geen mechanisch kontakt maakt met het bewegende deel in de gravitatie–oriëntatie eenheid. Deze methode resulteert in een hoge lineariteit en een hoge resolutie. Bij het ontwerpen en realiseren van de signaalverwerkende eenheid is een studie gemaakt van een elektronische schakeling die samen met de positiegevoelige eenheid geïntegreerd kan worden op één chip met behulp van een bipolair IC proces.

De gravitatie–oriëntatie gevoelige eenheid, die het onderwerp is van hoofdstuk 3, bepaalt in vele opzichten de prestatie van de hellingssensor. Als werkvloeistof wordt alcohol gebruikt, omdat het oppervlak van deze vloeistof een hoek van nul graden maakt met de glaswand en omdat deze vloeistof een lage oppervlakte–spanning/massadichtheid verhouding heeft. Dit garandeert een soepele beweging van de luchtbel. De stof, waarmee de alcohol gekleurd wordt, is Methasol Nigrosine, dat een hoge absorptiekoëfficiënt heeft over een breed spektrum en goed oplosbaar is in alcohol. Als lichtbron wordt een IRLED gebruikt wegens zijn hoog stralingsvermogen en zijn geringe warmteproductie. Hoewel er geen speciale maatregelen genomen worden, vertoont de hellingssensor een goed gedempte dynamische respons. Het

dynamische gedrag van de hellingssensor is in de eerste plaats afhankelijk van de viskositeit/massadichtheid verhouding van de werkvloeistof. De demping neemt in de gravitatie–oriëntatie gevoelige eenheid toe met deze verhouding. Op de tweede plaats is de demping afhankelijk van de afmeting van de luchtbel. Een grote luchtbel resulteert in een hoge eigenfrequentie en een kleine dempingsverhouding. Gebaseerd op de "rigid–body" aanname, kan de hellingssensor beschreven worden als een tweede orde lineair systeem. De frequentierespons en transiëntrespons analyse kunnen dus worden gebruikt voor het beschrijven van het dynamische gedrag van de hellingssensor.

Om de positie van de luchtbel te kunnen bepalen, wordt in de hellingssensor een hoekpositiegevoelige detektor (APD) gebruikt, die gebaseerd is op het laterale fotoeffekt in silicium. De APD, die beschreven is in hoofdstuk 4, is gekenmerkt door een hoge positieresolutie en een hoge positierespons lineariteit. APD's met een lineariteit van ± 0.1 graad werden vervaardigd. Om de positie van een puntvormige lichtvlek over een 360 graden bereik te kunnen meten en de problemen te vermijden, die veroorzaakt worden door de kontaktelektroden, worden twee weerstandslagen gebruikt. In vergelijking met de tweedimensionale positiegevoelige detektor (PSD) heeft de APD een hoge positierespons lineariteit en een hoge produktieopbrengst. De procestechnologie is ook minder gekompliceerd. Wanneer naast een detektor ook een elektronische signaalverwerkende schakeling op dezelfde chip nodig is, moet aandacht worden besteed aan de defekten, die in de epilaag kunnen optreden. De defekten kunnen asymmetrische vervorming veroorzaken in het positierespons rooster van de APD. Om dit soort defekten in een vroeg stadium te kunnen ontdekken, is het meten van de stroom–spannings karakteristiek tussen de bovenste weerstandslaag en de substraatlaag een effektieve methode. Een weerstandskarakteristiek duidt meestal op de aanwezigheid van defekten.

In hoofdstuk 5 wordt een elektronische signaalverwerkende schakeling gepresenteerd, die gebaseerd is op JFET's. De schakeling heeft een hoge lineariteit en een goede temperatuurstabiliteit. Het kompensatiegebied voor fotostroomvariaties van deze schakeling is kleiner dan dat wat bereikt kan worden met konventionele technieken. Wegens de aanwezigheid van de epilaag, vertonen APD's, die gemaakt zijn met behulp van het TUD–06 proces, een lagere spektrale respons in het infrarode gebied dan die, die vervaardigd zijn met behulp van het TUD–01 proces. Een verbetering kan worden verwacht, indien de dikte van de epilaag wordt vergroot of wanneer de epilaag in plaats van de implantatielaag wordt gebruikt als de weerstandslaag van de APD.

In hoofdstuk 6 worden de experimentele resultaten besproken, die verkregen werden aan een prototype van de elektronische hellingssensor. Het apparaat heeft een werkbereik van 360 graden en een positierespons lineariteit van ± 0.4 graden. De eigenfrequentie is 7 Hz en de dempingsverhouding is 0.2. Deze geven een tijdsduur tot stilstand van 0.45 s voor deze sensor.

ACKNOWLEDGEMENT

The work presented in this thesis was performed in the Laboratory of Electronic Instrumentation, Faculty of Electrical Engineering, Delft University of Technology, Delft. The project is financially supported by the Dutch Technical Foundation (STW, project DEL46.0579) and administratively managed by the Dutch Foundation for Fundamental Research on Matter (FOM).

I would like to express my deepest appreciation and thankfulness to many of my colleagues and friends, in particular I would like to thank:

- Professor S. Middelhoek, my supervisor, for his guidance and helpful advice;
- Dr. M. Stuivinga, Mr. H. Yashiro, Dr.ir. D.J.W. Noorlag for their cooperation in the investigation, design and measurement of the position–sensitive detectors and the angular position–sensitive detectors;
- Dr.ir. J.H. Huijsing and Dr.ir. L.K. Nanver for their valuable advice with regard to the electronic circuit;
- members of the IC workshop: Mr. J. Groeneweg, Mr. W. Verveer, Mr. F.J. de Jong, Mr. W. de Koning, ir. J.M.G. Teven, and ir. P.K. Nauta, for the fabrication of my devices;
- Mr. F. Schneider for his technical assistance in the design and fabrication of the mechanical part of the sensor; Mr. P.J. Trimp, Mr. J.C. Staalenburg and drs. J.C. van den Heuvel for their assistance in the experiments at different stages;
- members of the workshop of the Faculty of Applied Physics and members of the workshop of the Faculty of Electrical Engineering for their skillful fabrication of the glass structures; drs. J.G. Neevel of the Faculty of Chemical Engineering and Mr. H. Frank of the Faculty of Biotechnology for their assistance in the selection and experiments with the liquid dye; Mr. G. van Dijk of the Faculty of Applied Physics for his help in the preparation of the vial;
- ir. J.C. Haartsen, ir. J.H. Visser, the members of the sensor group, and all the other members of the Laboratory of Electronic Instrumentation for their moral support and fruitful discussions during the four years research work;
- Mrs. J.B. Zaat–Jones, Mrs. S. Massotty and Mrs.J. Nuijen for their invaluable skill and patience in helping me to improve my English and correct all the spelling, grammar and syntax errors which I made in this thesis and in all my previous scientific papers and reports.

Publications and Representations Related to this Thesis

Y. Z. Xing and C. P. W. Boeder, "A new angular–position detector utilizing the lateral photoeffect in Si", Sensors & Actuators, Vol.7, pp.153–166, 1985.

M. Stuivinga, Y. Z. Xing and C. P. W. Boeder, "Encoder disk using a PSD", Proc. 1985 Test+Transducer Conference, Wembley, Vol.2, pp.147–160, 1985

M. Stuivinga and Y. Z. Xing, "Development of a 12–bit angular encoder", Proc. Sensors & actuators Sym., Enschede, pp.247–255, 1986.

H. Yashiro, Y. Z. Xing and S. Middelhoek, "Influence of surface defects on the performance of Si position–sensitive detectors", Proc. 4th Int. Conference on Solid–State Sensors and Actuators, Tokyo, pp.423–426, 1987.

Y. Z. Xing and W. J. Lian, "A novel integrated optical potentiometer", Proc. 4th Int. Conference on Solid–State Sensors and Actuators, Tokyo, pp.427–430, 1987.

Y. Z. Xing, "A simple light–spot position detector with a light–intensity variation–insensitive output", Proc. EUROSENSORS I, Cambridge, pp.227–228, 1987.

Y. Z. Xing, "Substrate and defect influences on the position–response linearity of position–sensitive detectors", Proc. ESSDERC'88, Montpellier, pp.821–824, 1988.

Y. Z. Xing, F. Schneider, "A bubble–level tilt sensor with a large measurement range", Technical Digest EUROSENSORS II, Enschede, p.130, 1988.

About the Author

Yizi Xing was born in Peking, China, in 1958. He attended primary and secondary school from 1967 to 1978 in Peking, China. In 1978 he passed the country–wide entrance examination for universities in China and became a student in the Peking University, Peking.

He came to the Netherlands in February, 1979. After a six months Dutch course in the Language Laboratory of the Delft University of Technology, he began his study in the Faculty of Electrical Engineering of the same university in August, 1979. In november 1984, he received the M.S. degree cum laud on a thesis that dealt with an angular position–sensitive detector.

In march 1985, he became a junior scientist in the Laboratory of Electronic Instrumentation, Faculty of Electrical Engineering of the same university. Since then he has been involved in research on an electronic spirit level tilt sensor and has been working towards his Ph.D. degree.